

The ROCS and DIT COMPUTER CODES for NUCLEAR DESIGN

NUCLEAR POWER SYSTEMS
DECEMBER, 1981

 **POWER
SYSTEMS**
COMBUSTION ENGINEERING, INC.

8112170111 811211
PDR TOPRP EMVC-E
B PDR

LEGAL NOTICE

THIS REPORT WAS PREPARED AS AN ACCOUNT OF WORK SPONSORED BY COMBUSTION ENGINEERING, INC. NEITHER COMBUSTION ENGINEERING NOR ANY PERSON ACTING ON ITS BEHALF:

A. MAKES ANY WARRANTY OF REPRESENTATION, EXPRESS OR IMPLIED INCLUDING THE WARRANTIES OF FITNESS FOR A PARTICULAR PURPOSE OR MERCHANTABILITY, WITH RESPECT TO THE ACCURACY, COMPLETENESS, OR USEFULNESS OF THE INFORMATION CONTAINED IN THIS REPORT, OR THAT THE USE OF ANY INFORMATION, APPARATUS, METHOD, OR PROCESS DISCLOSED IN THIS REPORT MAY NOT INFRINGE PRIVATELY OWNED RIGHTS; OR

B. ASSUMES ANY LIABILITIES WITH RESPECT TO THE USE OF, OR FOR DAMAGES RESULTING FROM THE USE OF, ANY INFORMATION, APPARATUS, METHOD OR PROCESS DISCLOSED IN THIS REPORT.

TABLE OF CONTENTS

	Page
1.0 INTRODUCTION	1.1
2.0 THE ROCS CODE	2.1
2.1 Neutronics Models	2.4
2.1.1 Higher Order Difference Method	2.4
2.1.2 Nodal Expansion Method	2.15
2.1.3 Cross Section Representation	2.23
2.2 Depletion Model	2.26
2.3 Thermal Hydraulics	2.29
2.4 Feedback Models	2.31
2.5 Fuel Pin Peaking Model	2.32
2.6 References	2.38
3.0 THE DIT CODE	3.1
3.1 Structure of the Code	3.3
3.2 Transport Methods	3.5
3.3 Basic Cross Sections	3.8
3.4 Depletion Model	3.12
3.5 Verification Against Critical Experiments	3.16
3.6 References	3.25
4.0 DESIGN USE VERIFICATION	4.1
4.1 Normal Operation	4.2
4.1.1 Reactivity	4.3
4.1.2 Assembly Power Distributions	4.5
4.1.3 Inverse Boron Worth	4.11
4.1.4 Isothermal Temperature Coefficients	4.12
4.1.5 Control Rod Bank Worths	4.14
4.1.6 Power Coefficients	4.17
4.2 Upset Conditions	4.18
4.2.1 Dropped, Ejected & Net Rod Worths	4.19
4.2.2 Dropped & Ejected Rod Power Distributions	4.22
4.3 References	4.25
5.0 COMBINATION OF ASSEMBLY & LOCAL PEAKING UNCERTAINTIES	5.1
5.1 Statistical Model	5.1
5.2 Numerical Results	5.7
5.3 References	5.8
6.0 SUMMARY AND CONCLUSIONS	6.1

1.0 INTRODUCTION

This report describes the theory, design and performance of two computer codes used by Combustion Engineering, Inc. for the design of pressurized water nuclear reactor cores. The two codes are:

- ROCS, for two- and three-dimensional neutronics analysis;
- DIT, for the generation of coarse-mesh and fine-mesh, spectrum and space averaged, few-group cross sections.

The use of ROCS for coarse-mesh two- and three-dimensional neutronics analyses has previously been described in individual license applications (References 1.1 and 1.2, for example). This report provides a detailed description of the ROCS code, demonstrates the accuracy of the code through comparisons with experiments, and discusses current applications as well as anticipated future uses of the code. In addition to the coarse-mesh neutronics applications, ROCS can calculate local flux and power peaking using the MC module. This capability will eventually replace the current usage of fine-mesh PDQ in future license applications.

DIT has been used in license submittals since 1978 to ensure consistency in local power peaking between a transport theory calculation and the diffusion code PDQ. This use has been reported to the NRC in References 1.3 and 1.4. Coarse-mesh and fine-mesh few-group cross sections generated by DIT have been used in previous license submittals, Reference 1.5 for example.

Purpose of the Report

The purpose of this report is to document the methods, verification and level of accuracy for the computer codes ROCS (including an alternative numerical solution method, NEM) and DIT as well as for the computer code module MC for their use in new core and reload core design. This report will be referenced in future license submittals utilizing these computer codes.

Applicability of the Report

The computer codes and methods described in this report are intended for use in both new core and reload core design of nuclear reactor cores of the pressurized water (PWR) type. Their capabilities and levels of accuracy are concluded to be sufficient for the neutronics design including all safety related parameters dependent on two- and three-dimensional, coarse-mesh and fine-mesh flux and power distributions, control and absorber worths, the depletion and power dependent reactivity level, reactivity coefficients and reactivity differentials. It is also concluded that the ROCS code, including the fine-mesh module MC, is of sufficient accuracy for the generation of coefficient libraries for the incore instrumentation, replacing the use of two-dimensional PDQ in the procedures described in the topical report on the CECOR code system^(1.4).

This report quantifies the level of accuracy, in the form of statistical tolerance limits for example, for each particular application with the purpose of indicating that the accuracy of the code system is sufficient for the applications stated above. Numerical values of tolerance limits are in all cases smaller than the conservatism applied by C-E to the input for safety analyses. The levels of accuracy demonstrated in this report are such that they equal or exceed the levels of accuracy of previously employed design computer codes and methods.

Organization of the Report

Chapter 2 of this report describes the neutronics, depletion, thermal-hydraulic and feedback calculations performed by the ROCS code. Both the Higher Order Difference (HOD) method and the newer Nodal Expansion Method (NEM) are presented. Assembly power distributions obtained with both neutronics formulations are compared in Section 2.1. Calculative comparisons between PDQ and the local flux and power peaking MC module of ROCS are provided in Section 2.5.

Chapter 3 of this report describes the logic structure, transport theory methods, basic cross section library and depletion calculation used in the DIT code. It also describes the verification of DIT predictive capability by comparisons of reactivity and reaction rates with critical experiments. Reference 1.4 contains a detailed verification of the performance of DIT in fine-mesh applications for the purpose of predicting local power peaking. This verification is not repeated in this report. Verification of the application of DIT for the generation of cross sections for ROCS and MC is provided in Chapters 3 (critical experiments) and 4 (plant operation).

Chapter 4 contains the details of the ROCS/DIT verification. The performance for normal operating conditions is described in Section 4.1 by giving the results for extensive sets of comparisons with measurements. The performance of ROCS/DIT for upset core conditions is described, also by comparison to measured data, in Section 4.2.

Chapter 5 presents estimates of the uncertainties in the local fuel pin power peaking calculated with ROCS and MC using DIT cross sections. This is done by combining the assembly power results from Section 4.1.2 with the local power peaking results from Section 2.5.4.

Chapter 6 summarizes the numerical results of the analyses contained in this report.

1.1 REFERENCES

- 1.1. Letter, A. E. Lundvall, Jr. (BG&E) to R. W. Reid (NRC), BG&E Unit 1, Docket No. 50-137, February 23, 1979.
- 1.2. Letter, Robert E. Uhrig, (FPL&L) to Victor Stello (NRC), February 22, 1979, "St. Lucie Unit 1, Docket No. 50-335, Proposed Amendment to Facility Operating License DPR-67.
- 1.3. M. Raber, R. Lee, S. Visner, W. Corcoran, "Increased Waterhole Peaking in Operating Reactors, St. Lucie I", CEN-89(F)-P, March 30, 1978.
- 1.4. A. Jonsson, W. B. Terney, M. W. Crump, "Evaluation of Uncertainty in the Nuclear Power Peaking Measured by the Self-Powered, Fixed In-core Detector System", CENPD-153-P, Rev. 1-P-A, May 1980.
- 1.5 Letter, R. A. Clark (NRC) to W. Cavanaugh (AP&L), June 19, 1981, Safety Evaluation Report on Operation of ANO-2 During Cycle 2.

The Reactor Operation and Control Simulator code (ROCS) is a digital computer code for coarse-mesh, two- or three-dimensional neutronics analysis of nuclear reactor cores. The ROCS code was developed as a tool for realistic core analysis which effectively balances accuracy with computational speed. To achieve this objective, the code incorporates higher order expansion methods for the flux solution based on two-group diffusion theory. ROCS obtains a high degree of accuracy relative to traditional fine-mesh diffusion theory calculations, while requiring a low number of spatial mesh points. Additionally, the code employs thermal-hydraulic feedback models, calculates isotopic distributions, and has the capability to perform imbedded calculations for local flux and power distributions.

As originally developed, the ROCS code used a modified one-group diffusion theory model with the Higher Order Difference (HOD) method. References 2.1 - 2.4 describe the theory and application of the ROCS code with this modified one-group neutronics model. More recently, the neutronics model was extended to two energy groups.^(2.5) Only the two-group formulation is described in this report since calculations are no longer performed with the modified one-group diffusion theory model. In application, the two-group model has provided significant reductions in reactivity and box power sharing errors which are inherently present for coarse-mesh simulators based on one-group diffusion theory. These improvements have been quantified based on comparisons with measurements^(2.6,2.7) and with fine-mesh, two-group calculations for heterogeneous lattices using the C-E version of the PDQ-7 code.^(2.8)

A brief description of the ROCS model specification and code structure follows in this section. The remainder of the chapter provides descriptions of specific models used in the ROCS code. The neutronics models and cross section representation are described in detail in Section 2.1. An alternative neutronics formulation, the Nodal Expansion Method (NEM)^(2.9) is presented in addition to the standard HOD method. This is followed by descriptions of the

depletion, thermal-hydraulic and feedback models in Sections 2.2 through 2.4. The MC module for imbedded fine-mesh diffusion theory calculations of local flux and power distributions is described and results for assembly and quarter core calculations are shown in Section 2.5.

Model Specification

The ROCS code is designed to perform two- or three-dimensional coarse-mesh reactor core calculations with full-, half- or quarter-core symmetric geometries. The mesh consists of rectangular parallelepiped "nodes" arranged contiguously in the xy-plane, with one or more axial meshes (or planes) in the z-direction. In most applications, only the active core region is represented, with albedo-like boundary conditions assigned to exterior nodes. A typical ROCS core geometry uses [] nodes per assembly in the xy plane and [] axial planes depending upon core height and in-core instrument locations.

The nodal macroscopic group constants used in the neutronics calculation are constructed from detailed isotopic concentrations and microscopic cross sections processed by the code. The isotopes specified include fixed depletable isotopes and a lumped residual representing nondepletable isotopes. The depletable isotopes include fission chain isotopes, fission products and burnable absorbers. Control rods are represented by macroscopic cross sections specific to different rod banks.

Code Structure and Capabilities

The ROCS code is modular in design. The primary modules consist of a) the basic core simulator module, b) the thermal-hydraulic module, and c) the cross section and depletion module. The program control and dynamic storage allocation are contained in the basic simulator module, in addition to the majority of input/output processing, the neutronics calculation, and control of feedback and criticality search calculations. The thermal-hydraulic module

performs the general thermal-hydraulic calculation for feedbacks used in the neutronics calculation. The third module processes cross sections for use in the flux calculation, and performs isotopic depletion calculations.

The basic calculational flow structure for the ROCS simulator is shown in Figure 2-1. The outer loop of the flow diagram corresponds to execution of one or more maneuvers specified for the simulation. Each maneuver consists of a specific sequence of calculations which include the processing of cross sections, the neutronics calculation, and an optional depletion or short term xenon time-stepping calculation. The neutronics calculation allows various options of iterative calculations for thermal-hydraulic feedbacks and equilibrium xenon, and for criticality search calculations for power level, control rod bank insertion, soluble boron concentration or inlet moderator temperature.

2.1 Neutronics Models

The ROCS neutronics models employs a nodal solution method for the standard two-group diffusion equations:

$$-\nabla \cdot D_1 \nabla \phi_1 + (\Sigma_{a1} + \Sigma_{R1}) \phi_1 = \frac{1}{\lambda} (v \Sigma_{f1} \phi_1 + v \Sigma_{f2} \phi_2) \quad (2.1-1)$$

$$-\nabla \cdot D_2 \nabla \phi_2 + \Sigma_{a2} \phi_2 = \Sigma_{R1} \phi_1 \quad (2.1-2)$$

The original Higher Order Difference (HOD) method used in the ROCS code was based on a modified one-group diffusion equation and has been described in References 2.1 and 2.4. The HOD method has since been extended to a full two-group formulation as described in Section 2.1.1 below. A two-group Nodal Expansion Method (NEM) has also been developed for use in ROCS; NEM provides higher computational efficiency (with comparable accuracy) than the present HOD method. The NEM model is described below in Section 2.1.2, and typical results are shown. The coarse mesh cross section representation used in the ROCS neutronics models is described in Section 2.1.3.

2.1.1. Higher Order Difference (HOD) Method

Difference Approximation

The HOD formulation is derived using a Taylor series expansion representation of the flux in xyz directional coordinates. The coarse-mesh geometry consists of a lattice of rectangular nodes, each treated as having uniform properties. Figure 2-2 illustrates the geometry for a node ijk with center point (x_i, y_j, z_k) and boundaries at $x_i \pm h_i/2$, $y_j \pm h_j/2$ and $z_k \pm h_k/2$.

The flux for energy group g at any point (x,y,z) in node ijk is

expressed by the expansion

$$\begin{aligned} \phi_g^{ijk}(x,y,z) = & \phi_g^{ijk} + (x - x_i) f_{1g}^{ijk} (x - x_i) \\ & + (y_i - y_j) f_{2g}^{ijk} (y - y_j) \\ & + (z - z_k) f_{3g}^{ijk} (z - z_k) \end{aligned} \quad (2.1-3)$$

where ϕ_g^{ijk} is the flux at the center of the node and f^{ijk} is a polynomial function of degree n . Thus, f_{1g}^{ijk} has the following representation:

$$\begin{aligned} f_{1g}^{ijk}(x - x_i) &= \sum_{\ell=1}^n \frac{(x - x_i)^{\ell-1}}{\ell!} \frac{\partial^{\ell} \phi_g^{ijk}(x,y,z)}{\partial x^{\ell}} \Big|_{x_i y_j z_k} \\ &= \sum_{\ell=1}^n \frac{(x - x_i)^{\ell-1}}{\ell!} \phi_{\ell x g}^{ijk}(x,y,z) \Big|_{x_i y_j z_k} \end{aligned} \quad (2.1-4)$$

with f_{2g}^{ijk} and f_{3g}^{ijk} similarly defined and with $\phi_{\ell x g}^{ijk}(x_i, y_j, z_k)$ the " ℓ "th order partial derivative of the flux in node ijk at the center of the node.

For the following derivations, it is convenient to make use of the one-dimensional expansion for the flux,

$$\begin{aligned} \phi_g^i(x) &= \phi_g^i + (x - x_i) \cdot f_{1g}^i(x - x_i) \\ &= \phi_g^i + (x - x_i) \phi_{xg}^i + \frac{1}{2} (x - x_i)^2 \phi_{2xg}^i \\ &\quad + \frac{1}{6} (x - x_i)^3 \phi_{3xg}^i + \frac{1}{24} (x - x_i)^4 \phi_{4xg}^i + \dots \end{aligned} \quad (2.1-5)$$

and for the gradient,

$$\begin{aligned} \phi_{xg}^i(x) &= f_{1g}^i(x - x_i) + (x - x_i) \cdot f_{1g}^{i'}(x - x_i) \\ &= \phi_{xg}^i + (x - x_i) \phi_{2xg}^i + \frac{1}{2} (x - x_i)^2 \phi_{3xg}^i \\ &\quad + \frac{1}{6} (x - x_i)^3 \phi_{4xg}^i + \dots \end{aligned} \quad (2.1-6)$$

Two-group Nodal Equations

The two-group nodal equations for the HOD formulation can be derived through the standard procedure of integrating the two-group diffusion equations over the nodal volume, and using the flux and current continuity conditions at the interfaces to couple with adjacent nodes. The flux expansion approximation given above is used in the derivation and serves to give a higher order correction to the coarse mesh representation of the gradient and node-average flux.

The derivation starts by evaluating the integrals of the two-group diffusion equations, Eqs. (2.1-1) and (2.1-2), over the nodal volume V^{ijk} using the higher order expansion. The exact integrals are expressed by

$$\frac{1}{V^{ijk}} \int_{V^{ijk}} \nabla \cdot D_1 \nabla \phi_1 \, dV = \frac{1}{V^{ijk}} \int_{V^{ijk}} [(\Sigma_{a1} + \Sigma_{R1}) \phi_1 - \frac{1}{\lambda} (v \Sigma_{f1} \phi_1 + v \Sigma_{f2} \phi_2)] \, dV, \quad (2.1-7)$$

and

$$\frac{1}{V^{ijk}} \int_{V^{ijk}} \nabla \cdot D_2 \nabla \phi_2 \, dV = \frac{1}{V^{ijk}} \int_{V^{ijk}} [\Sigma_{a2} \phi_2 - \Sigma_{R1} \phi_1] \, dV \quad (2.1-8)$$

The left hand sides of Eqs. (2.1-7) and (2.1-8) can be evaluated using the divergence theorem and then substituting expansion forms given by Eqs.(2.1-3) through (2.1-6). Thus for each energy group g , by the divergence theorem,

$$\frac{1}{V^{ijk}} \int_{V^{ijk}} \nabla \cdot D_g \nabla \phi_g \, dV = \frac{1}{h_i h_j h_k} \int_{S^{ijk}} D_g^{ijk} \nabla \phi_g \cdot \hat{n} \, dS \quad (2.1-9)$$

which in expanded form becomes:

$$\begin{aligned}
&= (D_g^{ijk}/h_i) [\phi_{gx}^{ijk}(x_i+h_i/2) - \phi_{gx}^{ijk}(x_i-h_i/2)] \\
&+ (D_g^{ijk}/h_j) [\phi_{gy}^{ijk}(y_j+h_j/2) - \phi_{gy}^{ijk}(y_j-h_j/2)] \\
&+ (D_g^{ijk}/h_k) [\phi_{gz}^{ijk}(z_k+h_k/2) - \phi_{gz}^{ijk}(z_k-h_k/2)] \\
&= D_g^{ijk} [\phi_{2xg}^{ijk} + \phi_{2yg}^{ijk} + \phi_{2zg}^{ijk}] + (\phi_{4xg}^{ijk} h_i^2 + \phi_{4yg}^{ijk} h_j^2 \\
&+ \phi_{4zg}^{ijk} h_k^2)/24] + \dots
\end{aligned}$$

where S^{ijk} is the total nodal surface area and \hat{n} the outward normal. Eqs. (2.1-7) and (2.1-8) can then be approximated by

$$\begin{aligned}
D_1^{ijk} [(\phi_{2x1}^{ijk} + \phi_{2y1}^{ijk} + \phi_{2z1}^{ijk}) + (\phi_{4x1}^{ijk} h_i^2 + \phi_{4y1}^{ijk} h_j^2 + \phi_{4z1}^{ijk} h_k^2)/24] \quad (2.1-10) \\
= (\Sigma_{a1} + \Sigma_{R1} - v\Sigma_{f1}/\lambda) \Phi_1^{ijk} - (v\Sigma_{f2}/\lambda) \Phi_2^{ijk}
\end{aligned}$$

and

$$\begin{aligned}
D_2^{ijk} [(\phi_{2x2}^{ijk} + \phi_{2y2}^{ijk} + \phi_{2z2}^{ijk}) + (\phi_{4x2}^{ijk} h_i^2 + \phi_{4y2}^{ijk} h_j^2 + \phi_{4z2}^{ijk} h_k^2)/24] \quad (2.1-11) \\
= -\Sigma_{R1} \Phi_1^{ijk} + \Sigma_{a2} \Phi_2^{ijk},
\end{aligned}$$

respectively, where Φ_1^{ijk} and Φ_2^{ijk} represent the volume average nodal flux for groups 1 and 2. For each group g , this term can be approximated using the expansion in Eq. (2.1-3) as follows:

$$\begin{aligned}
\Phi_g^{ijk} &= \frac{1}{V^{ijk}} \int_{V^{ijk}} \phi_g(x,y,z) dV \quad (2.1-12) \\
&= \frac{1}{h_i h_j h_k} \int_{-h_i/2}^{h_i/2} \int_{-h_j/2}^{h_j/2} \int_{-h_k/2}^{h_k/2} [\phi_g^{ijk} \\
&+ \tilde{x} \cdot f_{1g}^{ijk}(\tilde{x}) + \tilde{y} \cdot f_{2g}^{ijk}(\tilde{y}) + \tilde{z} \cdot f_{3g}^{ijk}(\tilde{z})] d\tilde{x} d\tilde{y} d\tilde{z} \\
&\approx \phi_g^{ijk} + \frac{1}{3} [(h_i^2/8)\phi_{2xg}^{ijk} + (h_j^2/8)\phi_{2yg}^{ijk} + (h_k^2/8)\phi_{2zg}^{ijk}]
\end{aligned}$$

with the fourth and higher order partial derivative terms eliminated.

By using the flux and current continuity conditions at the node interfaces, the left hand sides of Eqs. (2.1-10) and (2.1-11) can be put in terms of fluxes in node ijk and its adjacent neighbors. For the interface between nodes ijk and $i+1,jk$ the respective conditions for energy group g are:

$$\phi_g^{ijk}(x_i+h_i/2,y,z) = \phi_g^{i+1jk}(x_{i+1}-h_{i+1}/2,y,z) \quad (2.1-13)$$

$$\begin{aligned} D_g^{ijk} \phi_{xg}^{ijk}(x_i+h_i/2,y,z) \\ = D_g^{i+1jk} \phi_{xg}^{i+1jk}(x_{i+1}-h_{i+1}/2,y,z) \end{aligned} \quad (2.1-14)$$

Using the expansions given by Eqs. (2.1-5) and (2.1-6) these respective conditions can be expressed for the point $(x_i+h_i/2, y_j, z_k)$ by:

$$\begin{aligned} \phi_g^{ijk} + (h_i/2) f_{1g}^{ijk}(h_i/2) \\ = \phi_g^{i+1jk} - (h_{i+1}/2) f_{1g}^{i+1jk}(-h_{i+1}/2) \end{aligned} \quad (2.1-15)$$

$$\begin{aligned} D_g^{ijk} [(h_i/2) f_{1g}^{ijk}(h_i/2) + f_{1g}^{ijk}(h_i/2)] \\ = D_g^{i+1jk} [(-h_{i+1}/2) f_{1g}^{i+1jk}(-h_{i+1}/2) \\ + f_{1g}^{i+1jk}(-h_{i+1}/2)] \end{aligned} \quad (2.1-16)$$

Thus, following the form of the one-group HOD derivation in Reference 2.4, one algebraically combines Eqs. (2.1-15) and (2.1-16) to obtain the following equation representing the internodal leakage for group

g between nodes ijk and $i+1, jk$:

$$\begin{aligned}
 W_{xg+}^{ijk} \phi_g^{ijk} + (D_g^{ijk}/h_i) f_{1g}^{ijk}(h_i/2) & \quad (2.1-17) \\
 + [D_g^{ijk}/2 - (h_i/2)^2 W_{xg+}^{ijk}] f_{1g}'^{ijk}(h_i/2) \\
 = W_{xg+}^{ijk} [\phi_g^{i+1jk} - (h_{i+1}/2)^2 f_{1g}'^{i+1jk}(-h_{i+1}/2)]
 \end{aligned}$$

where

$$W_{xg+}^{ijk} = \left(\frac{2}{h_i}\right) \left(-\frac{h_i}{D_g^{ijk}} + \frac{h_{i+1}}{D_g^{i+1jk}}\right)^{-1}$$

A similar equation connecting nodes $i-1, jk$ and ijk has the following form:

$$\begin{aligned}
 W_{xg-}^{ijk} \phi_g^{ijk} - (D_g^{ijk}/h_i) f_{1g}^{ijk}(-h_i/2) & \quad (2.1-18) \\
 + [D_g^{ijk}/2 - (h_i/2)^2 W_{xg-}^{ijk}] f_{1g}'^{ijk}(-h_i/2) \\
 = W_{xg-}^{ijk} [\phi_g^{i-1jk} - (h_{i-1}/2)^2 f_{1g}'^{i-1jk}(h_{i-1}/2)]
 \end{aligned}$$

with W_{xg-}^{ijk} similarly defined. By adding Eqs. (2.1-17) and (2.1-18) and substituting the fourth order expansions for f_{1g}^{ijk} and $f_{1g}'^{ijk}$ the following x-direction coupling equation results, representing the net leakage for node ijk , group g in the x-direction:

$$\begin{aligned}
 W_{xg+}^{ijk} & \{ [\phi_g^{i+1jk} - (h_{i+1}^2/8) \phi_{2xg}^{i+1jk} + (h_{i+1}^3/24) \phi_{3xg}^{i+1jk} - (h_{i+1}^4/128) \phi_{4xg}^{i+1jk}] \\
 & - [\phi_g^{ijk} - (h_i^2/8) \phi_{2xg}^{ijk} - (h_i^3/24) \phi_{3xg}^{ijk} - (h_i^4/128) \phi_{4xg}^{ijk}] \} \\
 + W_{xg-}^{ijk} & \{ [\phi_g^{i-1jk} - (h_{i-1}^2/8) \phi_{2xg}^{i-1jk} - (h_{i-1}^3/24) \phi_{3xg}^{i-1jk} - (h_{i-1}^4/128) \phi_{4xg}^{i-1jk}] \\
 & - [\phi_g^{ijk} - (h_i^2/8) \phi_{2xg}^{ijk} + (h_i^3/24) \phi_{3xg}^{ijk} - (h_i^4/128) \phi_{4xg}^{ijk}] \} \\
 = D_g^{ijk} & [\phi_{2xg}^{ijk} + (h_i^2/24) \phi_{4xg}^{ijk}] \quad (2.1-19)
 \end{aligned}$$

Similar equations can be obtained to represent the leakages in the y- and z-directions. Combining all three of these equations gives the total leakage for node ijk:

$$D_g^{ijk} [(\phi_{2xg}^{ijk} + \phi_{2yg}^{ijk} + \phi_{2zg}^{ijk}) + (\phi_{4xg}^{ijk} h_i^2 + \phi_{4yg}^{ijk} h_j^2 + \phi_{4zg}^{ijk} h_k^2)/24] = X_g + Y_g + Z_g \quad (2.1-20)$$

where X_g is the left side of Eq.(2.1-19), with Y_g and Z_g the left sides of similar equations.

The two-group nodal equations in the HOD formulation are obtained by substituting Eq.(2.1-20) into the left sides of Eqs. (2.1-10) and (2.1-11) from the first part of the derivation and then eliminating the remaining third and fourth order derivative terms.* The resulting equations for group 1 and 2, respectively, are:

$$\begin{aligned} W_{x1+}^{ijk} [\phi_1^{i+1jk} (1 - \beta_{x1}^{i+1jk}) - \phi_1^{ijk} (1 - \beta_{x1}^{ijk})] \\ + W_{x1-}^{ijk} [\phi_1^{i-1jk} (1 - \beta_{x1}^{i-1jk}) - \phi_1^{ijk} (1 - \beta_{x1}^{ijk})] + \tilde{Y}_1 + \tilde{Z}_1 \\ = (\Sigma_{a1} + \Sigma_{R1} - \nu \Sigma_{f1}/\lambda) \psi_1^{ijk} \phi_1^{ijk} \\ - (\nu \Sigma_{f2}/\lambda) \psi_2^{ijk} \phi_2^{ijk} \end{aligned} \quad (2.1-21)$$

$$\begin{aligned} W_{x2+}^{ijk} [\phi_2^{i+1jk} (1 - \beta_{x2}^{i+1jk}) - \phi_2^{ijk} (1 - \beta_{x2}^{ijk})] \\ + W_{x2-}^{ijk} [\phi_2^{i-1jk} (1 - \beta_{x2}^{i-1jk}) - \phi_2^{ijk} (1 - \beta_{x2}^{ijk})] + \tilde{Y}_2 + \tilde{Z}_2 \\ = -\Sigma_{R1} \psi_1^{ijk} \phi_1^{ijk} + \Sigma_{a2} \psi_2^{ijk} \phi_2^{ijk} \end{aligned} \quad (2.1-22)$$

* These derivative terms have been found to be negligible for most PWR calculations (Reference 2.1)

where

$$\beta_{xg}^{ijk} = (h_i^2/8) (\phi_{2xg}^{ijk}/\phi_g^{ijk})$$

and β_{yg}^{ijk} , β_{zg}^{ijk} are similarly defined. The node-average to centerpoint flux ratio is

$$\bar{\phi}_g^{ijk} = \phi_g^{ijk} / \phi_g^{ijk} = 1 + (\beta_{xg}^{ijk} + \beta_{yg}^{ijk} + \beta_{zg}^{ijk})/3$$

The \tilde{Y}_g and \tilde{Z}_g represent the truncated y- and z-direction terms as in Eq. (2.1-20).

Boundary Conditions

The two-group boundary conditions used in the HOD formulation physically represent the ratio of outer face current to the node-average flux of the nodes at the core-reflector interface for each energy group. [



The form of the HOD boundary condition is illustrated for a node ijk with the x_+ face bounding the active core. The two-group boundary conditions are defined by

$$a_{xg+}^{ijk} = \frac{J_{xg+}^{ijk}}{\phi_g^{ijk}}, \quad g = 1, 2 \quad (2.1-23)$$

where J_{xg+}^{ijk} is the net current for group g at the $x+$ nodal face, represented by

$$J_{xg+}^{ijk} = -D_g^{ijk} \phi_{gx}^{ijk} (x_i + h_i/2) \quad (2.1-24)$$

The $x+$ boundary condition form in Eq. (2.1-23) corresponds to the gradient term at $x_i + h_i/2$ in Eq. (2.1-9). Thus the boundary condition can be substituted into the left hand side of Eq. (2.1-21) or (2.1-22) using

$$\begin{aligned} -\alpha_{xg+}^{ijk} \phi_g^{ijk}/h_i &= (D_g^{ijk}/h_i) \phi_{gx}^{ijk} (x_i + h_i/2) \\ &= W_{xg+}^{ijk} [\phi_g^{i+1jk} (1 - \beta_{xg}^{i+1jk}) - \phi_g^{ijk} (1 - \beta_{xg}^{ijk})] \end{aligned} \quad (2.1-25)$$

Similar boundary condition forms apply for the other node faces.

Two-group Matrix Solution

The two-group HOD equations for the core model are obtained by combining Eqs. (2.1-21) and (2.1-22) with boundary conditions as represented by Eq. (2.1-25). The resulting system can be represented by two-group matrix equations of the form

$$A_{11} \bar{\phi}_1 + A_{12} \bar{\phi}_2 = 0 \quad (2.1-26)$$

$$A_{21} \bar{\phi}_1 + A_{22} \bar{\phi}_2 = 0 \quad (2.1-27)$$

The solution vectors $\bar{\phi}_1$ and $\bar{\phi}_2$ contain the elements ϕ_1^{ijk} and ϕ_2^{ijk} , respectively.

The matrices A_{11} and A_{22} correspond to group 1 and 2 operators

for the seven-point finite difference equations:

$$a_{xg-}^{ijk} \phi_g^{i-1jk} + \dots + a_g^{ijk} \phi_g^{ijk} + \dots + a_{zg+}^{ijk} \phi_g^{ijk+1} = 0 \quad (2.1-28)$$

with coefficients

$$a_{xg-}^{ijk} = W_{xg-}^{ijk} (1 - \beta_{xg}^{i+1jk}) \delta_{x-}^{ijk}, \quad g = 1, 2$$

$$a_1^{ijk} = - [\Sigma_{a1}^{ijk} + \Sigma_{R1}^{ijk} - v \Sigma_{f1}^{ijk}(\lambda) \psi_1^{ijk} + b_{x1-}^{ijk} + \dots + b_{z1+}^{ijk}]$$

$$a_2^{ijk} = - [\Sigma_{a2}^{ijk} \psi_2^{ijk} + b_{x2-}^{ijk} + \dots + b_{z2+}^{ijk}]$$

and $\delta_{x+}^{ijk} = 0$, if the $i+1$ node does not exist (i.e., the ijk node is adjacent to the reflector)

$$\delta_{x+}^{ijk} = 1, \text{ if the } i+1 \text{ node exists,}$$

$$b_{xg+}^{ijk} = W_{xg+}^{ijk} (1 - \beta_{xg}^{ijk}) \delta_{x+}^{ijk} + \alpha_{xg+}^{ijk} \psi_g^{ijk} (1 - \delta_{x+}^{ijk}) / h_i$$

α_{xg+}^{ijk} = boundary condition for group g at $x+$ face of node ijk .

Additionally,

$$\beta_{xg}^{ijk} = (\xi h_i^2 / 8) \phi_{2xg}^{ijk} / \phi_g^{ijk}$$

$$\psi_g^{ijk} = 1 + (\beta_{xg}^{ijk} + \beta_{yg}^{ijk} + \beta_{zg}^{ijk})$$

where ξ is an underrelaxation factor used in the iterative calculation.

The matrix A_{12} contains diagonal elements $(v \Sigma_{f2}^{ijk} / \lambda) \phi_2^{ijk}$ representing the thermal to fast group source in Eq. (2.1-26). Similarly A_{21} is a diagonal matrix with elements $\Sigma_{R1}^{ijk} \phi_1^{ijk}$ representing the fast-to-thermal source in Eq. (2.1-17).

Eqs. (2.1-26) and (2.1-27) contain additional unknowns in the second derivative terms β_{xg} , β_{yg} and β_{zg} , and the eigenvalue λ . These

values are obtained using auxiliary equations in the iterative solution. The second derivative term β_{xg} , for example, is obtained by solving the x-direction leakage equation given by Eq. (2.1-19) for ϕ_{2xg} with higher derivative terms eliminated. The resulting equation with boundary condition terms included is

$$\begin{aligned}
 D_g^{1jk} \phi_{2xg}^{1jk} &= & (2.1-29) \\
 W_{xg+}^{1jk} \{ [\phi_g^{1+1jk} - (h_{i+1}^2/8) \phi_{2xg}^{1+1jk}] - [\phi_g^{1jk} - (h_i^2/8) \phi_{2xg}^{1jk}] \} \delta_{x+}^{1jk} \\
 + W_{xg-}^{1jk} \{ [\phi_g^{1-1jk} - (h_{i-1}^2/8) \phi_{2xg}^{1-1jk}] - [\phi_g^{1jk} - (h_i^2/8) \phi_{2xg}^{1jk}] \} \delta_{x-}^{1jk} \\
 - a_{xg+}^{1jk} \phi_g^{1jk} (1 - \delta_{x+}^{1jk})/h_i & \quad - a_{xg-}^{1jk} \phi_g^{1jk} (1 - \delta_{x-}^{1jk})/h_i
 \end{aligned}$$

The flux and derivative values from the previous iteration are used for the right hand side of Eq. (2.1-29). Similar equations are used to solve for β_{yg} and β_{zg} .

The eigenvalue is calculated using the conventional two-group formulation

$$\lambda = \lambda_1 + \lambda_2 \quad (2.1-30)$$

where

$$\begin{aligned}
 \lambda_1 &= \frac{\sum_{ijk} v \Sigma_{f1}^{ijk} \psi_1^{ijk} \phi_1^{ijk} v^{ijk}}{\sum_{ijk} (\Sigma_{a1}^{ijk} + \Sigma_{R1}^{ijk} + L_1^{ijk}) \psi_1^{ijk} \phi_1^{ijk} v^{ijk}} \\
 \lambda_2 &= P_{1-2} \frac{\sum_{ijk} v \Sigma_{f2}^{ijk} \psi_2^{ijk} \phi_2^{ijk} v^{ijk}}{\sum_{ijk} (\Sigma_{a2}^{ijk} + L_2^{ijk}) \psi_2^{ijk} \phi_2^{ijk} v^{ijk}}
 \end{aligned}$$

and the resonance escape probability is given by

$$P_{1-2} = \frac{\sum_{ijk} \Sigma_{R1}^{ijk} \psi_1^{ijk} \phi_1^{ijk} v^{ijk}}{\sum_{ijk} (\Sigma_{a1}^{ijk} + \Sigma_{R1}^{ijk} + L_1^{ijk}) \psi_1^{ijk} \phi_1^{ijk} v^{ijk}}$$

The boundary leakage terms L_1^{ijk} and L_2^{ijk} are given by

$$L_g^{ijk} = \alpha_{xg-}^{ijk} (1 - \delta_{x-}^{ijk})/h_x + \dots + \alpha_{zg+}^{ijk} (1 - \delta_{z+}^{ijk})/h_z \quad (2.1-31)$$

$$g = 1,2$$

The overall solution of the two-group HOD equations is obtained by the iterative procedure indicated in Figure 2-3. The matrix equations given by Eqs. (2.1-26) and (2.1-27) are solved by the successive overrelaxation (SOR) method. The iteration cycle consists of a group 1 flux iteration followed by a group 2 iteration, with second derivative terms updated during each pass. Independent SOR acceleration parameters are used for the two energy group calculations. At the end of each iteration cycle the eigenvalue is calculated; also, the underrelaxation factor for derivative terms is increased according to the degree of convergence, so that $\xi=1$ for the converged solution.

2.1.2 Nodal Expansion Method (NEM)

The Nodal Expansion Method (NEM)^(2.9,2.11,2.12) will be available in ROCS as an alternative to the current HOD method. At present, NEM has been incorporated in a special version of the C-E coarse-mesh kinetics code, HERMITE,^(2.13). NEM uses one-dimensional fourth order polynomial expansions for each direction within the node to establish highly accurate internodal currents.

The derivation of the method begins with the following form of the two-group diffusion equation.

$$\begin{aligned} \nabla \cdot \bar{J}_g(\bar{r}) + \Sigma_{ag}(\bar{r})\phi_g(\bar{r}) + \Sigma_{g'} \Sigma_{g'g}(\bar{r}) \phi_{g'}(\bar{r}) \\ = \Sigma_{g'} [\Sigma_{g'g}(\bar{r}) + \frac{1}{\lambda} \chi_{g'} \nu \Sigma_{fg'}(\bar{r})] \phi_{g'}(\bar{r}) \end{aligned} \quad (2.1-32)$$

Neutron currents and fluxes are related by Fick's Law

$$J_g(\vec{r}) + D_g(\vec{r}) \nabla \phi_g(\vec{r}) = 0 \quad (2.1-33)$$

and the following equations for net current and flux

$$j_{gu} = j_{gu}^+ - j_{gu}^- \quad (2.1-34)$$

$$\phi_g = 2(j_{gu}^+ + j_{gu}^-) \quad (2.1-35)$$

Here j_{gu} and ϕ_g are the net current and flux respectively and the subscript u represents either the x, y or z direction. The $+$ or $-$ superscript on the currents indicates a partial current in the $+$ or $-$ u direction.

A mesh of M rectangular nodes is defined to create a discrete problem geometry. A given node, M , is assumed to have sides a_x^m , a_y^m , a_z^m and volume

$$V^m = a_x^m a_y^m a_z^m$$

The origin is positioned at a corner of the node so that

$$0 \leq u \leq a_u^m$$

The node has three "left" surfaces and three "right" surfaces. An arbitrary surface is designated u_s where $u = x, y$ or z and $s = l$ or r . Thus

$$u_l = 0 \text{ and } u_r = a_u^m$$

The neutron balance for the node can be obtained by integrating Eq.

(2.1-32) over the node and applying the divergence theorem and Eq. (2.1-34). This results in the nodal balance equation:

$$\sum_u \frac{1}{a_u^m} [(j_{gu\ell}^{-m} + j_{gur}^{+m}) - (j_{gu\ell}^{+m} + j_{gur}^{-m})] + (\Sigma_{ag}^m + \sum_{g'} \Sigma_{g'g'}) \phi_g^m = \sum_{g'} (\Sigma_{g'g}^m + \frac{1}{\lambda} \chi_g \nu \Sigma_{fg'}) \phi_{g'}^m \quad (2.1-36)$$

where ϕ_g^m represents the node-average flux and Σ_{ag}^m and Σ_{fg}^m are flux and volume weighted cross sections for node m.

The interface conditions at abutting surfaces of adjacent nodes are statements of the continuity of the average partial currents:

$$j_{gur}^{+m} = j_{gu\ell}^{+m'} \quad \text{and} \quad j_{gur}^{-m} = j_{gu\ell}^{-m'} \quad (2.1-37)$$

These conditions are equivalent to the continuity of the face-average flux, ψ_{gus}^m , and the net current as may be seen by applying Eqs. (2.1-34) and (2.1-35).

Thus

$$j_{gur}^m = j_{gu\ell}^{m'} \quad (2.1-38)$$

and

$$\psi_{gu\ell}^m = \psi_{gur}^{m'} \quad (2.1-39)$$

where the average flux on face u_s is given by

$$\psi_{gus}^m = \int_0^{a_v^m} \int_0^{a_w^m} dv dw \phi_g(\bar{r})$$

evaluated at $s = \ell$ or $s = r$.

with v and w denoting the two directions perpendicular to u.

External boundary conditions are zero net current along axes of symmetry

$$j_{gus}^{+m} = j_{gus}^{-m} \quad (2.1-40)$$

and albedo boundary conditions elsewhere:

$$j_{gus}^{+} = \alpha_{gus}^{-m} j_{gus}^{-m} \quad (2.1-41)$$

In order to obtain the node-average fluxes ϕ_g^m , the interface and boundary conditions are used to eliminate the incoming currents. Traditional nodal methods define coupling coefficients to provide the missing equations. The Nodal Expansion Method differs from the traditional nodal methods in the way the outgoing currents are eliminated from the nodal balance equations. The flux distribution within the node is taken into account and, in effect, the coupling coefficients are determined as the solution progresses.

For the nodal balance the face-average flux and net current are obtained by integrating the flux over the two directions (v and w) transverse to u and, in the case of the net current, differentiating with respect to u. Therefore, an average flux is defined as a function of u to take into account the interior (nodal) flux distribution:

$$\psi_{gu}^m(u) = \frac{1}{a_v^m a_w^m} \int_0^{a_v^m} \int_0^{a_w^m} \phi_g(r) dv dw \quad (2.1-42)$$

clearly

$$\psi_{gu\ell}^m = \psi_{gu}^m(0) \text{ and } \psi_{gur}^m = \psi_{gu}^m(a_u^m)$$

$$\phi_g^m = \int_0^{a_u^m} \psi_{gu}^m(u) du \quad (2.1-43)$$

and

$$j_{gus}^m = -D_g^m \frac{\partial \psi_{gu}^m}{\partial u} \quad (2.1-44)$$

evaluated at $u=0$ at $S=\lambda$ and $u=a_u^m$ for $S=r$.

$\psi_{gu}^m(u)$ is determined from an approximate one-dimensional diffusion equation along direction u obtained by integration of Eq. (2.1-32) over the transverse directions:

$$\begin{aligned} \frac{\partial}{\partial u} D_g^m \frac{\partial}{\partial u} \psi_{gu}^m + (\Sigma_{agu}^m + \Sigma_{g'} \Sigma_{g'g'u}) \psi_{gu}^m \\ = \Sigma_{g'} (\Sigma_{g'gu} + \frac{1}{\lambda} x_g v \Sigma_{fg'u}^m) \psi_{g'u}^m - D_g^m L_{gu}^m \end{aligned} \quad (2.1-45)$$

where $D_g^m L_{gu}^m$ is the transverse leakage given by

$$D_g^m L_{gu}^m = -\frac{1}{a_v^m a_w^m} \int_0^{a_v^m} \int_0^{a_w^m} dv dw \left(\frac{\partial}{\partial v} D_g \frac{\partial}{\partial v} + \frac{\partial}{\partial w} D_g \frac{\partial}{\partial w} \right) \phi_g(r) \quad (2.1-46)$$

The one-dimensional flux $\psi_{gu}^m(u)$ is approximated by a fourth order polynomial:

$$\begin{aligned} \psi_{gu}^m(u) = a_{0gu}^m h_0(u) + a_{1gu}^m h_1(u) + a_{2gu}^m h_2(u) \\ + a_{3gu}^m h_3(u) + a_{4gu}^m h_4(u) \end{aligned} \quad (2.1-47)$$

The basis functions $h_i(u)$ are polynomials of order i and are given below using $\mu = u/a_u^m$.

$$h_0 = 1 \quad (2.1-48a)$$

$$h_1 = 2\mu - 1 \quad (2.1-48b)$$

$$h_2 = 6\mu(1-\mu) - 1 \quad (2.1-48c)$$

$$h_3 = 6\mu(1-\mu)(2\mu-1) \quad (2.1-48d)$$

$$h_4 = 6\mu(1-\mu)(5\mu^2 - 5\mu + 1) \quad (2.1-48e)$$

If the face-average fluxes and currents and the node-average flux are known, the coefficients a_{igu}^m can be computed using Eqs. (2.1-48) and (2.1-43) through (2.1-45). The transverse leakage term, $-D_g^m L_{gu}^m$, is approximated by the quadratic polynomial

$$\begin{aligned} L_{gu}^m = & \overline{L_{gu}^m} + \frac{1}{2} (L_{1gu}^m - L_{0gu}^m) h_1 \\ & + [\overline{L_{gu}^m} - \frac{1}{2} (L_{1gu}^m - L_{0gu}^m)] h_2 \end{aligned} \quad (2.1-49)$$

where

$$-D_g^m \overline{L_{gu}^m} = j_{gv\ell}^m - j_{gvr}^m + j_{gw\ell}^m - j_{gwr}^m \quad (2.1-50)$$

The coefficients of h_1 and h_2 in Eq. (2.1-49) were chosen so the L_{0gu}^m and L_{1gu}^m are the values of L_{gu}^m assumed at the left and right u-ends of the node respectively.

The boundary and interface equations together with the nodal balance equation provide enough equations to account for three coefficients of the quartic polynomial for ψ_{gu}^m . Two more equations are obtained by the weighted residual technique.

Define the weighting functions $w_1 = h_1$ and $w_2 = h_2$ and

integrate w_1 times both sides of Eq. (2.1-45) over $0 \leq u \leq a_u^m$. Thus one obtains the " w_1 weighted balance equation" after considerable algebraic manipulation:

$$\begin{aligned}
 & (\Sigma_{agu}^m + \Sigma_{g'}^m \Sigma_{g'u}^m) \left(\frac{1}{3} a_{1gu}^m + \frac{1}{5} a_{3gu}^m \right) + 12 D_{gu}^m a_{3gu}^m \\
 & + \frac{1}{6} D_g^m (L_{1gu}^m - L_{0gu}^m) - \Sigma_{g'}^m \left(\Sigma_{g'gu}^m + \frac{1}{\lambda} \chi_g \nu \Sigma_{fg'u}^m \right) \left(\frac{1}{3} a_{1g'u}^m + \frac{1}{5} a_{3g'u}^m \right) \\
 & = 0
 \end{aligned} \tag{2.1-51}$$

The " w_2 weighted balance equation" is similarly derived:

$$\begin{aligned}
 & (\Sigma_{agu}^m + \Sigma_{g'}^m \Sigma_{g'u}^m) \left(\frac{1}{5} a_{2gu}^m - \frac{3}{35} a_{4gu}^m \right) - 12 D_{gu}^m a_{4gu}^m \\
 & + \frac{1}{5} D_g^m \left[L_g^m - \frac{1}{2} (L_{1gu}^m + L_{0gu}^m) \right] - \Sigma_{g'}^m \left(\Sigma_{g'gu}^m + \frac{1}{\lambda} \chi_g \nu \Sigma_{fg'u}^m \right) \\
 & \left(\frac{1}{3} a_{2g'u}^m - \frac{3}{35} a_{4g'u}^m \right) = 0
 \end{aligned} \tag{2.1-52}$$

There are now two equations per energy group (2.1-51 and 2.1-52) for each spatial direction plus a single overall nodal balance equation (2.1-36). In addition, there are the conditions of continuity of face-average flux and current at each internal interface and an albedo at each boundary. These provide a sufficient set of independent equations to solve for the partial currents on each nodal face and for each node-average flux. These equations are solved iteratively for the fluxes, currents and the eigenvalue.

Results With The Nodal Expansion Method

The NEM and HOD methods for solving the neutron diffusion equation have been compared to each other and to fine-mesh calculations using consistent two-dimensional quarter core models of the Arkansas Nuclear One Unit 2 (ANO-2) Cycle 1 midplane. NEM and HOD calculations were also performed in three dimensions early in the same reactor cycle.

The fine-mesh calculations were performed in two dimensions with PDQ (2.8), the HOD calculations with ROCS and the NEM calculations within the host code HERMITE. (2.13) [

] External radial boundary conditions for the NEM and HOD models were obtained in parallel from the same source. The same DIT runs were used to produce consistent cross section tables for the fine-mesh PDQ model and the coarse-mesh ROCS/HOD and HERMITE/NEM models. The standard xenon equilibrium equations and equivalent fuel temperature correlations were used in all three reactor models. [

]

Midplane assembly relative power densities calculated by the NEM and HOD methods in two dimensions are compared to fine-mesh PDQ power distributions in Figures 2-4 through 2-6 for BOC, MOC and EOC respectively. Both coarse-mesh calculations closely approximate the fine-mesh PDQ. The standard deviations are [] or less and maximum differences from PDQ assembly powers are less than []

Three-dimensional comparisons of NEM with HOD were performed for AND-2 early in the first cycle with HERMITE and ROCS models that were equivalent to those used for the above two-dimensional comparisons. The HERMITE host code used axial albedos for NEM that were consistent with the axial boundary conditions in the ROCS calculations.

Figure 2-7 shows NEM and HOD radially averaged axial power distributions from unrodded full power equilibrium xenon calculations at beginning-of-life. Both solution methods produce essentially the same axial shape. Figure 2-8 shows a comparison of the corresponding midplane assembly relative power densities. The standard deviation of assembly power differences is about [] and the maximum difference about []. Consistently close agreement between the two methods is obtained at other radial planes. Figure 2-9 shows the standard deviations and maximum errors resulting from these radial comparisons between NEM and HOD as a function of axial position.

The standard deviations of the differences between the HOD and NEM methods are of the order of [] while those for the HOD method vs. measurement are in the range of [] (Section 4.1.2). This indicates that cross section models are more important than neutronics models in determining the overall uncertainty. With this level of agreement, substitution of NEM for the HOD method in ROCS is not expected to have any major impact on calculational uncertainties.

2.1.3 Cross Section Representation

Cross section information used in the ROCS system is derived from microscopic cross sections supplied by DIT for each nuclide in two energy groups. This information is utilized in two basic forms. First, two-group macroscopic cross sections are used in the basic flux and eigenvalue calculation as described in Section 2.1.1. The macroscopic contributions due to thermal-hydraulic feedbacks, xenon, soluble boron and control rods are added prior to the flux calculation. Second, two-group microscopic cross sections are used explicitly in the depletion and xenon short-term time-stepping calculations as described in Section 2.2.

The two-group microscopic cross sections for each nuclide are supplied in table form. Represented for each nuclide and energy group are:

- σ_{tr} = transport cross section (b)
- σ_a = absorption cross section (b)
- σ_R = removal cross section (b)
- σ_f = fission cross section (b)
- ν = average number of neutrons released per fission
- κ = average energy release per fission (watt-sec)

The tables represent the above values as nonlinear functions of important independent variables [] evaluated for nominal thermal-hydraulic conditions. In addition, multipliers (called G-factors) may be included in the table for any of the cross sections. The G-factors may also be represented as functions of pertinent independent variables. Thus a typical cross-section table interpolation can be

represented symbolically by:

$$[\quad \quad \quad] \quad (2.1-53)$$

where

ρ_0, T_{M0}, T_{F0} = nominal moderator density, moderator temperature and fuel temperature;

N_1, \dots, N_6 = independent variables for table interpolation.

The cross sections are assumed to vary with moderator temperature, moderator density, and the square root of the fuel temperature for small changes about the nominal. The dependence of the cross sections on the thermal-hydraulic parameters is usually approximated by the inclusion of the first derivative of the cross section, for example:

$$\begin{aligned} \sigma(\rho, T_M, T_F) &= \sigma(\rho_0, T_{M0}, T_{F0}) \\ &+ \frac{\partial \sigma}{\partial \rho} \Delta \rho + \frac{\partial \sigma}{\partial T_M} \Delta T_M + \frac{\partial \sigma}{\partial (T_F)^{1/2}} \Delta (T_F)^{1/2} \end{aligned} \quad (2.1-54)$$

where

$$\begin{aligned} \Delta \rho &= \rho - \rho_0 && = \text{change in density from nominal value} \\ \Delta T_M &= T_M - T_{M0} && = \text{change in moderator temperature from nominal} \\ \Delta (T_F)^{1/2} &= (T_F)^{1/2} - (T_{F0})^{1/2} && = \text{change in square root of fuel temperature from nominal} \end{aligned}$$

The cross section derivative terms in Eq. (2.1-54)* are also

[

The $(\Delta \rho, \Delta T_M, \Delta T_F)$ terms are derived from a heat balance calculation for each node and are updated each feedback pass (see Fig. 2-1).

* and in Eq. (2.1-55)

The microscopic cross sections used in the depletion segment are obtained using Eq. (2.1-54). Similarly, the macroscopic group constants used in the flux calculation are obtained by combining the number densities, microscopic cross section data and feedback terms, e.g.,

$$\begin{aligned} \Sigma(\rho, T_M, T_F) &= \Sigma_0(\rho_0, T_{M0}, T_{F0}) \\ &+ \frac{\partial \Sigma}{\partial \rho} \Delta \rho + \frac{\partial \Sigma}{\partial T_M} \Delta T_M + \frac{\partial \Sigma}{\partial (T_F)^{1/2}} \Delta (T_F)^{1/2} \end{aligned} \quad (2.1-55)$$

where, for example

$$\Sigma_0(\rho_0, T_{M0}, T_{F0}) = \sum_i N_i \sigma^i(\rho_0, T_{M0}, T_{F0}),$$

$$\frac{\partial \Sigma}{\partial \rho} = \sum_i N_i \left(\frac{\partial \sigma}{\partial \rho} \right)_i,$$

$$\frac{\partial \Sigma}{\partial T_M} = \sum_i N_i \left(\frac{\partial \sigma}{\partial T_M} \right)_i,$$

$$\frac{\partial \Sigma}{\partial (T_F)^{1/2}} = \sum_i N_i \left(\frac{\partial \sigma}{\partial (T_F)^{1/2}} \right)_i$$

Here, N_i is the number density of the i^{th} nuclide (assumed constant in the above derivative terms) while σ^i , $\left(\frac{\partial \sigma}{\partial \rho} \right)_i$, etc., are the corresponding microscopic terms for nominal conditions. The nuclides used in forming the macroscopic cross sections include the depletable isotopes plus a lumped residual, which contains all the nondepletable isotopes.

2.2 Depletion Model

The ROCS system performs coarse mesh depletion calculations for each node in a two- or three-dimensional core configuration. The allowed depletion chains are internally modeled with fixed depletion equations so that beyond the input cross section data the user need supply only such data as initial concentrations, decay constants and fission yields for each depletion nuclide. Table 2.1 shows the principal depletion nuclides which can be specified and their chain structures. These include the principal uranium and plutonium isotopes, a fuel exposure chain, xenon and samarium fission product chains, and boron and gadolinium burnable absorber chains.

The fixed depletion equations used in the ROCS code are derived through the standard procedure of analytically integrating the coupled linear rate equations which represent each chain. The production and depletion reactions for each depletion nuclide are indicated in Table 2.1. The depletion equations are solved using the flux and microscopic cross section values based on the neutronics and thermal-hydraulic feedback calculations preceding the depletion time step. The initial flux and cross sections are assumed constant over the depletion time step.

2.2.1 Fuel Depletion

The fissionable isotope chains used in the depletion model are representative of fuel used in commercial and conceptual LWR designs. The ^{238}U depletion model shown in Table 2.1 includes a [] This model enables detailed tracing of the plutonium isotopic concentrations, thereby providing accurate prediction of plutonium contributions to the three-dimensional power and fuel exposure distributions through first and later cycle core depletion calculations.

The fuel exposure counter (MWD/T) in Table 2.1 is used to store nodal exposure values based on time integration of fission rates for the

^{235}U and ^{238}U chains. The exposure over a time step, Δt , is calculated according to the formula

$$\begin{aligned} \Delta(\text{MWD}/T) &= C \sum_j \int_{\Delta t} N_j(t) \kappa \sigma_g^j \phi dt \\ &= C \phi \Delta t \left(\sum_j \bar{N}_j \kappa \sigma_f^j \right) \end{aligned} \quad (2.2-1)$$

where for a given node:

$$\begin{aligned} \phi &= \phi_1 + \phi_2 && = \text{total node average flux,} \\ \kappa \sigma_f^j &= \frac{\kappa \sigma_{f1} \phi_1 + \kappa \sigma_{f2} \phi_2}{\phi_1 + \phi_2} && = \text{flux averaged fission cross section} \\ &&& \text{for isotope } j, \\ \bar{N}_j &= \int_{\Delta t} N_j(t) dt / \Delta t && = \text{average concentration of isotope } j \\ &&& \text{over } \Delta t \text{ evaluated through analytic} \\ &&& \text{integration,} \end{aligned}$$

C = a constant converting fission energy release per unit volume to MWD/T, specific to the initial fuel composition for the node.

2.2.2 Burnable Absorber Depletion

Shim rods containing a burnable absorber isotope (e.g., ^{10}B) are represented by the depletion chain designated SHIMB in Table 2.1. The SHIMB chain can be used to model the depletion of a single isotope due to neutron absorption starting from its initial concentration. A gadolinium depletion chain is also available. [

]

2.2.3 Fission Product Chains

The fission product chains consisting of $^{135}\text{I} - ^{135}\text{Xe}$ and $^{149}\text{Pm} - ^{149}\text{Sm}$ are included in the depletion model, as indicated in Table 2.1. In the case of xenon, two related calculational capabilities exist in addition to the depletion calculation. These are the equilibrium xenon feedback calculation, and xenon short-term

time-stepping. The latter calculation can be used in place of the normal depletion calculation to obtain nonequilibrium ^{135}I and ^{135}Xe distributions following a short time step, assuming the flux and other nuclide concentrations remain constant. In practice, xenon time-stepping combined with successive flux calculations is used to calculate xenon transients over periods of several hours following a change in operating conditions such as power level or rod bank insertion. The accuracy of such calculations is demonstrated in Reference 2.19.

2.3 Thermal Hydraulics

The ROCS thermal-hydraulic calculational model represents the reactor core as an array of closed, parallel flow channels. Each radial node in the coarse-mesh geometry corresponds to an individual flow channel, and the channels are axially segmented for each ROCS plane. The thermal-hydraulic calculation is thus performed for each node in the active core.

The basic thermal-hydraulic calculation consists of a heat balance calculation for moderator enthalpy and other equation-of-state properties for each axially segmented channel, and a calculation of average fuel temperature in each segment using a burnup and power dependent correlation. The calculated quantities are used to determine the thermal-hydraulic feedback terms entering the flux calculation.

The steady-state heat balance calculation requires specification of channel inlet conditions, consisting of coolant system pressure (P^*), moderator temperature (T_M) and channel mass flow rate (W). The inlet values for T_M and W can be input as either uniform or channel dependent values. The inlet state properties, including moderator density (ρ_M) and enthalpy (H), are then calculated based on 1967 ASME steam table data.^(2.14) The enthalpy rise (ΔH) for a given channel segment (or node) is calculated as

$$\Delta H = Q/W \quad (2.3-1)$$

and the average enthalpy in the node is

$$H = H_{in} + \Delta H/2 \quad (2.3-2)$$

The thermal power in the node, (Q), is obtained from the two-group node-average flux values, i.e.,

$$Q = V \cdot PFACT \cdot (\kappa \Sigma_{f1} \phi_1 + \kappa \Sigma_{f2} \phi_2) \quad (2.3-3)$$

where V is the nodal volume and PFACT is a constant converting fission energy rate to units of thermal power used in Eq. (2.3-1). The average moderator state properties including T_M and ρ_M are obtained for each node as functions of H and P^* based on the steam tables.

The fuel temperature correlation used in the ROCS code is based upon detailed calculations performed with the FATES code (2.15) which accounts for exposure- and linear heat rate-dependent physical changes in the fuel pellet, clad and pellet-to-clad gap.

The fuel temperature correlation has the polynomial form

$$T_F = T_M + \left(\sum_{i=0}^2 B_i * E^i \right) * KWFT + \left(\sum_{i=0}^3 C_i * E^i \right) * KWFT^2 \quad (2.3-4)$$

where T_F = average fuel temperature ($^{\circ}F$)
 T_M = moderator temperature ($^{\circ}F$)
 E = fuel exposure (MWD/T)
 KWFT = average fuel pin linear power density (KW/ft)

The quantities B_i and C_i are the precalculated polynomial coefficients specific to the fuel design and dimensionality of the ROCS calculation (i.e., 2-D or 3-D). A detailed description of the development and verification of the fuel temperature correlation is given in Reference 2.16.

The ROCS neutronics calculation is linked to optional independent feedback calculations for thermal-hydraulic parameters (moderator density, moderator temperature, fuel temperature) and for equilibrium ^{135}I - ^{135}Xe distributions. The thermal-hydraulic calculation (Section 2.3) is performed iteratively with the flux calculation when any combination of thermal-hydraulic feedbacks is specified. For each feedback variable specified, the macroscopic cross sections used in the flux calculation are updated through the appropriate feedback term in Eq. (2.1-55). In the case of xenon, the macroscopic cross sections are updated each iteration cycle using calculated ^{135}I and ^{135}Xe equilibrium concentrations based on the two-group flux distribution from the previous iteration. The number of feedback iterations is governed by independent convergence criteria for each feedback parameter, so that the final flux solution is obtained after all specified feedbacks have converged.

In addition to the above feedback models, the ROCS code contains optional eigenvalue search models for the following control variables: control rod bank insertion, soluble boron concentration, reactor power level, and inlet moderator temperature. The search calculations employ numerical iteration techniques which update the specified control variable to obtain convergence on the search eigenvalue, and are generally used along with feedback calculations. The power level and inlet temperature searches require use of thermal-hydraulic feedbacks. These latter search calculations are performed after alternate feedback iterations while the boron and rod search calculations are performed after each feedback iteration.

2.5 Fuel Pin Peaking

The ROCS code has the capability of performing pin peaking calculations for each node in two- or three-dimensional core geometries through use of the MC module. The MC module uses an imbedded fine-mesh diffusion theory method for obtaining pin power distributions from coarse-mesh calculations^(2.18). The calculative sequence is illustrated in Figure 2-10 and a description of the details follows. A method has been developed for determining diffusion coefficients which, when combined with the finite difference formulation of MC, permits the inclusion of transport effects in a rigorous fashion.

2.5.1 Diffusion Theory For The Imbedded Calculaton

The nodal imbedded, fine-mesh method uses a mesh-centered, two-group formulation of the two-dimensional diffusion equation with one mesh per pin cell. The resulting equations are solved in a boundary source mode. Integration of the two-dimensional diffusion equation over each uniform fine-mesh cell with volume V_{ij} gives:

$$L_{ij} + \Sigma_{ij} V_{ij} \phi_{ij} = \frac{\chi}{\lambda} \nu \Sigma_{fij} V_{ij} \phi_{ij} \quad (2.5-1)$$

This equation is in one-group form in order to simplify the notation. Implementation in the ROCS code uses a full two-group formalism. The finite difference form of the leakage operator is derived from Green's theorem:

$$-L_{ij} = \int_{V_{ij}} dV \nabla \cdot D(x,y) \nabla \phi(x,y) = \int_{S_{ij}} dS \cdot D(x,y) \nabla \phi(x,y) \quad (2.5-2)$$

For a surface with the normal in direction k the surface integral is approximated by the following form:

$$L_{ij}(k) = D_{ij}^k \phi_{ij} - D_n^{-k} \phi_n \quad (2.5-3)$$

where n denotes the neighbor of mesh ij in direction k . Note that

directionally dependent diffusion coefficients are permitted in this formalism. The fact that Eq. (2.5-3) is linear in the diffusion coefficients facilitates the incorporation of transport effects as shown below.

Determination of Diffusion Coefficients

Since the imbedded calculation is done with diffusion theory it is important that diffusion parameters are chosen so as to compensate for the differences between transport and diffusion theory. The method chosen uses simple flux-volume weighted cross sections direct from the transport calculation (by the DIT code) with diffusion coefficients determined for each cell within each assembly type. The diffusion coefficients are determined so that when they are used in Eq. (2.5-3), the net leakage across each cell boundary together with the cell average flux, ϕ_{ij} , exactly yields the net leakage and average flux from a DIT transport calculation performed for the same assembly geometry. Given the net leakages and fluxes from the transport calculation (L^T and ϕ^T) the following equation system results for determining directionally dependent diffusion coefficients:

$$L_{ij}^T(k) = D_{ij}^k \phi_{ij}^T - D_n^{-k} \phi_n^T \quad \begin{matrix} ij=(1, N_{\text{Mesh}}) \\ k=(1,4) \end{matrix} \quad (2.5-4)$$

where n denotes the neighbor of mesh ij in direction k and N_{Mesh} is the total number of cells.

There are $4 \times N_{\text{Mesh}}$ equations of this form with $4 \times N_{\text{Mesh}}$ unknown values of D_{ij}^k . Note that for the general case, $L_{ij}^T(k)$ will include the external boundary conditions imposed upon the transport theory assembly calculation. This then permits a realistic representation of the assembly location in the core. However, when the assembly transport computation is performed with zero external net currents, Eqs. (2.5-4) are not independent. In this case, DIT will have replaced the external leakage by a buckling-mode type leakage representation so that the neutron balance contains a term of

the type $B^2 \cdot d \cdot \text{SUM}(V \cdot \phi^T)_{ij}$. The node-averaged diffusion coefficient, d , is determined from a B1 computation for the homogenized assembly. An additional equation is thus obtained by requiring that the flux-volume weighting of all cell diffusion coefficients be consistent with this value of d :

$$B^2 \cdot \text{SUM}_{ij} D_{ij} (V\phi)_{ij} = B^2 \cdot d \text{SUM}_{ij} (V\phi)_{ij} \quad (2.5-5)$$

where

$$D_{ij} = \frac{1}{4} \text{SUM}_{k=1}^4 D_{ij}^k \quad (2.5-6)$$

When the D_{ij}^k from Eq. (2.5-4) are used with the transport calculated cell flux-volume weighted cross sections, Σ_{ij} , these diffusion coefficients will yield exactly

$$\phi_{ij} = \phi_{ij}^T \quad (2.5-7)$$

when the diffusion equation is applied to the same problem as was solved with transport theory. The diffusion coefficients therefore have the property of conserving cell averaged fluxes, reaction rates, and net leakages across cell boundaries. Thus, MC has the capability to effectively reproduce DIT local power distributions.

Having determined diffusion coefficients that exactly reproduce average fluxes, reaction rates, and net currents from transport theory for a particular geometry, it is then asserted that they are universally applicable independent of the size of the flux gradients seen in the core. Although not exact, this is a common assumption. Also, directionally averaged diffusion coefficients, Eq. (2.5-6), are used for ordinary applications. These two assumptions do not substantially affect the degree of agreement with transport theory results as seen later in Figures 2-11 through 2-13.

2.5.2 Boundary Currents for the Imbedded Calculation

The nodal diffusion equations, Eqs. (2.5-1) and (2.5-3), are solved

as a boundary source problem for the imbedded calculation. The partial in-currents on each nodal face and the global eigenvalue are supplied by the ROCS coarse-mesh calculation.

After completion of the fine-mesh imbedded calculation, the fine-mesh power distribution is renormalized to the coarse-mesh power level to assure that coarse-mesh and fine-mesh node average powers and burnups will remain the same during depletion.

2.5.3. Cross Section Model For The Imbedded Calculation

The MC imbedded calculation uses a macroscopic cross section model based upon interpolation of multi-dimensional macroscopic table sets. These tables are created by the DIT code for all assembly types, [

[

2.5.4 Local Power Distributions

This section presents verification of the MC nodal imbedded method for obtaining local power distributions from coarse mesh calculations. This is achieved through comparisons of MC with transport theory (i.e., DIT) in assembly calculations and ROCS and MC with PDQ fine-mesh diffusion theory in two-dimensional quarter core calculations.

Comparisons have been made of MC with DIT for both shimmed and unshimmed assemblies. Figures 2-11 through 2-13 illustrate the agreement between MC and transport theory. Figure 2-11 shows the relative differences in the local two-group fluxes. This comparison

is for an octant of an unshimmed assembly with zero net external leakage. Directionally averaged diffusion coefficients specific to each individual cell in the octant were used, so that the level of agreement is essentially determined by the numerical accuracies of the diffusion and transport calculations.

Figures 2-12 and 2-13 compare MC fission rates with transport theory for unshimmed and shimmed octant assemblies respectively. The assembly in Figure 2-12 has zero net external leakage, while Figure 2-13 represents a core location with a global power tilt. Both MC calculations used directionally averaged diffusion coefficients obtained from a zero net boundary current calculation. []
[] The standard deviations of differences are [] respectively and are representative of the MC model used below. This close agreement between MC and transport theory fission rates illustrates the accuracy of the assumption of universally applicable diffusion coefficients.

The PDQ fine-mesh diffusion theory code has been used as a benchmark for comparing MC performance in predicting peak-to-assembly-average pin power (peak pin/box factor) in quarter core ROCS calculations. The PDQ model used in these comparisons has transport theory adjustments to reproduce pin-to-box factors from direct DIT calculations when applied to an individual assembly. The results of these comparisons are found in Figures 2-14 through 2-17 which show the relative differences in peak pin/box factors for all assemblies from two-dimensional midplane calculations.

Figures 2-14 through 2-16 show the differences in assembly peak pin/box factors obtained from unrodded ROCS, MC and PDQ calculations at BOC, MOC and EOC respectively. The ROCS, MC and PDQ models utilized independent cross section tablesets obtained from DIT calculations. The good agreement in pin/box factors shown by the quarter-core maps is indicative of the agreement in local power distribution observed within the individual assemblies. Figure 2-17

shows the pin/box factor differences at BOC for a calculation with the lead rod bank inserted. In this case the MC model utilized macroscopic rod cross sections for the rodded locations. The differences in pin/box factors are comparable to those in the unrodded cases. The largest differences are in low power assemblies where the absolute assembly pin peak is not limiting.

Table 2.2 summarizes the means and standard deviations (in both absolute and relative terms) from the ROCS and MC vs. PDQ comparisons. Overall, the mean relative difference is [] and the associated standard deviation is []. The uncertainty in peak-to-assembly-average power, based on this table, is combined with the uncertainties in assembly power peaks (taken from Section 4.1.2) in Chapter 5. The least favorable values, corresponding to the BOC rodded case in Table 2.2, are used in Chapter 5.

2.6 References

- 2.1. C. P. Robinson and J. D. Eckard, Jr., "A Higher Order Difference Method for Diffusion Theory," Trans. Am. Nucl. Soc., 15, 297 (1972), and Combustion Engineering Report TIS-3351.
- 2.2. C. P. Robinson and R. R. Lee, "Experimental Verification of the 3-D Coarse Mesh Method of Robinson and Eckard," Trans. Am. Nucl. Soc., 17, 476 (1973).
- 2.3. I. C. Rickard, N. R. Gomm, and T. G. Ober, "Calculational and Experimental Verification of the Combustion Engineering Coarse Mesh Physics Simulator," Trans. Am. Nucl. Soc., 24, 340 (1976), and Combustion Engineering Report TIS-5023.
- 2.4. T. G. Ober, J. C. Stork, I. C. Rickard, and J. K. Gasper, "Theory, Capabilities, and Use of the Three-Dimensional Reactor Operation and Control Simulator (ROCS)," Nucl. Sci. Eng., 64, 605 (1977).
- 2.5. T. G. Ober, J. C. Stork, R. P. Bandera and W. B. Terney, "Extension of the ROCS Coarse-Mesh Physics Simulator to Two Energy Groups," Trans. Am. Nucl. Soc., 28, 763 (1978), and Combustion Engineering Report TIS-5856.
- 2.6. W. B. Terney, R. P. Bandera, and T. G. Ober, "Qualification of C-E's 3-D Spatial Neutronics Code for PWR Analysis," Trans. Am. Nucl. Soc. 30, 227 (1978), and Combustion Engineering Report TIS-6011.
- 2.7. R. P. Bandera, P. H. Gavin, P. C. Rohr, "Evaluation of Coarse-Mesh Methods in Calculation of Safety-Related Parameters," Trans. Am. Nucl. Soc., 35, 560 (1980).
- 2.8. W. R. Cadwell, "PDQ-7 Reference Manual," WAPD-TM-678, Bettis Atomic Power Laboratory (1969).
- 2.9. H. Finnemann, H. Raum, "Nodal Expansion Method for the Analysis of Space-Time Effects in LWRs", Proceedings of NEACRP Specialists Meeting, Paris, November 26 -28, 1979.

- 2.10 W. B. Terney, "Albedo-Adjusted Fast-Neutron Diffusion Coefficients in Reactor Reflectors," Nucl. Sci. Eng., 57, 239 (1975).
- 2.11. H. Finneemann, F. Bennewitz, M. R. Wagner, "Interface Current Techniques for Multidimensional Reactor Calculations", Atomkernenergie, 30, 123 (1977).
- 2.12. H. Finneemann, "A Consistent Nodal Method for the Analysis of Space-Time Effects in Large LWRs", Proc. of joint NEARCP/CSNI Specialists Meeting, Munich, January 22 -24, 1975.
- 2.13 P. E. Rohan, S. G. Wagner, S. E. Ritterbusch, "HERMITE: A Multi-dimensional Space-Time Kinetics Code for PWR Transients," Combustion Engineering, Inc. Report CENPD-188-A (1976).
- 2.14. C. A. Meyer et al., Thermodynamic and Transport Properties of Steam, American Society of Mechanical Engineers (1967).
- 2.15. "C-E Fuel Evaluation Model," CENPD-139, Rev.-1 (1974).
- 2.16. P. H. Gavin and P. C. Rohr, "Development and Verification of a Fuel Temperature Correlation for Power Feedback and Reactivity Coefficient Application," Trans. Am. Nucl. Soc., 30, 715 (1978).2.11.
- 2.17. A. Jonsson, W. B. Terney, M. W. Crump, "Evaluation of Uncertainty in the Nuclear Power Peaking Measured by the Self-Powered, Fixed In-Core Detector System," CENPD-153-P, Rev. 1-P-A, May 1980.
- 2.18. S. Grill, A. Jonsson, "A Nodal Imbedded Method to Recover Local Power Peaking From Coarse Mesh Reactor Calculations", Trans. Am. Nucl. Soc., 35, 580 (1980).
- 2.19 I. C. Rickard, N. R. Gomm, T. G. Ober, "Calculational and Experimental Verification of the Combustion Engineering Coarse Mesh Simulator", Trans. Am. Nucl. Soc., 24, 340 (1976), and Combustion Engineering Report TIS-5023.

Figure 2-1
ROCS LOGIC FLOW

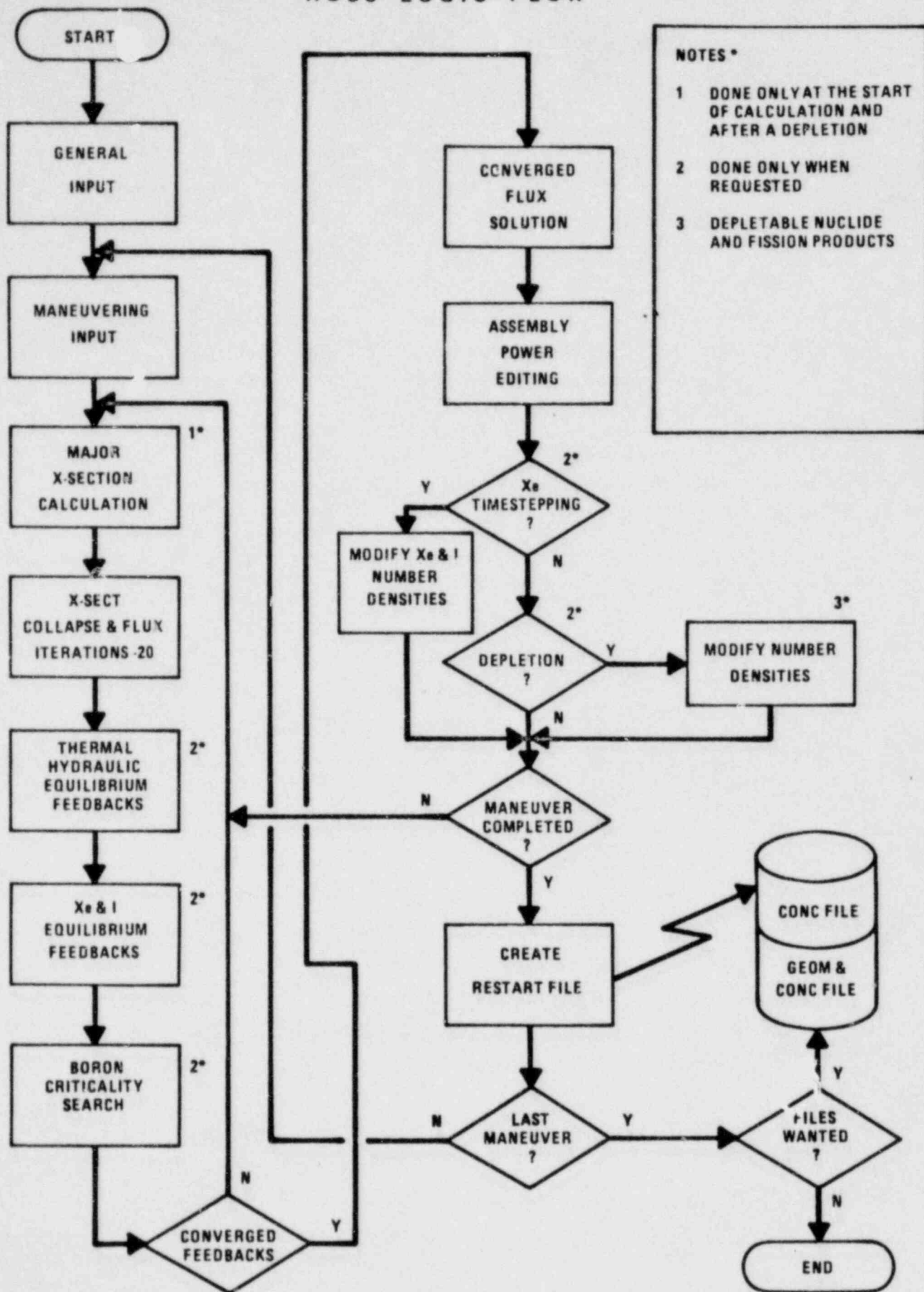


FIGURE 2-2

NODAL CELL GEOMETRY

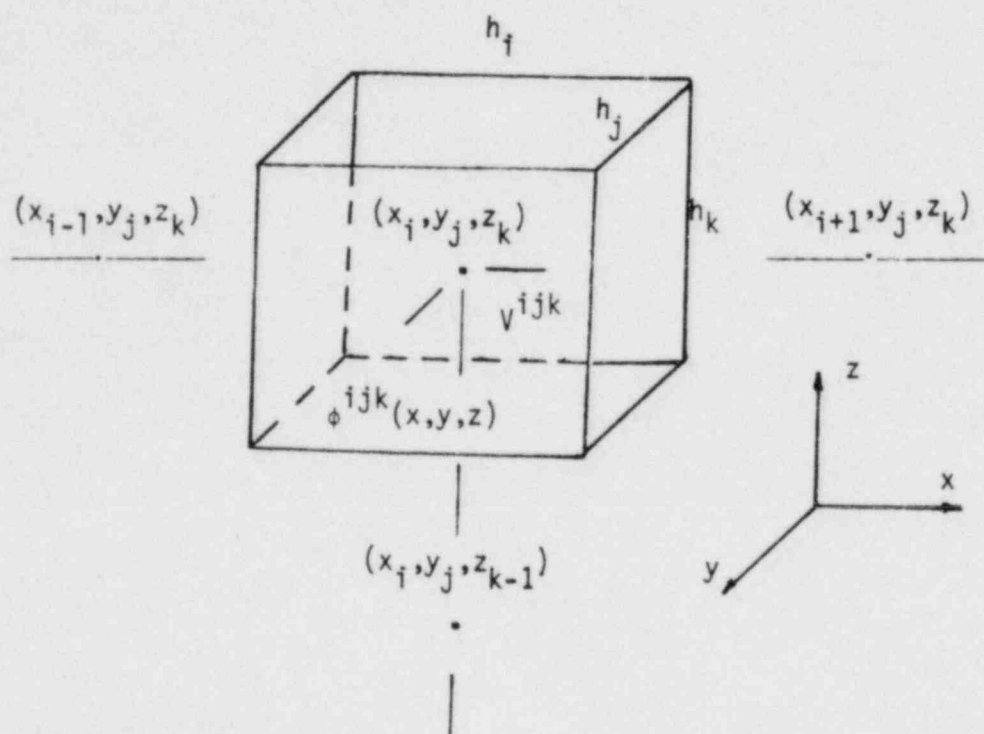


FIGURE 2-3

TWO-GROUP HOD SOLUTION METHOD

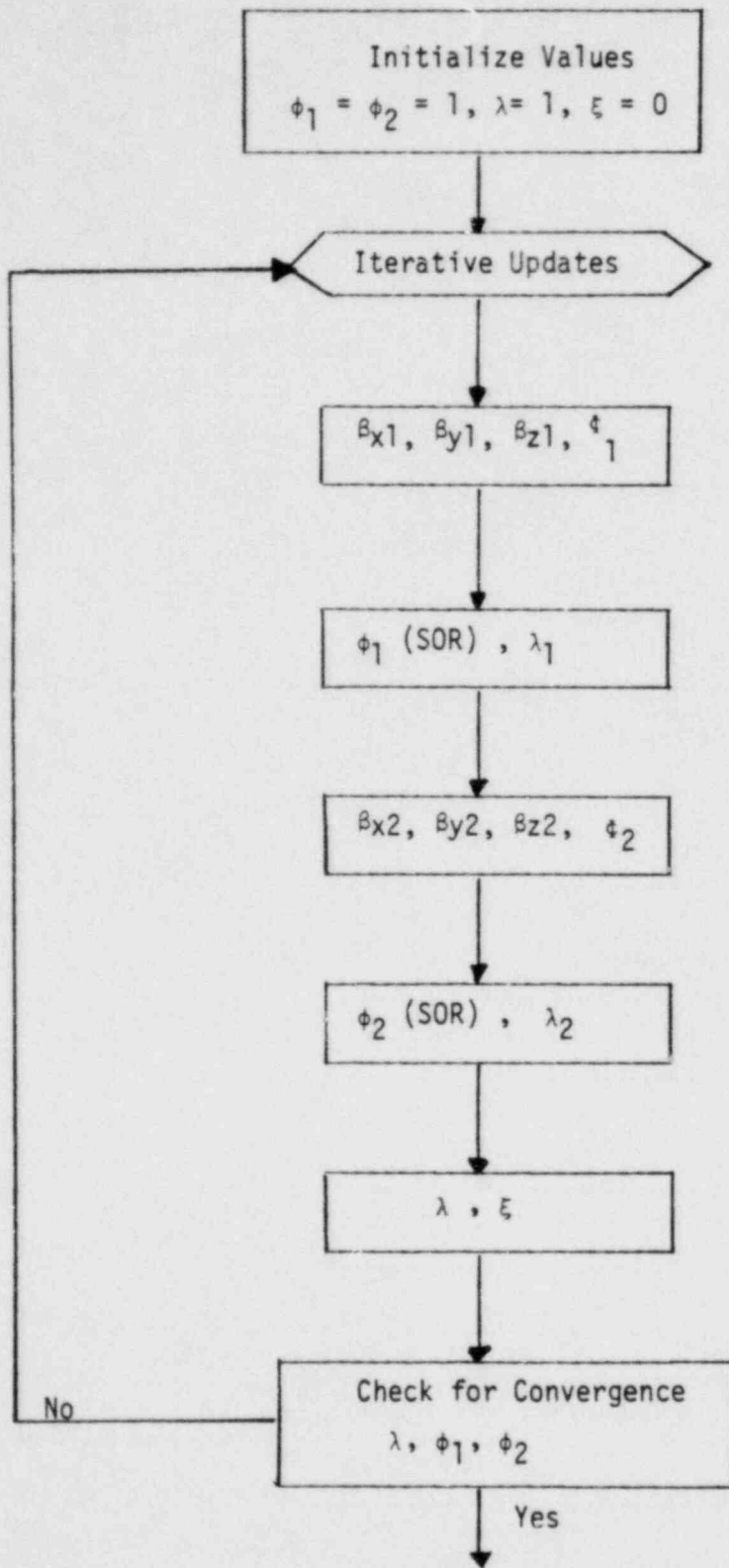


Figure 2-4
2D MIDPLANE POWER DISTRIBUTION COMPARISON
NEM AND HOD vs PDQ AT BOL

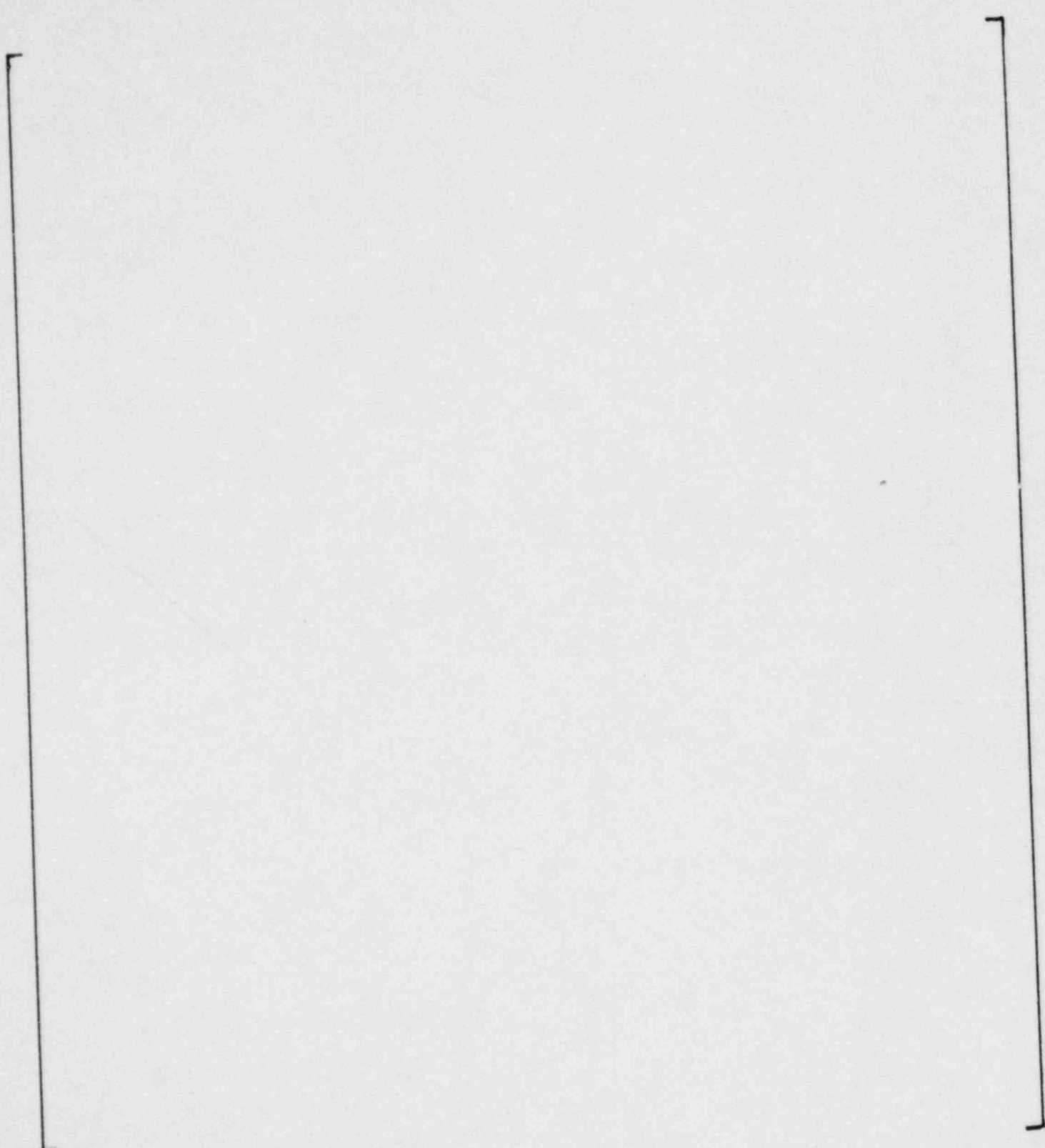


Figure 2-5
2D MIDPLANE POWER DISTRIBUTION COMPARISON
NEM AND HOD vs PDQ AT MOC

Figure 2-6
2D MIDPLANE POWER DISTRIBUTION COMPARISON
NEM AND HOD vs PDQ AT EOC

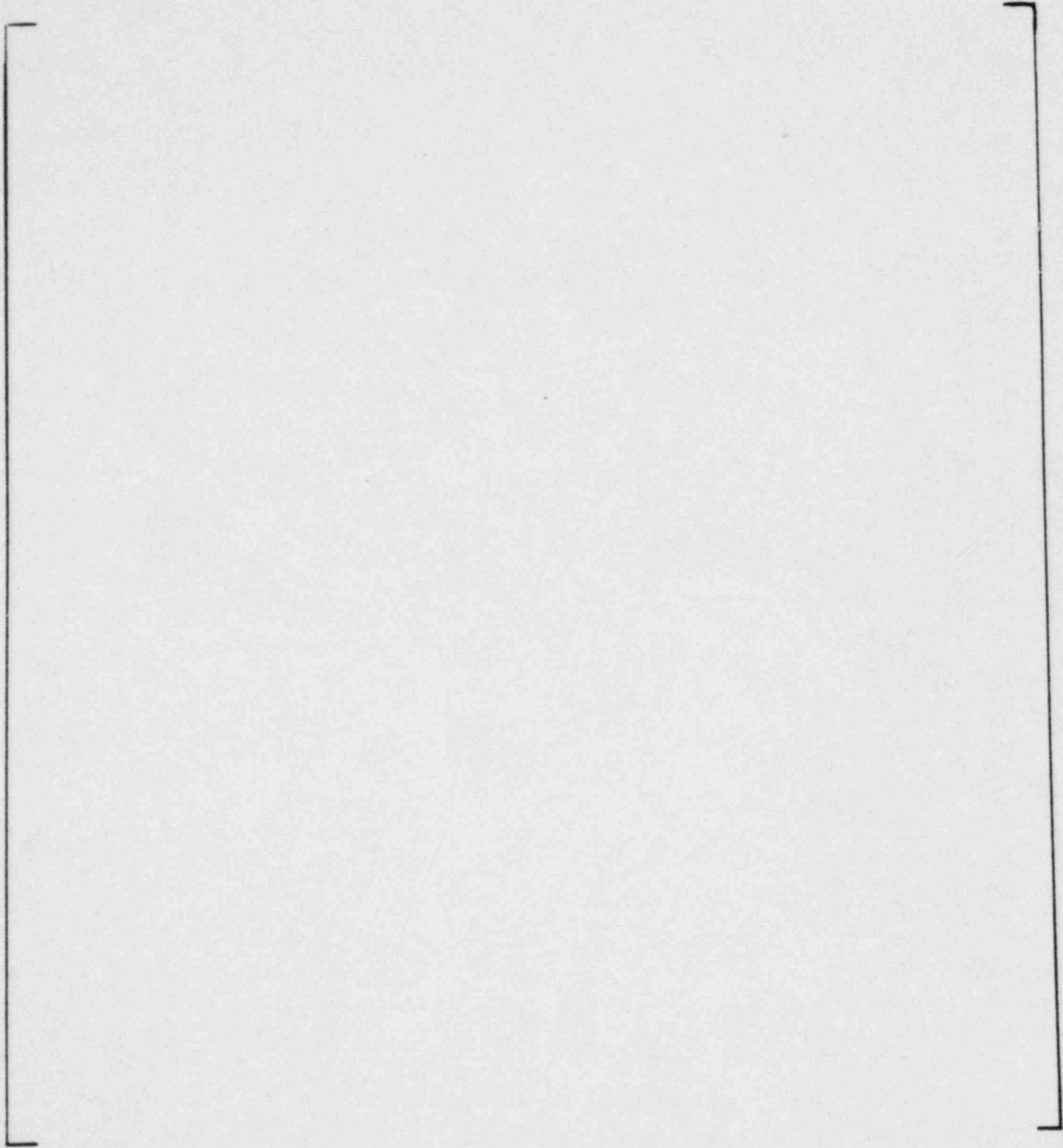


Figure 2-7
RADIAL AVERAGED AXIAL POWER DISTRIBUTION vs PERCENT OF CORE HEIGHT
FULL POWER, BEGINNING OF LIFE

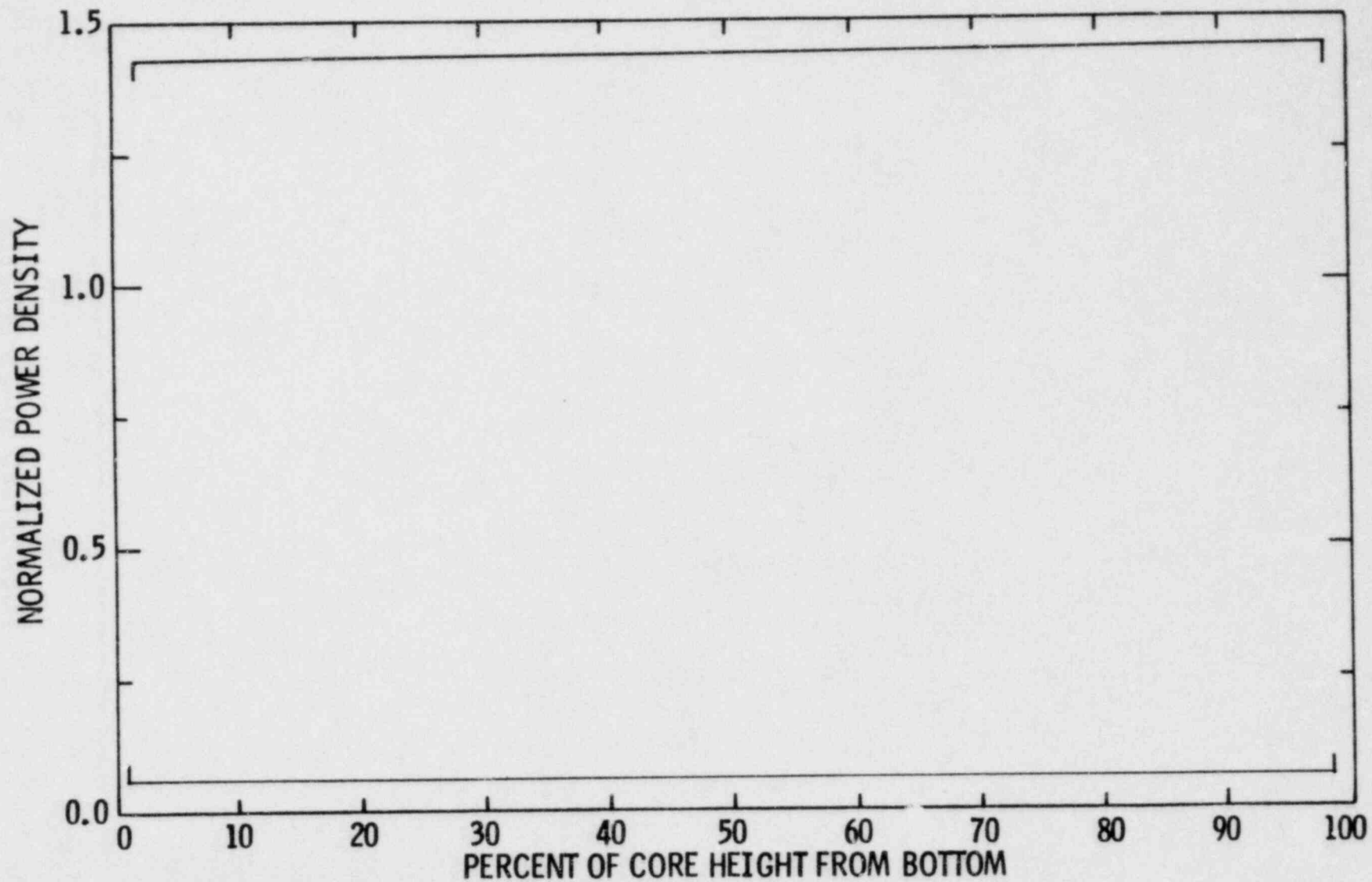


Figure 2-8
MIDPLANE POWER DISTRIBUTION FROM 3D CALCULATIONS
NEM AND HOD COMPARED
FULL POWER, BEGINNING OF LIFE

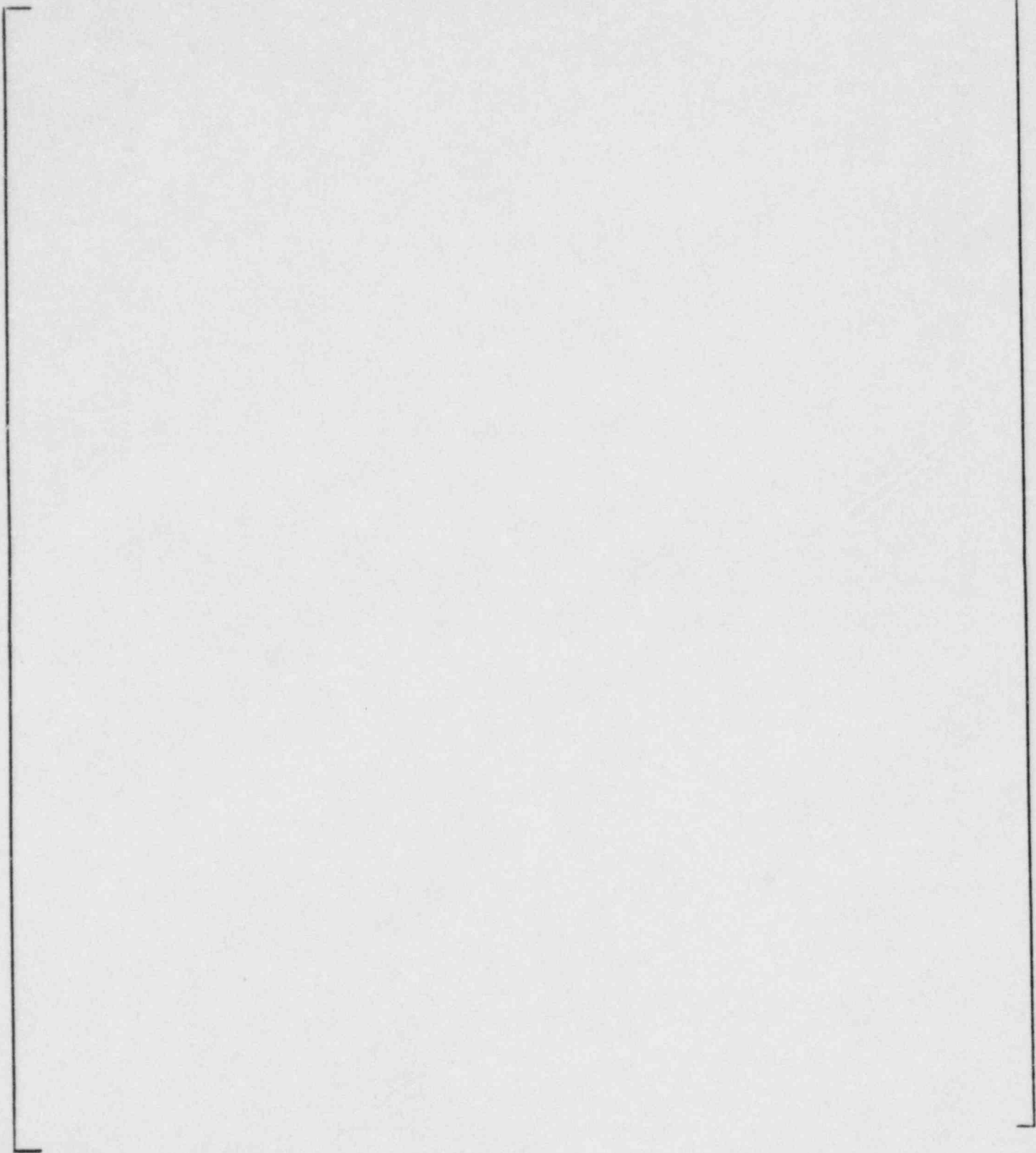


Figure 2-9
NEM-ROCS, RMS AND MAXIMUM PERCENT DIFFERENCES
IN THE RADIAL POWER DISTRIBUTION vs PERCENT
OF CORE HEIGHT

350 MW/T
50% Power

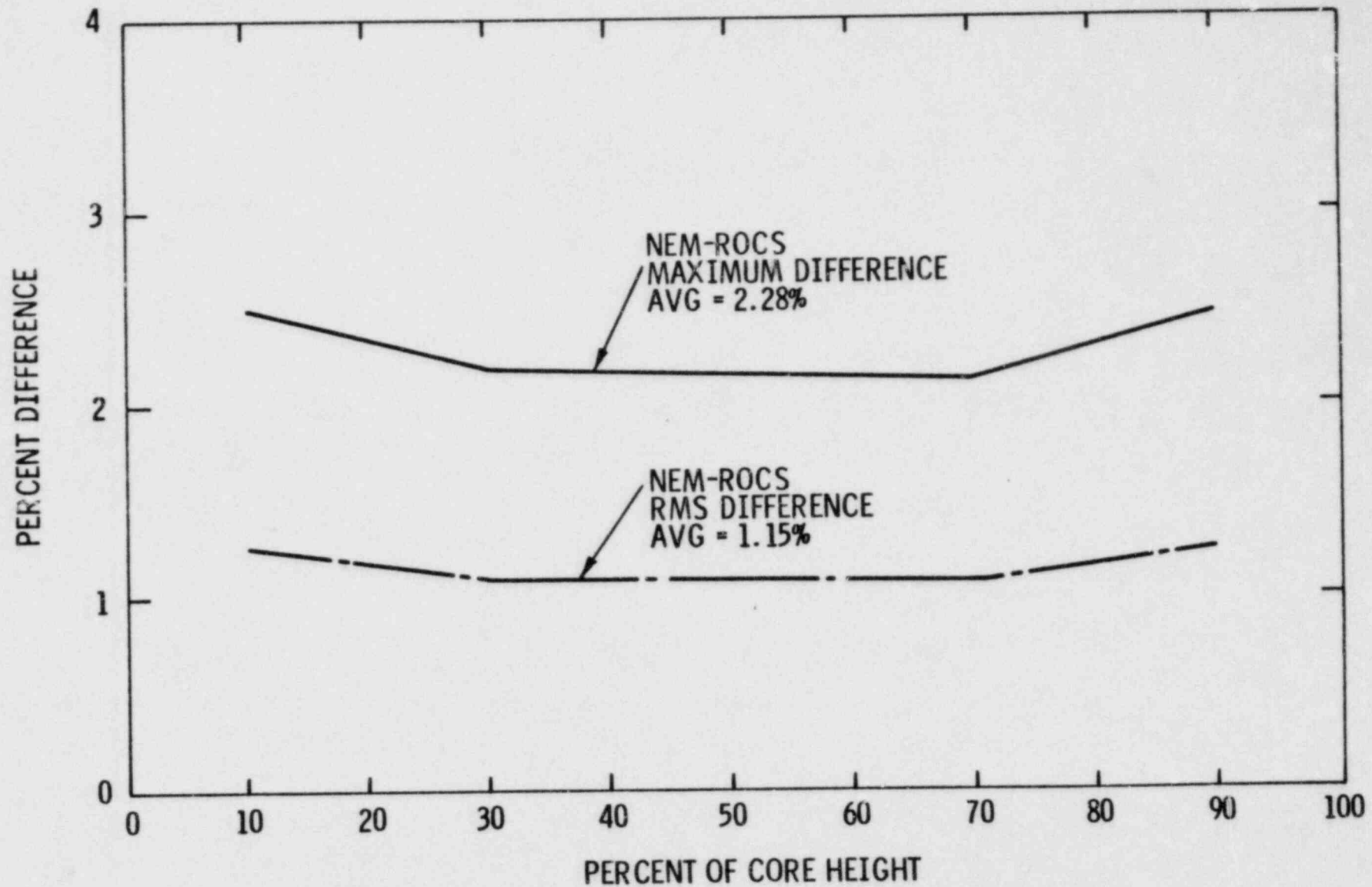


Figure 2-10
PIN PEAKING IN COARSE MESH CALCULATIONS

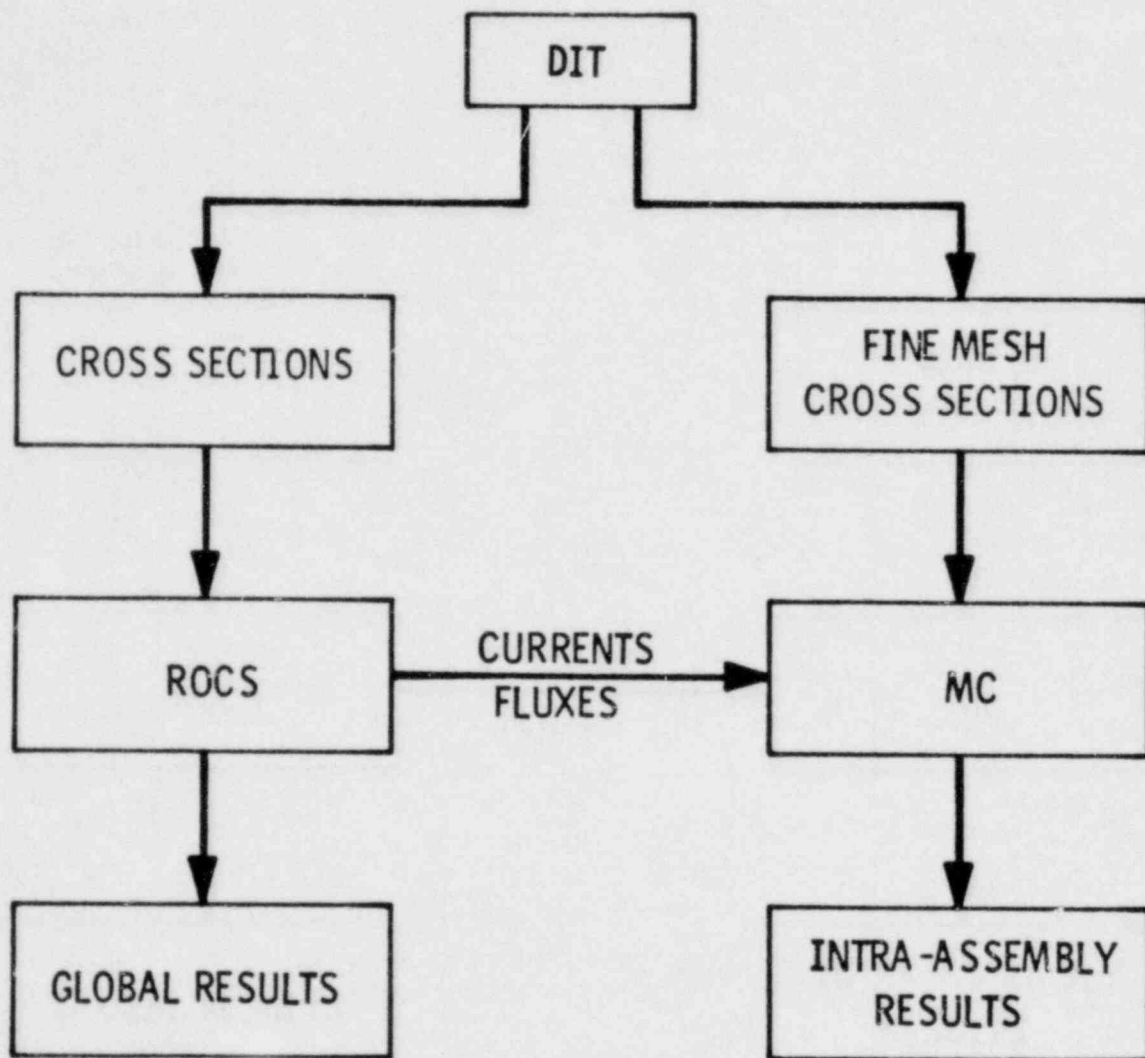


Figure 2-11
 COMPARISON OF DIT TRANSPORT THEORY FLUXES WITH MC
 DIFFUSION THEORY FLUXES

$$\frac{\text{DIT-MC}}{\text{DIT}} \times 100$$

<div style="border: 1px solid black; padding: 5px; width: fit-content; margin-left: auto; margin-right: auto;"> % DIFF. GRP. 1 % DIFF. GRP. 2 </div>								INSTR. WATER	
								-0.06 -0.08	-0.05 -0.08
						-0.05 -0.04	-0.05 -0.08		
				0.05 0.04	0.05 -0.03	-0.05 -0.03			
WATER				-0.05 -0.01	-0.05 -0.04	-0.05 -0.01			
-0.06 0.06				0.05 -0.01	-0.05 -0.03	-0.05 0.00			
		-0.05 0.03	-0.05 0.17	0.05 -0.02	0.05 -0.06	0.05 -0.02	-0.04 -0.11		
		-0.05 0.06	0.05 0.06	-0.05 0.05	-0.05 -0.05	-0.04 0.07	0.05 -0.01	0.05 -0.11	
-0.05 0.32	0.05 0.04	-0.05 0.05	-0.05 0.05	0.05 0.05	0.05 -0.05	0.05 -0.14	0.05 -0.14		

Figure 2-12
 COMPARISON OF FISSION RATES
 DIT (K=1) vs MESH CENTERED DIFFUSION THEORY

	k_{∞}					
DIT (K = 1)	1.3499					
MC DIFF THEORY	1.3502					

$$\%DIFF = \frac{(DIT - MC)}{DIT} \times 100$$

						W	
					+0.4	+0.6	
				+0.3	-1.0	+0.1	
			W	+0.4	0.0	+0.9	
				+0.3	-0.2	+0.4	
		+0.5	+0.6	+0.5	+0.1	-0.9	+0.2
	-0.2	-0.5	+0.2	+0.1	-0.7	-0.7	-0.7

W = WATERHOLE

Figure 2 - 13
COMPARISON OF FISSION RATES IN A LOCATION WITH A
POWER TILT - MC DIFFUSION THEORY vs TRANSPORT THEORY

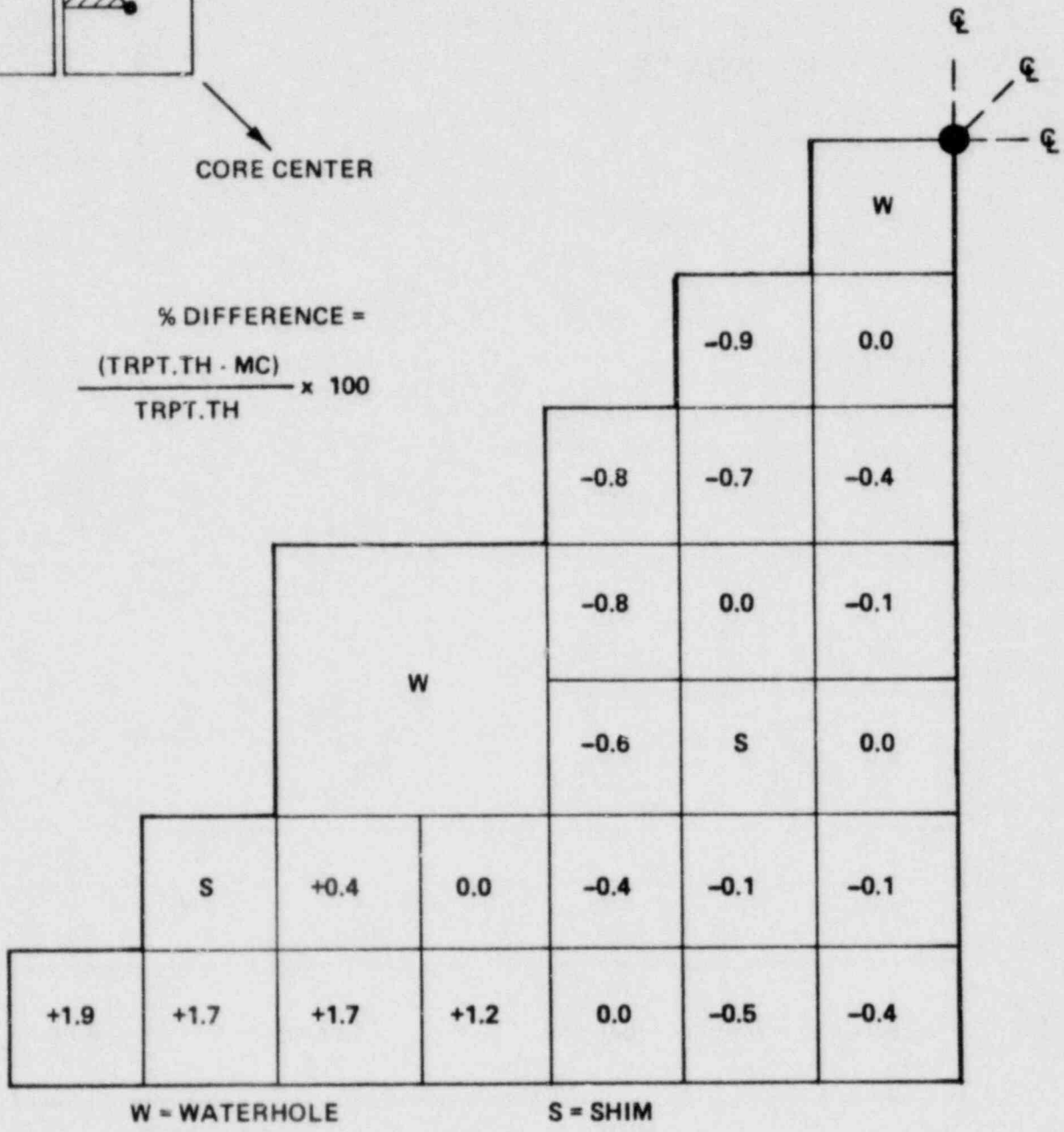
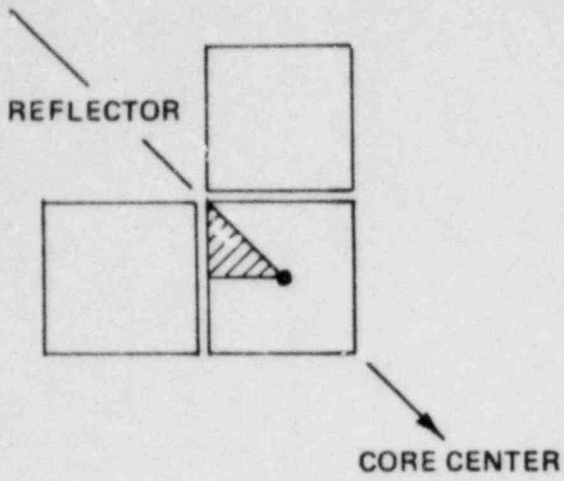


Figure 2-14
COMPARISON OF PIN/BOX DIFFERENCES BETWEEN
ROCS/MC AND PDQ
BOC
UNRODDED

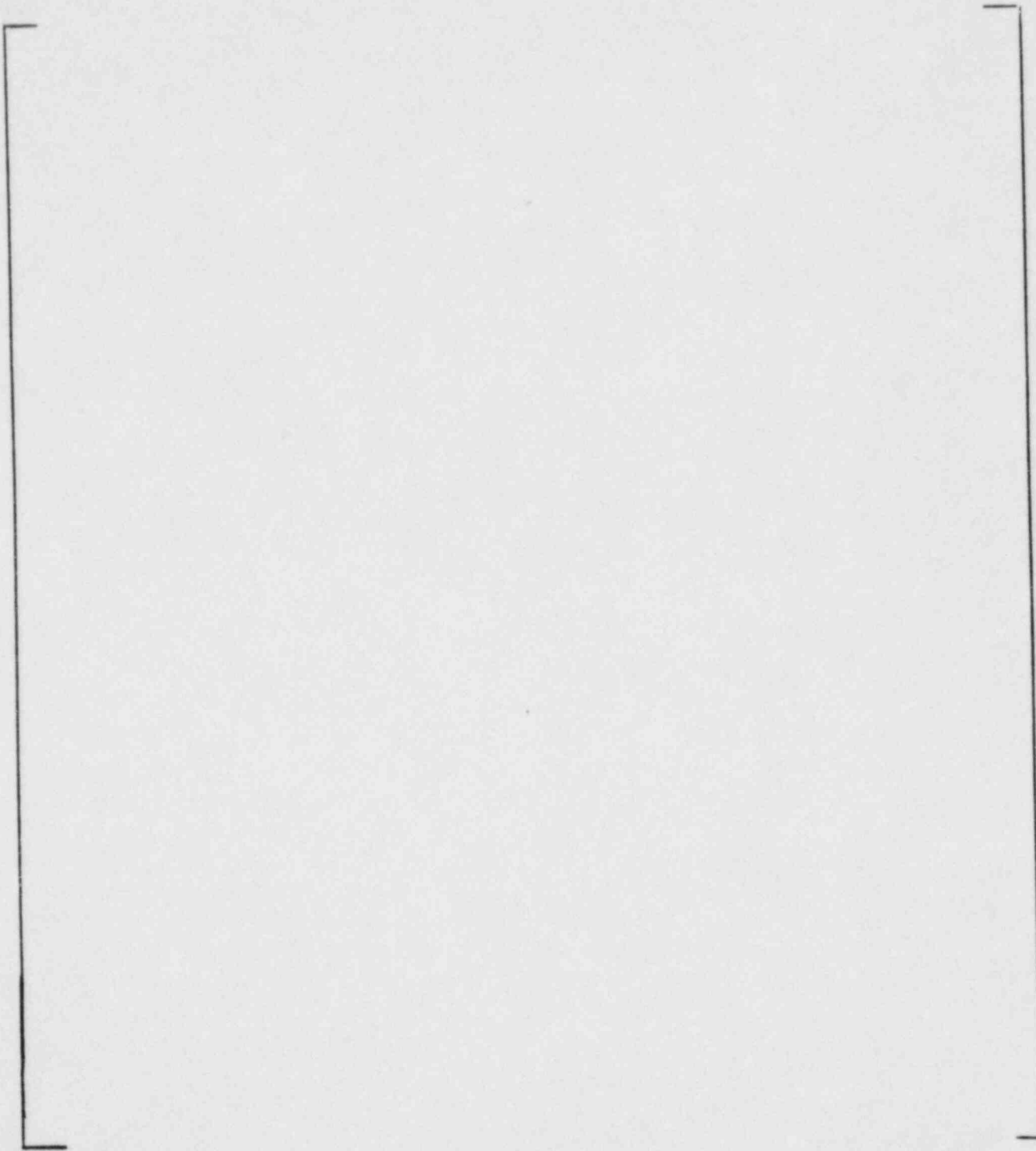


Figure 2-15
COMPARISON OF PIN/BOX DIFFERENCES BETWEEN
ROCS/MC AND PDQ
MOC
UNRODDED

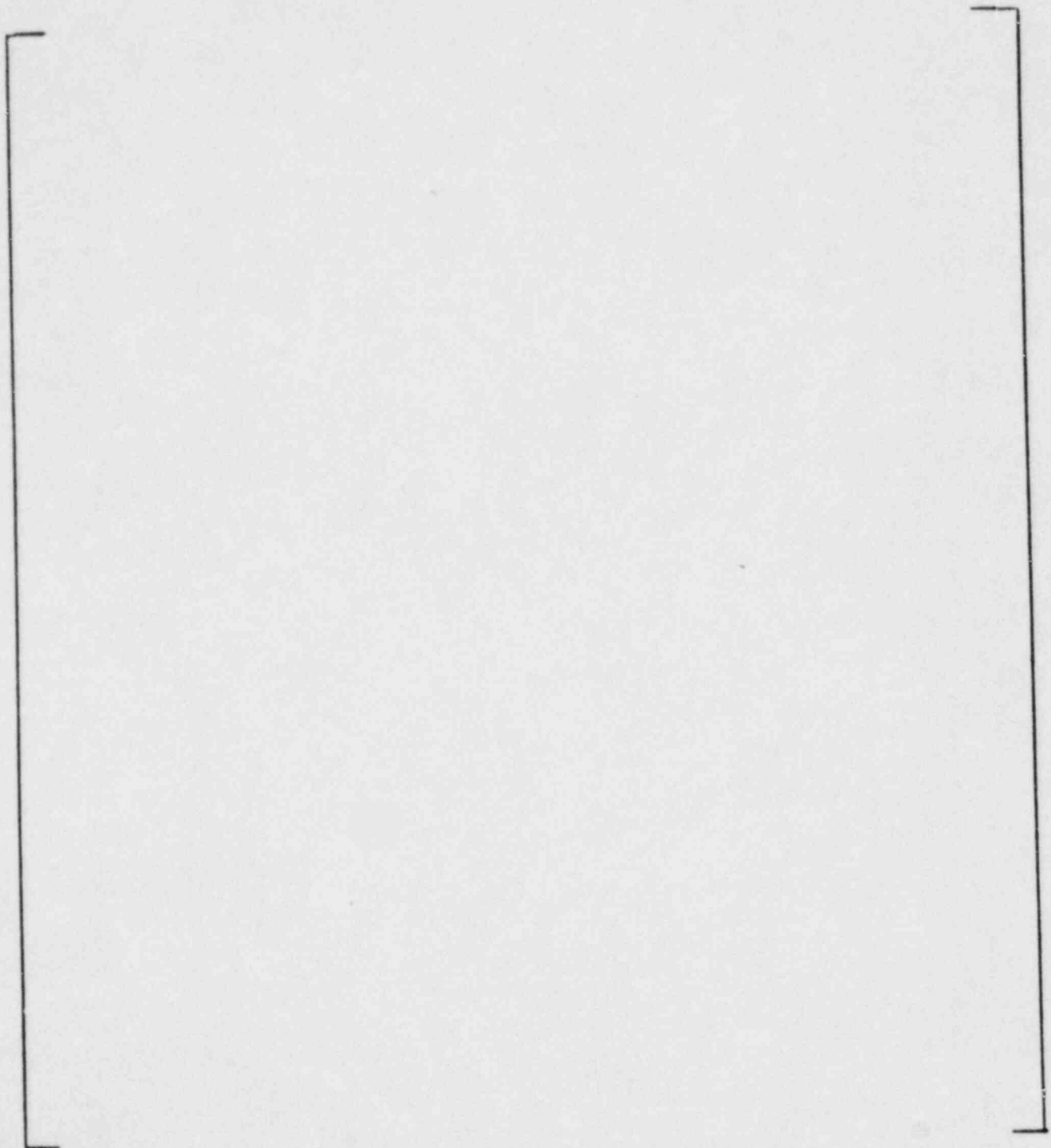


Figure 2-16
COMPARISON OF PIN/BOX DIFFERENCES BETWEEN
ROCS/MC AND PDD
EOC
UNRODDED

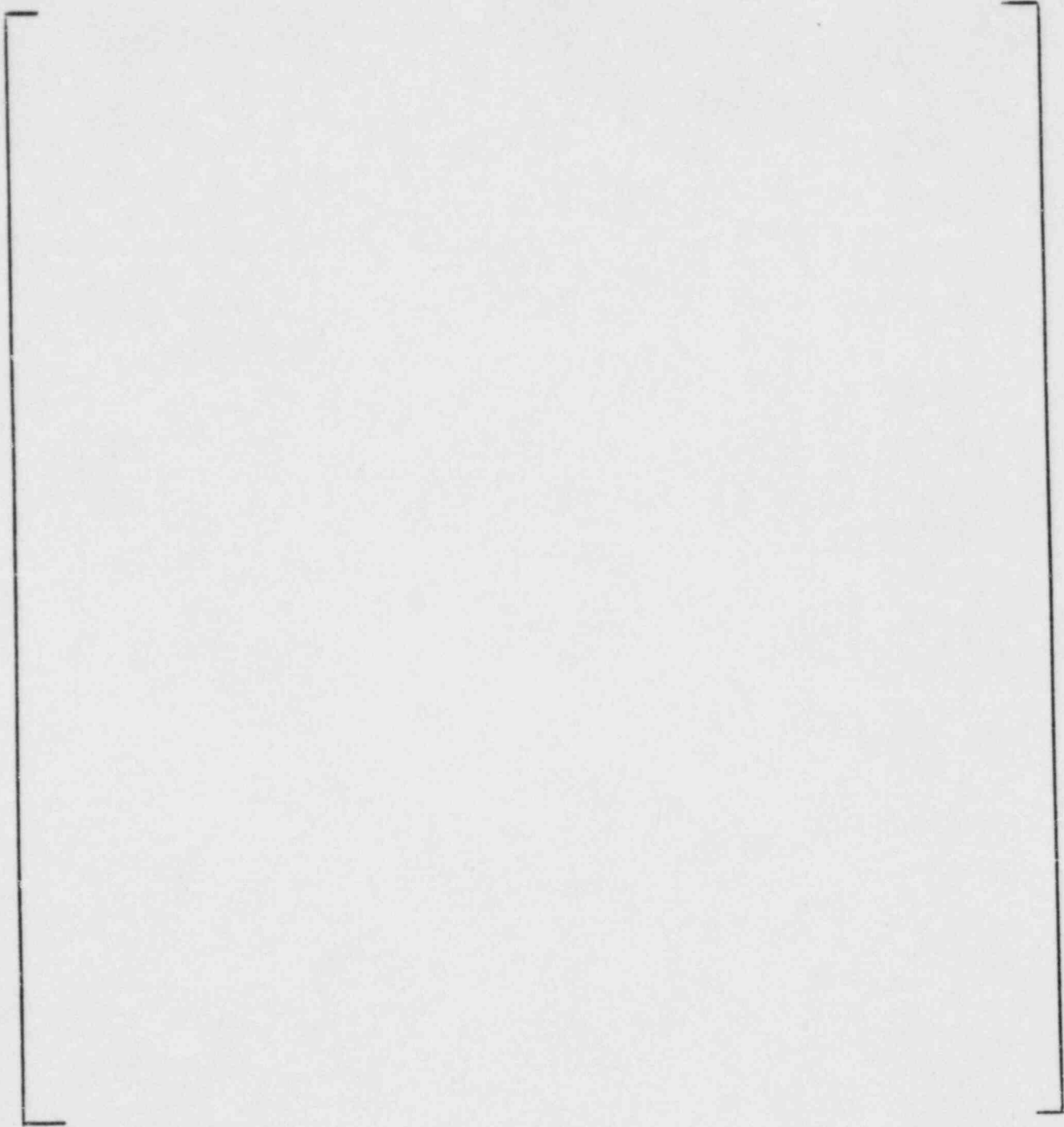


Figure 2-17
COMPARISON OF PIN/BOX DIFFERENCES BETWEEN
ROCS/MC AND PDQ
BOC
LEAD ROD BANK INSERTED

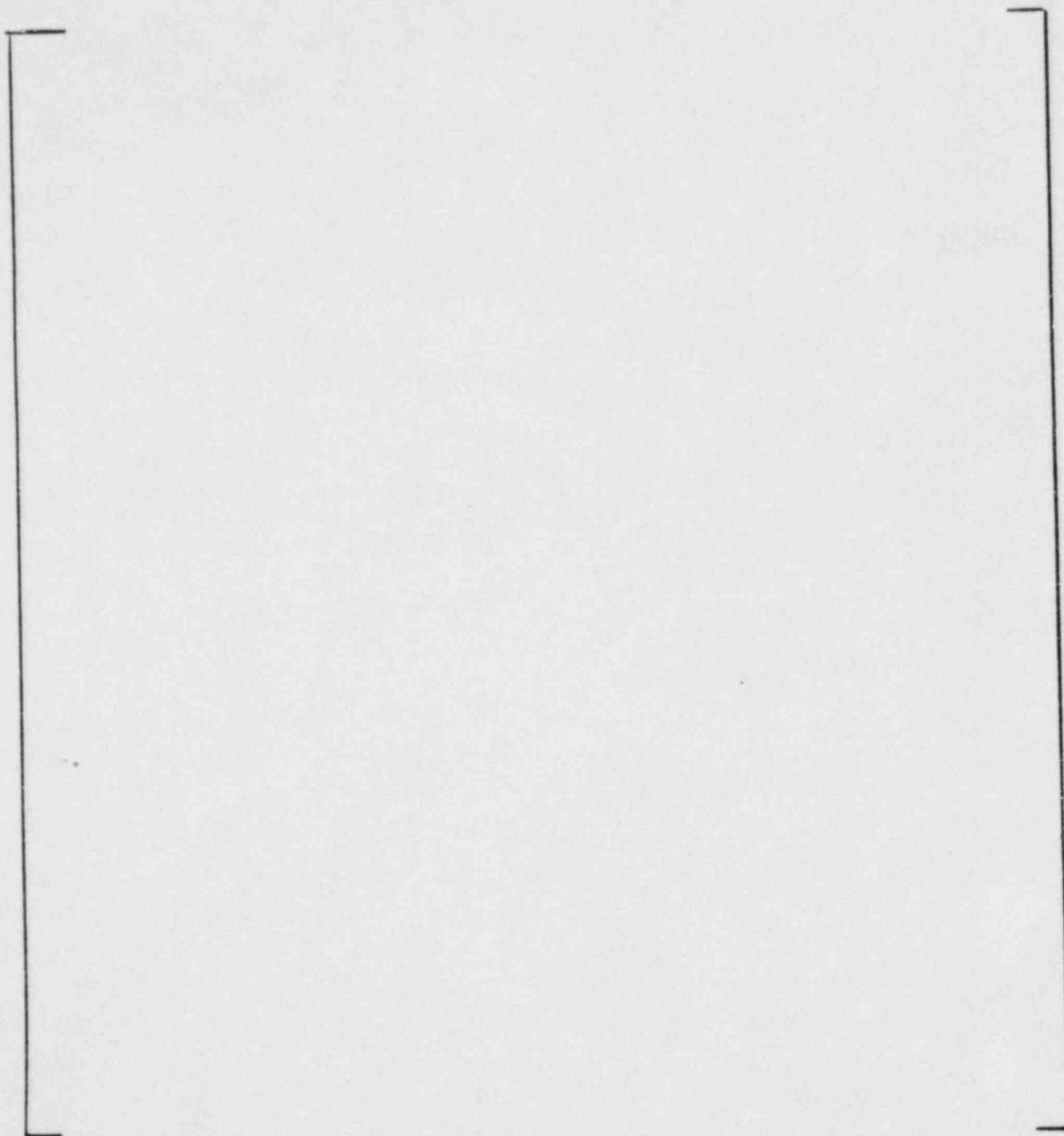


Table 2.1

Principal ROCS Depletion Chains

<u>Chain</u>	<u>Nuclide</u>	<u>Source Reactions*</u>	<u>Depletion Reactions*</u>
1.	U-235	none	A, B
2.	U-238	none	A, B
	[]		B
	[]		A, B
	[]		A, B
	[]		A, B
	[]		A, B
3.	MWD/T (exposure)	F	none
4.	I-135	Y	A, B
	XE-135	Y, B (I-135)	A, B
5.	PM-149	Y	B
	SM-149	B (PM-149)	A
6.	SHIMB (shim boron)	none	A
7.	[]		A
	[]		A
	[]		A
	[]		A

* A = neutron absorption
 C = neutron capture
 F = fission
 Y = fission product yield
 B = natural decay

TABLE 2.2

SUMMARY OF QUARTER CORE PIN/BCX COMPARISONS
 ROCS AND MC vs. PDQ

	Sample Size	Mean		Standard Deviation	
		(Abs.)	(Rel.)	(Abs.)	(Rel.)

The function of the DIT lattice code is to prepare few-group averaged cross sections for coarse-mesh and fine-mesh diffusion theory codes. These cross sections are used in ROCS (coarse-mesh), in PDQ (fine mesh) and in the MC module of ROCS (fine-mesh). Development of DIT began in 1972, and an early version was completed in 1974.^(3.1) The form currently in use was developed by early 1976.

The essential components of the DIT lattice code are:

1. Spectrum calculations using integral transport theory in up to 85 energy groups for typical portions of the assembly geometry (e.g.: fuel cell, fuel cell and burnable absorber, fuel cell and water-hole).
2. Few-group spatial calculations in exact assembly geometry followed by a leakage calculation to maintain a critical spectrum.
3. Isotopic depletion calculations for every cell in the assembly.

Thus the use of the two-dimensional integral transport theory code DIT ensures that the effects of lattice heterogeneities are explicitly treated. Few-group cross sections for coarse-mesh spatial calculations are obtained without laborious intermediate fine-mesh calculations to perform accurate weighting of the various types of fuel, absorber and water-hole cells.

Sections 3.1 through 3.4 discuss the structure of DIT, transport theory methods, basic cross section libraries and isotopic depletion respectively. Section 3.5 contains the verification of reactivity and reaction rate calculative accuracy using critical experiment measurements. Reference 3.2 contains a detailed verification of DIT relative to fuel pin power peaking measured in the critical

experiments which will not be repeated here. The following chapter contains the verification of DIT cross sections when used in the simulation of operating cores with the ROCS code. General accounts of the performance of DIT, including comparisons to critical experiments and operating reactor data, have also appeared in the open literature (References 3.3 through 3.6).

3.1 The Structure of DIT

The calculative strategy in DIT is illustrated by Figure 3-1. It follows closely that of the UKAEA code WIMS ^(3.7) which was constructed for use in LWR design in the late 1960s. DIT performs all the functions of more traditional methods based on sequential zero- or one-dimensional transport calculations. The complexities of the two-dimensional PWR fuel assembly geometry, including spectrum interactions of fuel, control rods, water-holes, burnable absorbers and in-core instrumentation flux detectors are represented. As shown by Figure 3-1, the essential feature of DIT, which distinguishes it from traditional methods, is that the spectral and spatial averaging procedures are based on calculations in two-dimensional geometry. Hence few approximations to the geometry representation are necessary. The use of integral transport theory ^(3.8) has made it feasible to retain explicit pin geometry in all calculative steps; i.e., homogenization of pin cells is not performed prior to the transport calculation in assembly geometry.

The so-called assembly calculation, which is performed in several broad energy groups (ranging from 2 to 12), is preceded by a sequence of spectrum calculations performed in the basic cross section library energy group structure of up to 85 groups. Basic cross section libraries are discussed in Section 3.3. The geometries used in the spectrum calculations are replicas of portions of the true assembly geometry as illustrated in Figure 3-1. Boundary conditions recycled from the assembly calculation are used for each spectrum geometry.

Group condensation based on the spectra calculated for all the different types of cells and subregions within them is performed to obtain few-group macroscopic cross sections that are passed on directly to the assembly calculations. Since the accuracy of the spectrum calculations is high, the group condensation can normally be performed with a standard four-group structure. In cases where conventional group condensation methods break down, more groups can be (and are) used in the assembly calculation.

The assembly calculation as well as the spectrum calculations are performed by integral transport theory (References 3.8 through 3.11) as described in Section 3.2.

This entire sequence of calculations is normally performed assuming that there is no net leakage from the assembly geometry. Following the assembly calculation, fine-group spectra are constructed for all subregions in the assembly based on the spatial distribution of the few-group assembly flux and on the energy and space distribution of the fine-group flux from the spectrum calculations. A correction for the influence of global leakage is then made on the basis of a B1 calculation with the fine energy group structure for the homogenized assembly.

Few-group microscopic cross sections for use in the depletion stage of DIT are formed using the basic cross section library and the spectra calculated as described. The depletion method is described in Section 3.4. Spatial averages of microscopic and macroscopic cross sections are performed for editing purposes and are passed on to ROCS, PDQ and MC.

The above calculations are performed in one single job step without manual intervention. Few-group cross sections are prepared in the HARMONY format (3.12) for ROCS and PDQ. Cross sections are input directly to MC without intermediate processing.

The neutron transport equation is solved in its integral form. Within each pin cell the methods for integrating the equation are those of Carlvik.^(3.10 and 3.11) Two optional FORTRAN routines have been written to implement Carlvik's methods and are used alternately as required by computational accuracy and efficiency. Use of the method described in Reference 3.10 permits the retention of an azimuthal flux dependence within each pin cell. Both routines permit the cells to remain heterogeneous. Conventional methodology would use these integration methods in the geometry of infinite lattices of equal cells or for single isolated cells with some input albedo on the boundary. Homogenization of each type of cell would follow from a sequence of such calculations. The homogenized cross sections would be used in an x-y geometry, coupling several cells either by integral transport theory, the S_n method or by diffusion theory. The method first described in References 3.8 and 3.9, and used in DIT, permits the cells of an arbitrary geometry to be coupled without the need for homogenization through the use of cell interface currents. As described in Reference 3.8, the neutron flux angular distribution may be approximated at the cell interfaces by the retention of a finite number of terms of a spherical harmonics expansion.

Details of the mathematical methods may be found in References 3.8 and 3.9. The general method will be summarized in this paragraph for the important case of isotropic scattering and azimuthally symmetric material distribution within each cell. The latter approximation precludes tracking the development of a tilted depletion distribution within an individual fuel or absorber pin. However this is seldom a requirement, and currently, there are no design computer codes with this capability. More important, the approximation implies a circular cylindrical cell boundary. Through the research of many, it is well established that the consequences of this approximation are negligible for volume ratios used in LWRs. As shown in Reference 3.8, these general approximations lead to the following equations for

the scalar flux, ϕ , and for the flux moments, ϕ_+ or ϕ_- , on the boundary, b, of each cell M:

$${}^M\phi_{0n}^0(r_i) = \sum_j {}^M T_{00,nn}^{00}(r_i, r_j) {}^M V_i {}^M \psi_{0n}^0(r_j) + \sum_{\nu} \sum_{\mu} {}^M T_{0\nu,nn}^{0\nu} {}^M S_b {}^M \phi_{\nu n}^{\mu} \quad (3.2-1)$$

$${}^M\phi_{\pm n}^{\pm} = \sum_j {}^M T_{n0,nn}^{\pm 0}(r_b, r_j) {}^M V_j {}^M \psi_{0n}^0(r_j) + \sum_{\nu} \sum_{\mu} {}^M T_{n\nu,nn}^{\pm \nu}(r_b, r_b) {}^M S_b {}^M \phi_{\nu n}^{\mu} \quad (3.2-2)$$

In these equations ψ represents the sum of scattering and fission sources through which coupling to other neutron energy groups occurs. Indices i and j are used to denote space points within cell M while n, m, μ and ν are indices for the spherical harmonics expansion. Provision has been made for retaining P_0 and P_1 moments of the cell boundary fluxes in DIT. At all space points within individual cells, an infinite number of terms in the angular expansions of neutron flux is implied by the use of integral transport theory. Indices k and κ represent the terms in a Fourier expansion for the flux as a function of azimuthal angle within each cell. Terms of order $k=0$ and $k=1$ are retained in DIT. Normally both orders are included since the accuracy in local flux would be insufficient with $k=0$ only. Figure 3-2 illustrates the dependence of the thermal flux on both radius and azimuthal angle within a fuel pin cell located next to a water-hole.

The general expressions for the transport matrices, in one-dimensional integral form, as permitted by the assumptions discussed above, are:

$$T_{n\nu, kx}^{m\mu}(r_i, r_j) = \frac{K_\nu^m}{\pi} \delta_{kx} \int_0^{2\pi} d\alpha e^{i(k\alpha + \mu\alpha' - m\alpha)} \frac{1}{t_{\nu\nu}} G_{n\nu,1}^{m\mu}(\tau_{\nu\nu}) \quad (3.2-3)$$

$$T_{n\nu, kx}^{m\mu}(r_i, r_b) = \frac{\bar{K}_\nu^m}{\pi} \delta_{kx} \int_0^{2\pi} d\alpha e^{i(k\alpha + \mu\alpha' - m\alpha)} \frac{\cos \alpha'}{t_{\nu s}} G_{n\nu,2}^{m\mu}(\tau_{\nu s}) \quad (3.2-4)$$

$$T_{n\nu, kx}^{m\mu}(r_b, r_i) = \frac{K_\nu^m}{\pi} \delta_{kx} \int_0^{2\pi} d\alpha e^{i(k\alpha + \mu\alpha' - m\alpha)} \frac{1}{t_{s\nu}} G_{n\nu,1}^{m\mu}(\tau_{s\nu}) \quad (3.2-5)$$

$$T_{n\nu, kx}^{m\mu}(r_b, r_b) = \frac{\bar{K}_\nu^m}{\pi} \delta_{kx} \int_0^{2\pi} d\alpha e^{i(k\alpha + \mu\alpha' - m\alpha)} \frac{\cos \alpha'}{t_{ss}} G_{n\nu,2}^{m\mu}(\tau_{ss}) \quad (3.2-6)$$

These integrals are evaluated by Carlvik's method. (3.10) Note that for isotropic scattering as indicated in Eq.(3.2-1), only the T_{00}^{00} matrix for coupling space points i and j within the cell is required. Higher orders are used only for the transport vectors describing escape from and transmission across each cell.

The functions $G(\tau)$ in equations (3.2-3 through -6) are related to the Bickley-Naylor functions. The details of these relationships may be found in Reference 3.10.

3.3 Basic Cross Sections

The DIT code utilizes data libraries containing up to 85-group microscopic cross sections, fission spectra, fission product yields and other supplemental data. The 85-group library contains more resonance region energy groups than other similar libraries in order to minimize uncertainties involved in group-averaged slowing-down cross sections, and is the reference library for this report. Fewer energy groups can (and will) be used for future design work. The source of data for the library is ENDF/B-IV. Three adjustments to the library data have been made to reflect changes to ENDF/B-IV recommended by the Cross Section Evaluation Working Group (CSEWG) for incorporation into ENDF/B-V. These adjustments include a reduction of about 3% in the shielded resonance integral of ^{238}U ; the use of the harder Watt fission spectra for ^{235}U and ^{239}Pu later incorporated in ENDF/B-V; and increases in the $\nu(\text{Nu})$ values of ^{235}U and ^{239}Pu . These adjustments lead to improved agreement with data from integral experiments and from operating power reactors.

The following sections describe the methods employed to construct the DIT data library.

3.3.1 Processing of Data

The data library contains cross sections and supplemental data for the 88 isotopes listed in Table 3.1. [

[

The energy group structure of the basic 85-group library is given in Table 3.2. A 41-group library has also been developed and may be

used as an alternative. Its preparation is described in Section 3.3.5.

The methods employed in the preparation of the library are outlined in Figure 3-3. Up-scattering is neglected above a cut-off energy of 1.855 eV.

3.3.2 Epithermal Region

The ENDF/B-IV files are processed with ETOG^(3.14) to provide cross sections, resonance parameters and scattering matrices (σ_s^0 and σ_s^1) for the isotopes contained in the library. ETOG prepares this data in 99 energy groups spanning the range from 14.9 MeV to 0.414 eV. The GAM portion of GGC3^(3.15) is used to condense the 99-group data into 50 energy groups spanning the energy range 14.9 MeV to 1.855 eV weighted with a spectrum representative of a PWR assembly.

In the resolved energy region (9.1keV to 1.855 eV), the capture and fission cross sections of resonant absorbers are replaced with resonance tables as described in Section 3.3.4.

3.3.3 Thermal Region

The ENDF/B-IV files are processed with FLANGE II^(3.16) to provide cross sections and full scattering matrices in the thermal region (1.855 eV to 0.00025 eV). The cross sections of isotopes containing resonances in the thermal region are Doppler broadened. For hydrogen, scattering matrices are prepared with FLANGE II using ENDF/B-IV thermal scattering law parameters for H₂O. The scattering law parameters are based on calculations with GASKET^(3.17) using the Haywood scattering model.

The cross sections and scattering matrices in the library are tabulated for a sufficient number of temperatures to span the range expected during power reactor operation and to permit linear interpolation.

3.3.4 Resonance Region

Cross sections for the resolved resonance region (9.1keV to 1.855 eV) are prepared with C-E RABBLE, an extension of the RABBLE^(3.18) code, using resolved resonance parameters from ENDF/B-IV. The cosine current approximation in RABBLE was replaced with an integral transport routine.^(3.11) Group-averaged resonance cross sections are generated with the modified RABBLE code which performs a space dependent calculation of the slowing down sources. The cross sections from the C-E RABBLE calculations are corrected to include the proper group dependent smooth contributions which are derived from the ETOG/GGC3 calculations. These cross sections are then converted into a two-dimensional table parametric in temperature and a background cross section via an equivalence theorem. DIT then uses the same equivalence theorem to interpolate between values in the table. This method eliminates the need to relate heterogeneous resonance integrals to homogeneous data.

3.3.5 Condensed Group Structure Library

A 41-group data library, derived from a condensation of the basic 85 group library, may be used as an alternative. The group structure is given in Table 3.3. The number of groups in the resolved resonance region is kept the same as the 85-group library to avoid condensation approximations. The condensation is performed as:

$$\sigma_{X,G}^i = \int_{g \in G} \sigma_{X,g}^i \phi_g / \int_{g \in G} \phi_g \quad (3.3-1)$$

where X is the reaction (absorption or fission) and g is the number of fine groups within condensed group G.

For the scattering matrices, the condensation is

$$\sigma_{S_{G,G'}}^i = \frac{\int_{g \in G} \int_{g' \in G'} \sigma_{S_{g,g'}}^i \phi_g}{\int_{g \in G} \phi_g} \quad (3.3-2)$$

and for the diagonal elements (3.13)

$$\sigma_{S_G}^i = \int_{g \in G} \sigma_{S_g}^i \cdot T_g \cdot \phi_g / \int_{g \in G} \phi_g$$

$$T_g = 2 \left(\frac{\Sigma_{S_G}}{\Sigma_{S_g}} \right)^2 - \frac{\Sigma_{S_G}}{\Sigma_{S_g}} \quad (3.3-3)$$

and

$$\sigma_{S_{G,G}}^i = \sigma_{S_G}^i - \int_{G' \neq G} \sigma_{S_{G,G'}}^i$$

where σ_s represents either the P_0 or P_1 component.

The cross sections for each isotope are weighted with a flux spectrum representative of the local environment the isotope would typically experience in a fuel cell, e.g., fuel region, clad region or coolant.

The 41-group library has been tested against the basic 85-group library and has been shown to accurately reproduce reactivity levels, reactivity coefficients, power distributions and reaction rates.

Depletion Calculations

This section describes the methods employed to predict the changes in isotopic composition of reactor core components during power operation. The basic method is described in detail in Reference 3.19.

3.4.1 Burnup Chains

The three core components which deplete are the fuel, the burnable absorber rods and the in-core instruments. Burnup chains for each have been incorporated in the data library for DIT. The fuel chains describe the transformation of the important actinides, (See Fig. 3.4) and the buildup and destruction of the fission products (See Fig. 3.5). The burnable absorber rods contain either gadolinia (Figure 3.6) or boron. The boron chain is a simple depletion of ^{10}B . The C-E fixed in-core instrument is a Rhodium Self Powered Detector (SPND). The chain is a simple depletion of ^{103}Rh .

3.4.2 Burnup Equations

The burnup equations are derived from the formulation of a material balance on each of the isotopes in the chain:

$$\frac{dN_i}{dt} = \text{PRODUCTION}_i - \text{LOSS}_i \quad (3.4-1)$$

where N_i is the atom density of isotope i .

The burnup equations are solved for each region in each cell specified to contain a depletable isotope. The depletion time steps are chosen such that the flux in the region and the cross sections can be considered constant during a step. Spectrum and spatial calculations are performed at the start of each depletion step to update the fluxes and cross sections.

The depletion chains are set in the form of a lower triangular matrix; that is, self-contained loops are not permitted in the chains. The formulation of the fuel chains will be described. Depletion in burnable absorbers and instrument material is treated in a similar manner.

The fuel depletion chains are resolved into a number of independent actinide and fission product (FP) burnup chains. This is done to minimize computation time by reducing the size of the individual matrices.

The depletion time step, ΔT , is divided into a number of smaller steps

$$\delta T = \Delta T / N \quad (3.4-2)$$

where N is chosen to ensure that reaction rates remain essentially constant during the interval.

The actinide chains and the fission product chains are decoupled during each interval. For the actinides the burnup equation for each isotope is

$$\frac{dN_i}{dt} = d_{ii} N_i(t) + \sum_{j=1}^{i-1} d_{ij} N_j(t) \quad (3.4-3)$$

where

$i = 1, 2, \dots, \text{NFUEL}$ isotopes, and

j is an index on the isotope contributing as a source to i .

The d_{ii} are the diagonal elements for the loss terms:

$$d_{ii} = -(\lambda_i + \sum_{g=1}^{NG} \bar{\phi}_g \sigma_i^g) \quad (3.4-4)$$

and the d_{ij} are the off-diagonal elements for the source terms:

$$d_{ij} = \left(\lambda_{j \rightarrow i} + \sum_{g=1}^{NG} \bar{\phi}_g \sigma_{j \rightarrow i}^g \right) \quad (3.4-5)$$

Also,

$\lambda_{j \rightarrow i}$ = decay constant of isotope j to isotope i ;

$\sigma_{j \rightarrow i}^g$ = reaction cross section to produce i from j in group g

$\bar{\phi}_g$ = average flux in group g ;

NG = number of neutron energy groups.

The actinide chains are solved first. Then, a constant average source rate \bar{Q}_k for each of the N_{FP} fission product nuclides is calculated:

$$\bar{Q}_k = \sum_{i=1}^{N_{FUEL}} x_{k,i} \bar{N}_i \sum_{g=1}^{NG} \sigma_{f,i}^g \bar{\phi}_g \quad (3.4-6)$$

where

$\sigma_{f,i}^g$ = fission cross section in group g for isotope i .

$x_{k,i}$ = yield of FP_k from fissionable isotope, i .

$$\bar{N}_i = \frac{1}{\delta T} \int_T^{T+\delta T} N_i(t) dt \quad (3.4-7)$$

and $K = N_{FUEL} + 1, \dots, N_{FUEL} + N_{FP}$

The fission product burnup equations are in the non-homogeneous form:

$$\frac{dN_k}{dt} = d_{k,k} N_k(t) + \sum_{l=N_B+1}^{k-1} d_{k,l} N_l(t) + \bar{Q}_k \quad (3.4-8)$$

where the index on l includes the isotopes of the independent fission product chain.

The burnup equations are solved either analytically or numerically based on the following criterion:

$$e^{-\alpha} - \frac{2-\alpha}{2+\alpha} = \epsilon_B \quad (3.4-9)$$

where ϵ_B is a difference value on the order of 10^{-5} to 10^{-6} and α is related to the d_{ii} values.

A critical value of α_e for the criterion ϵ_B is found, such that, for

$$|d_{ii}| \delta T > \alpha_e$$

an analytical solution is used,
and for

$$|d_{ii}| \delta T \leq \alpha_e$$

a numerical solution is used.

The solutions of these equations are described in Reference 3.19.

3.5 Verification Against Critical Experiments

3.5.1. The Use of Clean Critical Experiments for Methods and Data Verification

The analyses of clean critical experiments provide a means of evaluating the calculative models and the basic cross section data which constitute the design methodology. Selected critical experiments containing either uniform arrays of fuel rods or heterogeneous arrangements which simulate PWR assembly designs have been analyzed with the DIT code and its data library as a basis. Selection of criticals was based on the criteria of applicability to PWR fuel and assembly designs, self-consistency of measured parameters, and availability of adequate data to model the experiments.

The uniform criticals have been analyzed to demonstrate the adequacy of the fine details of the calculative modeling and the data processing through comparisons with measured criticality parameters and reaction rate ratios.

The non-uniform criticals provide the means of further verifying the design methodology for core configurations which simulate specific PWR assembly designs. In addition to criticality parameters, comparison between calculated and measured fission rate distributions establishes calculative biases and uncertainties for local power distribution predictions.

3.5.2 Uniform Criticals

Reaction rate ratios are defined below and are referred to in the descriptions of the individual experiments.

$$C = (\text{Capture Rate U238})/(\text{Fission Rate U235})$$

$$\rho^{28} = \frac{\text{Epithermal Capture Rate U238}}{\text{Thermal Capture Rate U238}}$$

$$\delta^{28} = \frac{\text{Fission Rate U238}}{\text{Fission Rate U235}}$$

$$\delta^{25} = \frac{\text{Epithermal Fission Rate U235}}{\text{Thermal Fission Rate U235}}$$

$$\text{RCR} = \frac{(\text{Capture Rate U238/Fission Rate U235}) \text{ Experiment}}{(\text{Capture Rate U238/Fission Rate U235}) \text{ Thermal Column}}$$

Description of Experiments

Table 3.4 contains pertinent core parameters for each of the experimental configurations. The moderator-to-fuel volume ratios were varied by changing the cell pitch of the fuel rod arrangement. In all cores, H₂O was the moderator and reflector material.

(a) UKAEA, Winfrith R/100H Series (3.20)

The cores were composed of stainless steel clad UO₂ (3 w/o ²³⁵U) fuel rods arranged on a square pitch. The fuel pellet diameter was 1.012 cm and the outer diameter of the clad was 1.0925 cm. Measured parameters included criticality, asymptotic core buckling (B²), the Relative Conversion Ratio (RCR) and ρ^{28} .

(b) TRX 1 and 2 (3.21)

The TRX 1 and 2 cores were composed of aluminum clad, uranium metal (1.31 w/o ²³⁵U) fuel rods arranged on a triangular pitch. The fuel pellet diameter was 0.983 cm and the outer diameter of the clad was 1.1506 cm. Measured parameters

included criticality, B^2 , ρ^{28} , δ^{28} , δ^{25} and the conversion ratio, C.

(c) EPRI-BNWL Critical Experiments (3.22)

The cores were composed of aluminum clad, vibrationally compacted UO_2 (2.35 w/o) fuel rods arranged on a square pitch. The fuel outer diameter was 1.118 cm and the clad outer diameter was 1.27 cm. For each moderator-to-fuel volume ratio, unborated and borated critical configurations were established. The critical parameters and an asymptotic core buckling (B^2) were measured for selected fuel rods.

(d) BAPL UO_2 Experiments (3.21)

The cores were composed of aluminum clad, UO_2 (1.31 w/o ^{235}U) fuel rods arranged on a triangular pitch. The fuel pellet diameter was 0.973 cm and the clad outer diameter was 1.0925. Measured parameters included criticality, B^2 , ρ^{28} , δ^{28} and δ^{25} .

The BAPL UO_2 cores 1, 2 and 3 are specified as integral benchmarks for data testing by CSEWG.

Method of Analysis

An infinite lattice fuel cell was modeled in the DIT code with each region (e.g., fuel, clad and moderator) represented explicitly. Fuel-clad gaps were homogenized with the clad material by volume weighting. The square or triangular cells were treated as equivalent right circular cylinders. The integral transport calculation in DIT was solved in 85 energy groups for the heterogeneous cell. A B-1 calculation was performed in 85 energy groups for the homogenized cell (by flux-volume weighting of cross sections) using the measured bucklings. The B-1 calculation provided the effective multiplication of the cell and leakage corrected fluxes to obtain reaction rate ratios to compare to the measured values.

The DIT design data library was used for the analysis. As discussed in Section 3.3, the library is based on ENDF/B-IV with modifications. These include:

1. A reduction of about [] in the shielded ^{238}U resonance integral.
2. The use of watt spectra for ^{235}U and ^{239}Pu .
3. Increases of about [] in the ν values of ^{235}U and ^{239}Pu .

Item 1 was included to remove a known overprediction of ^{238}U capture using ENDF/B-IV resonance data. Items 2 and 3 are related to changes made in ENDF/B-V. Not included were changes to [] [] These parameters would increase M^2 which appears to be underpredicted by 2 to 3% with ENDF/B-IV data. The underprediction of M^2 is most apparent in the results for the high leakage, uniform critical experiments. It is not significant in power reactors where the leakage worth is much less.

Analysis of Results

The uniform critical experiments analyzed included:

1. Moderator-to-fuel ratios ranging from 0.78 to 4.02
2. Fuel enrichment ranging from 1.3 w/o to 3.0 w/o ^{235}U
3. Various fuel pellet diameters including vibrationally compacted fuel
4. Aluminum and stainless steel cladding
5. Unborated and borated cores
6. One experiment at an elevated temperature
7. UO_2 and uranium metal fuel

Overall, for moderator-to-fuel ratios typical of PWR designs (1.6 to 2.0), the agreement in calculated reactivity is good and differences are well understood.

The calculated δ^{28} are generally lower than measurements by an average value of about 3.3%. This value is comparable to the uncertainty in the measurements. Since ^{238}U has a threshold fission energy, the δ^{28} value will be sensitive to the accuracy in the calculation of the high energy spectrum. Changes to the fission and inelastic scattering cross sections of ^{238}U have been recommended for ENDF/B-V and will result in slightly better agreement. With the changes recommended for ENDF/B-V, a difference of about 2% would remain.

The calculated δ^{25} values are generally larger than the measured values by an average of about 2.2%. This difference appears to be related to a small overprediction in the resonance fission in ^{235}U . This can be attributed to the method of generating resonance

cross sections or for accounting for interference effects. An overprediction of the resonance fission in ^{235}U and, consequently, the total fission would also contribute to the underprediction of the δ^{28} values.

The observed differences in the δ^{28} and δ^{25} values are small and are not significant in the design application of the code.

Conclusions

The results of the analyses of the 15 uniform critical experiments demonstrate that the DIT code and its data library accurately model the physical processes important for PWR design. The level of agreement with measured criticality and reaction rate ratios is on the order of the uncertainties in these parameters. The small differences that are observed are understood and are not considered significant in the design process.

3.5.3. Non-Uniform Criticals

The core arrangements of the non-uniform critical experiments selected for analysis are representative of C-E assembly designs. Measurements included criticality plus fission rate distributions for selected fuel rods. This section addresses the comparisons between measured and calculated criticality. Comparisons between the measured and calculated fission rate distributions to establish calculative biases and uncertainties in predicting intra-assembly power peaking are fully covered in Reference 3.3.

Description of the Experiments

a) Combustion Engineering Sponsored Critical Experiments (C-E Criticals)

A series of critical experiments was performed for Combustion Engineering at the Westinghouse Reactor Evaluation Center (WREC) employing the CRX reactor. The experimental program consisted

of approximately [] critical configurations of fuel rods. The basic core configuration was a 30X30 square fuel rod array of Zr-4 clad UO_2 fuel having an enrichment of [] Fuel rods were removed to create internal water holes or channels to accommodate control rods or to simulate control rod channels representative of C-E assembly designs (primarily the MARK V 14X14 design).

The majority of the experiments employed a lattice pitch of [] with several experiments repeated with a lattice pitch of [] These values of [] together with the fuel pellet dimensions, enrichment and rod diameter, resulted in hydrogen to fuel ratios representative of the C-E design at room and at operating temperatures, respectively.

The fuel rod assemblies were fully reflected with H_2O on the four sides. The experiments were conducted at room temperature. Both borated and unborated cores were employed. A given configuration was made critical by adjusting the water height. The reactivity worths of incremental water height changes were made to provide a means of interpolating to exact criticality. Axial bucklings were obtained by fitting measured activities along a rod to a cosine function.

Representative core lattices were selected for analysis. Pertinent data for these lattices are summarized in Table 3.5. The two basic lattice layouts are shown in Figures 3-8 and 9.

b) KRITZ Experiments

A program of critical experiments, sponsored jointly by Combustion Engineering and KWU, was performed at the KRITZ Critical Facility OF AB Atomenergi, Studsvik, Sweden. The program consisted of analyzing a number of core configurations of interest to C-E and KWU. The C-E configurations were

representative of the MARK V 14X14 fuel assembly, including the 5 large control rod channels. A basic cell pitch of [] was used for all lattices.

A description of the fuel rods is given in Table 3.6. The cores were relatively large both in cross sectional area and height. Each core contained about [] rods [] in length. The core was reflected with water on the four sides and the bottom. Soluble boron was employed for gross reactivity control.

Core criticality was obtained by adjusting the water height. The water temperature was raised by passing the moderator through a 500 kw electric heater outside the core and circulating the water until the desired equilibrium temperature was reached. Once the experiment was started, the water was not circulated. Temperature measurements were made at 3 axial positions to insure equilibrium conditions were reached. In the higher temperature experiments, some cooldown occurred during the experiment. Its effect on reactivity was accounted for by adjusting the reported soluble boron concentration.

The axial buckling was determined by fitting data from axial gamma scans of the irradiated core to a cosine function. Copper wire activation measurements were also employed to determine axial bucklings.

The core layout for the experiment is shown in Figure 3-10.

Method of Analysis

[]

Four group, fine-mesh, cross sections were generated with DIT.

Separate DIT calculations modeled the various regions of the cores; for example, the central 14x14 region and the asymptotic region in the cores corresponding to Figure 3.8 were treated with two DIT calculations. In this way, spatial and spectrum effects due to heterogeneities were properly accounted for in the cross sections. The cross sections for the CEA channels (large water-holes) were fitted such that the diffusion calculation reproduced the reaction rates predicted by transport theory, i.e. DIT. [

[

[

Analysis of Results

The results of the analyses of the [] critical experiments are summarized in Table 3.7. The average k_{eff} is 1.0016. The results for the C-E Criticals indicate that CEA water worth is slightly overpredicted by DIT. This is seen by comparing the k_{eff} 's for the lattices #12 and #32 seen in Figures 3-8 and 3-9. As discussed in Section 3.5.2, the leakage is expected to be slightly underpredicted with the worths varying from 0.1 to 0.2% k_{eff} . Corrections for these effects would tend to be compensating.

Conclusions

The analyses of [] non-uniform critical experiments with configurations representative of the C-E assembly design demonstrate that the reactivity levels calculated with design methods and data lead to good agreement with experiment. The cores selected for analysis provide an adequate combination of parameters to test calculative methods and data. These include three moderator-to-fuel volume ratios and UO_2 representative of beginning of life (BOL).

3.6 References

- 3.1 A. Jonsson, "Methods and Program Description - NUTEST 2.0" CENPD-159, November 1974.
- 3.2 A. Jonsson, W. B. Terney, M. W. Crump, "Evaluation of Uncertainty in the Nuclear Power Peaking Measured by the Self-Powered Fixed In-core Detector System", CENPD-153-P, Rev. 1-P, May 1980.
- 3.3 A. Jonsson, J. R. Rec, U. N. Singh, "Verification of a Fuel Assembly Spectrum Code Based on Integral Transport Theory", Combustion Engineering Report TIS-5815 and Trans. Am. Nucl. Soc., 28, 778 (1978).
- 3.4 A. Jonsson, J. R. Rec and U. N. Singh, "Requirements for the Physics Analysis of PWR Fuel Assemblies," in Symposium Proceedings: Nuclear Data Problems for Thermal Reactor Applications, EPRI NP-1098, June 1979, p. 17-1.
- 3.5 A. Jonsson, P. H. Gavin, J.R. Rec and W. B. Terney, "Core Physics Validation for the Combustion Engineering PWR," Combustion Engineering Report TIS-6368 and Trans. Am. Nucl. Soc., 33, 810 (1979).
- 3.6 R. L. Hellens and A. Jonsson, "Recent Improvements in PWR Physics," ANS topical meeting: 1980 Advances in Reactor Physics and Shielding, Sun Valley, Idaho, September 1980.
- 3.7 J. R. Askew, F. J. Fayers and P. B. Kemshell, "A General Description of the Lattice Code WIMS," J. Brit. Nuclear Energy Society, 5, 564 (1966).
- 3.8 A. Jonsson and A. J. Mockel, "Discrete Integral Transport Theory Extended to the Case with Surface Sources," Atomkernenergie, 24, 79-84, (1974).

- 3.9 A. Jonsson and A. J. Mockel, "Integral Transport Theory with Cell Couplings Involving Arbitrarily Distributed Currents," Trans. Am. Nucl. Soc., 21, 231 (1975).
- 3.10 I. Carlvik, "Integral Transport Theory in One-Dimensional Geometries," Nukleonik, 10, 104 (1967).
- 3.11 I. Carlvik, "A Method for Calculating Collision Probabilities in General Cylindrical Geometry and Applications to Flux Distributions and Dancoff Factors," in U.N. Int. Conf. on the Peaceful Uses of Atomic Energy, Geneva 1964, Vol. 2 p. 225-231 (1965).
- 3.12 R. J. Breen, O. J. Marlowe, C. J. Pfeifer, "HARMONY: System For Nuclear Reactor Depletion Computation," WAPD-TM-478, January 1965.
- 3.13 A. Travelli, "A New Definition of the Microscopic Multigroup Transport Cross Sections", Trans. Am. Nucl. Soc., 11, 532 (1968).
- 3.14 D. E. Kusner, et al, "ETOG-1, a Fortran IV Program to Process Data from ENDF/B Files to the MUFT, GAM, and ANISN Formats," WCAP-3845-1, ENDF-114(1969).
- 3.15 J. Adir, K. D. Lathrop, "Theory of Methods Used in the GGC-3 Multigroup Cross Section Code," GA-7156 (1967).
- 3.16 H. C. Honeck and D. R. Finch, "FLANGE-II, A Code to Process Thermal Neutron Data from an ENDF/B Tape," DP-1278, ENDF-152 (1971).
- 3.17 J. U. Koppel, J. R. Triplett, and Y. D. Naliboff, "GASKET, A Unified Code for Thermal Neutron Scattering, General Atomic Report GA-7417 (1966).
- 3.18 P. Kier and A. Robba, "RABBLE, A Program for Computation of Resonance Absorption in Multi-Region Reactor Cells," ANO-7326 (1967).

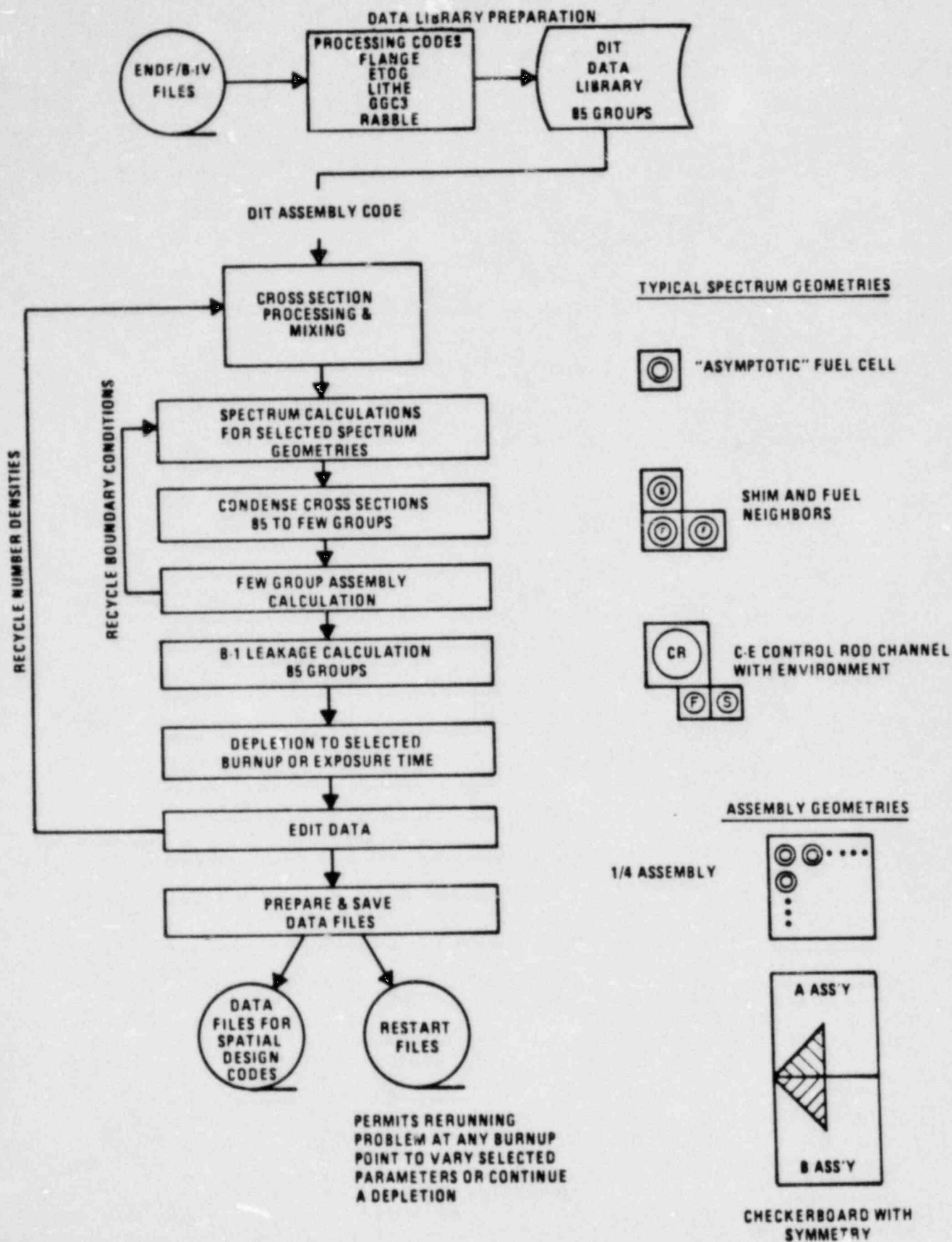
3.19 F. Bennewitz, A. Muller, M. Wagner, "Development of a Burn-Up (Depletion) Program for Calculation of the 3-D Burn-Up Dependent Power Density Distribution in Light Water Reactors," NUREG/TR-0029,R4.

3.20 P. B. Kemshell, "Some Integral Properties of Nuclear Data Deduced from WIMS Analyses of well Thermalized Uranium Lattices," AEEW-R786 (1972).

3.21 "Cross Section Evaluation Working Group Benchmark Specifications", ENDF-202 (BNL-19302).

3.22 R. Smith and G. Konzeh, "Clean Critical Experiment Benchmarks for Plutonium Recycle in LWR's," EPRI-NP-106, Vol. I (1976).

FIGURE 3-1
THE DIT ASSEMBLY CODE



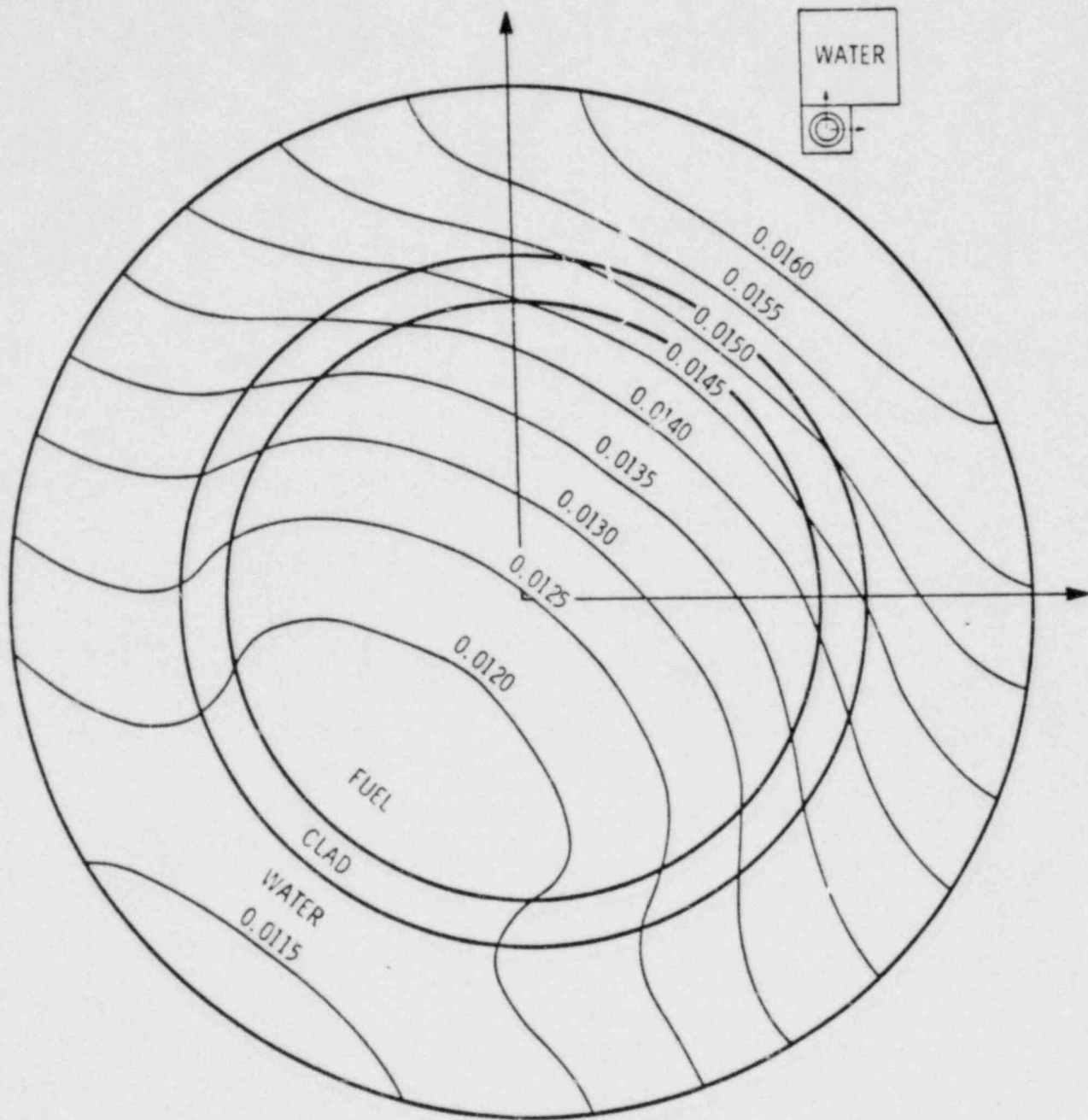


Figure 3-2
 THERMAL FLUX CONTOURS IN A UO_2 PIN
 NEAR A WATERHOLE

FIGURE 3-3

PREPARATION OF THE DATA LIBRARY FOR THE DIT CODE

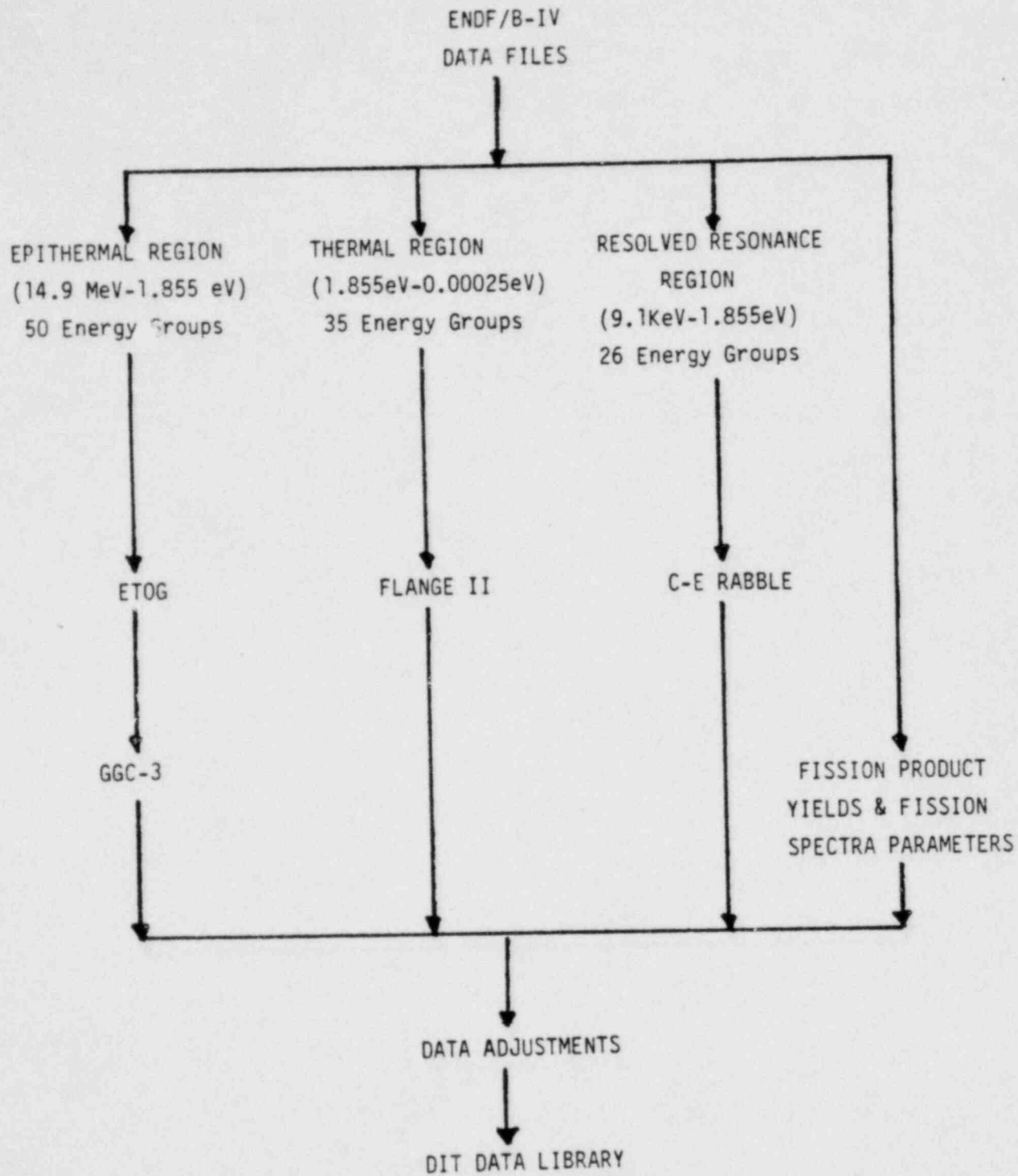
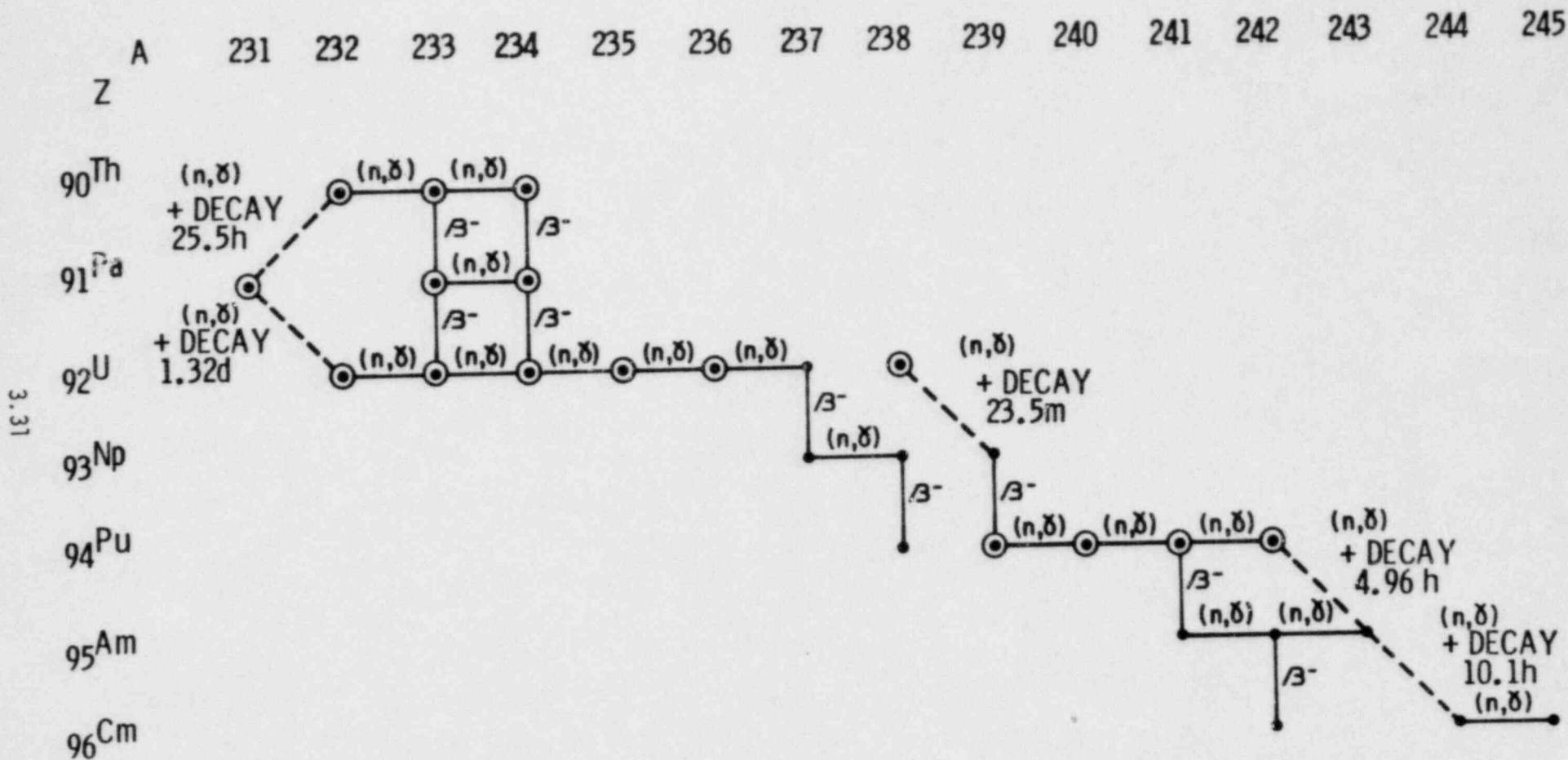


Figure 3-4
 FUEL BURNUP CHAINS



⊙ CONTRIBUTES TO FISSION PRODUCT INVENTORY

Figure 3-5
FISSION PRODUCT CHAINS

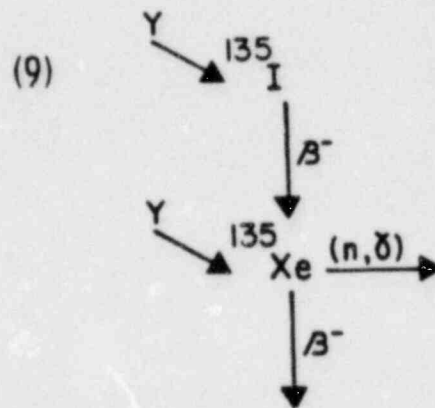
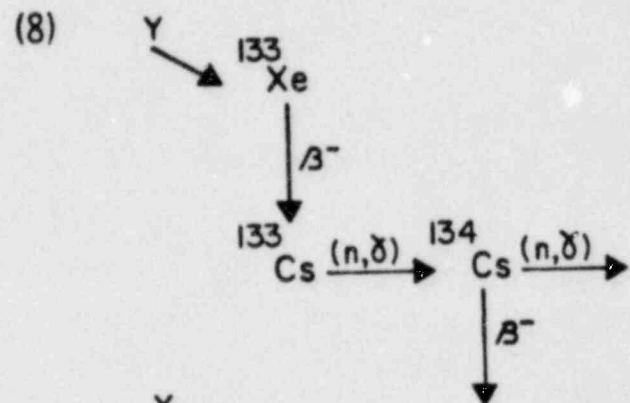
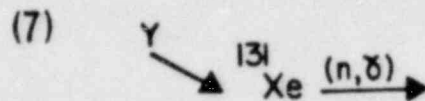
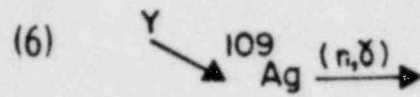
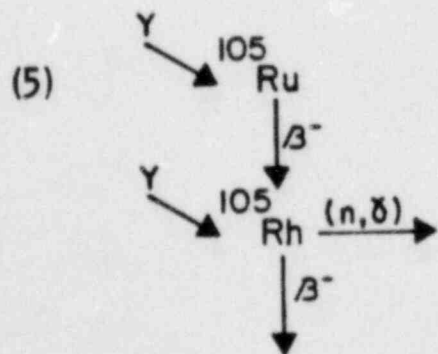
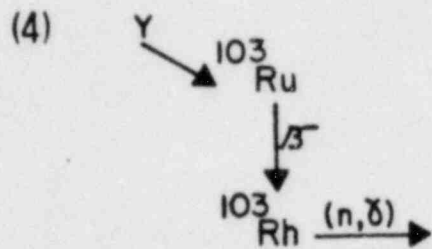
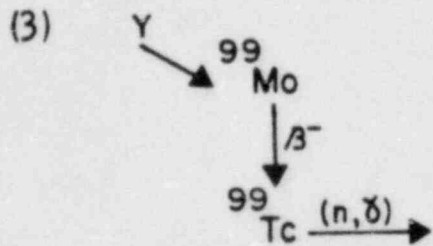
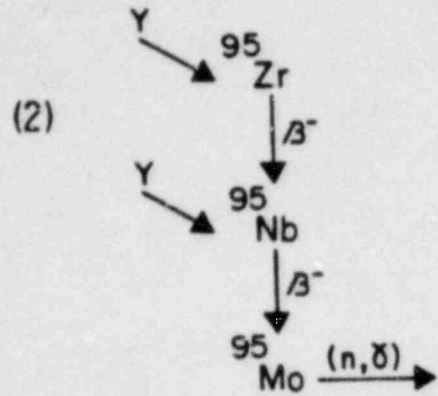
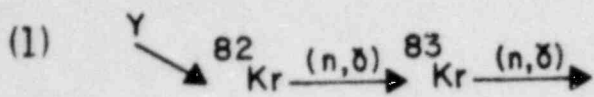


Figure 3-5 CONTINUED
FISSION PRODUCT CHAINS

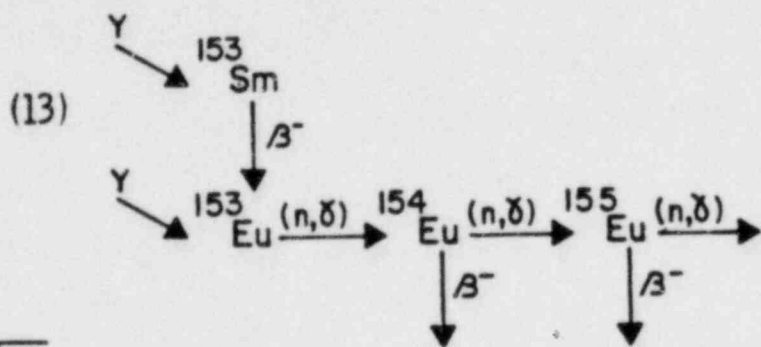
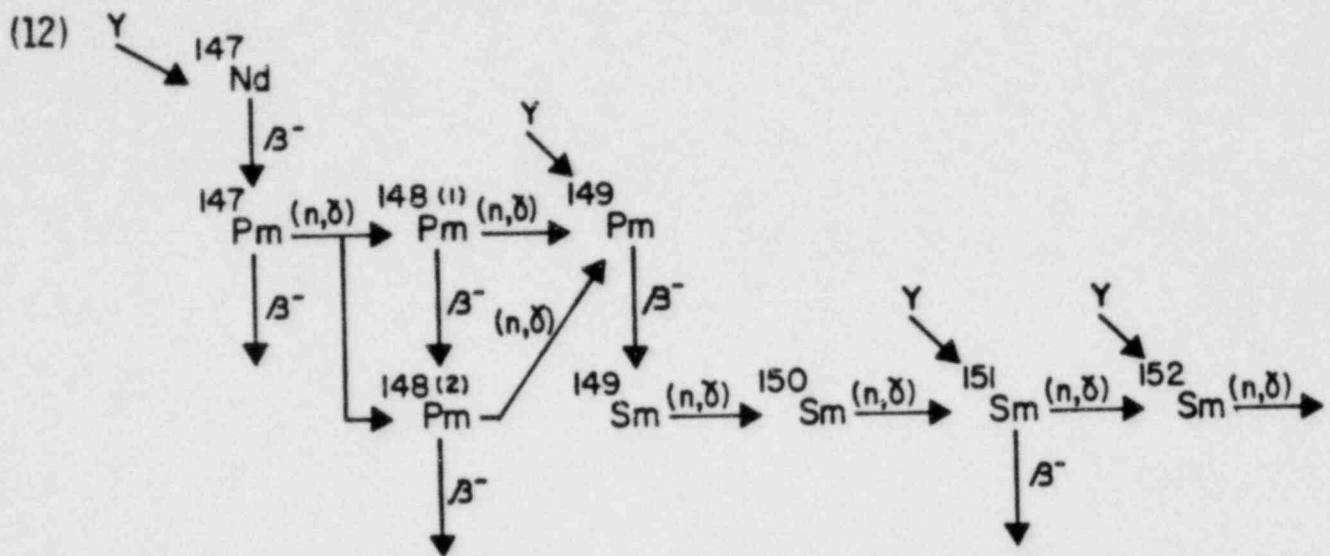


Figure 3-6
GADOLINIUM DEPLETION CHAIN

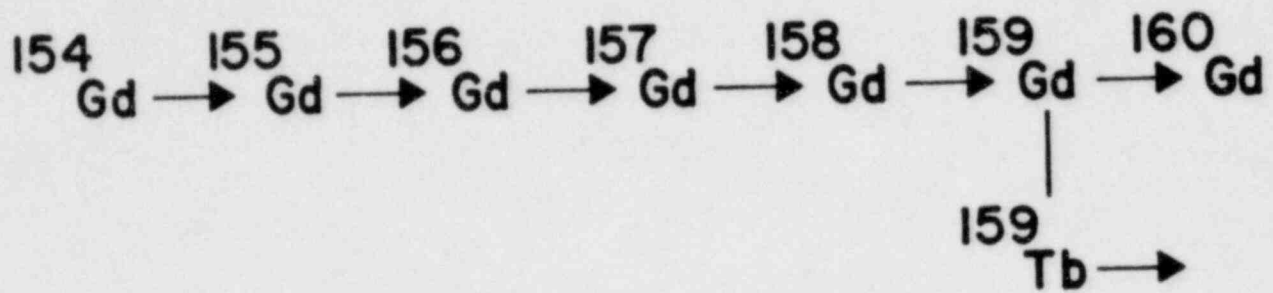


FIGURE 3-7

CRITICALITY OF UNIFORM LATTICES

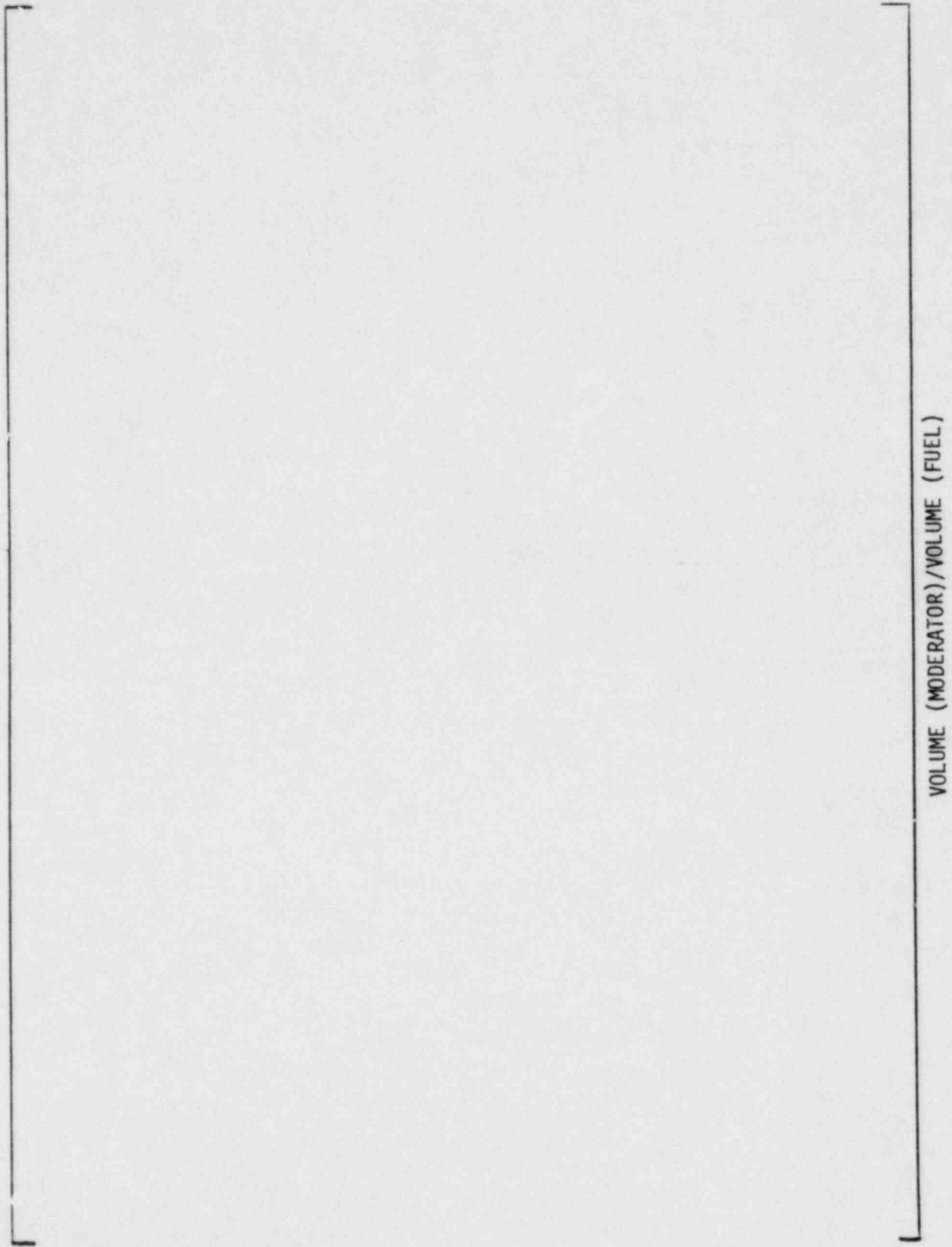
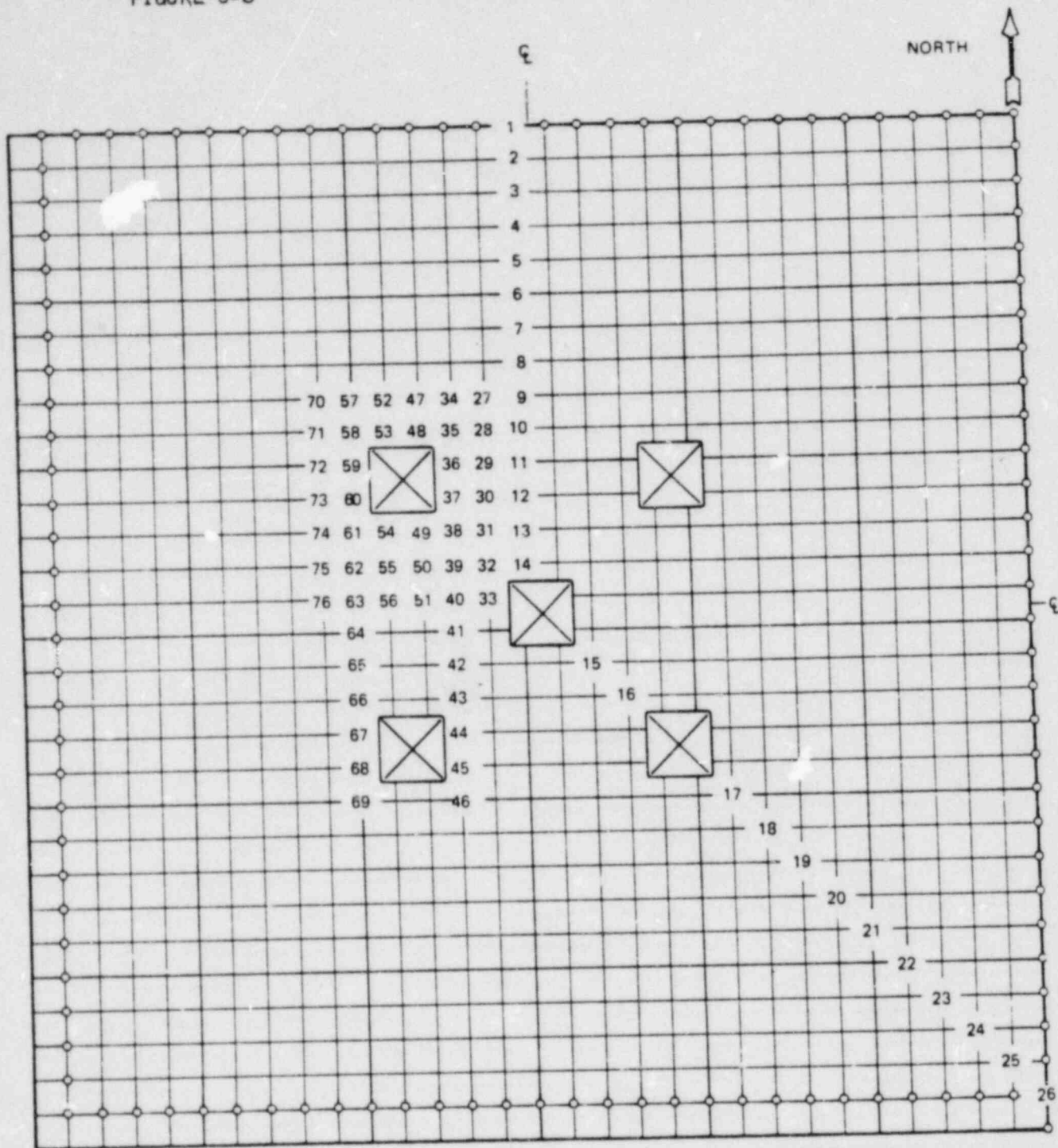
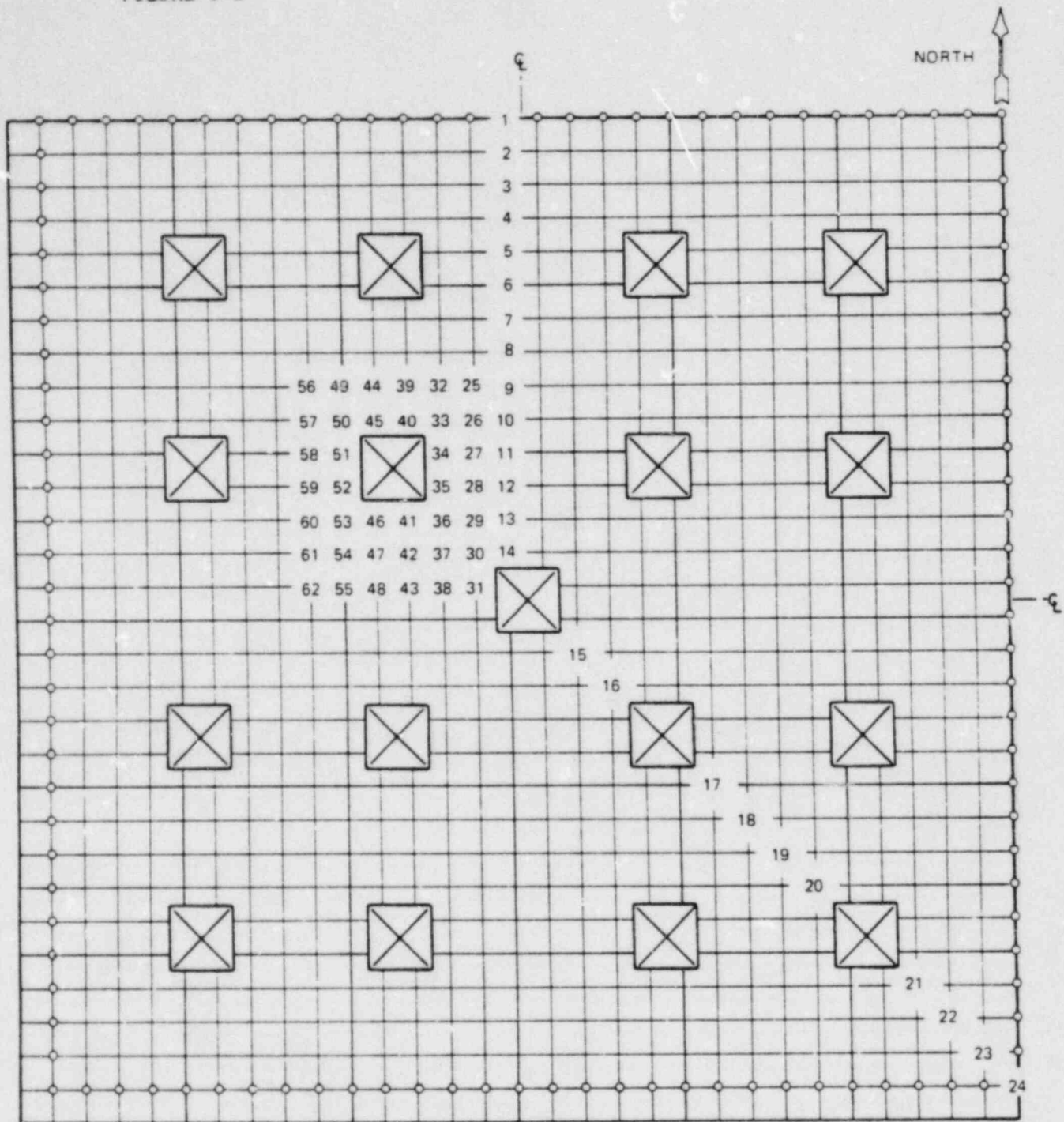


FIGURE 3-8



C-E Criticality Experiments
Lattices # 12,43

FIGURE 3-9



C-E Criticality Experiments
Lattices # 32,53,56

□ UO₂ - ROD

■ ROD FOR FISSION RATE
MEASUREMENT

□ WATER HOLE

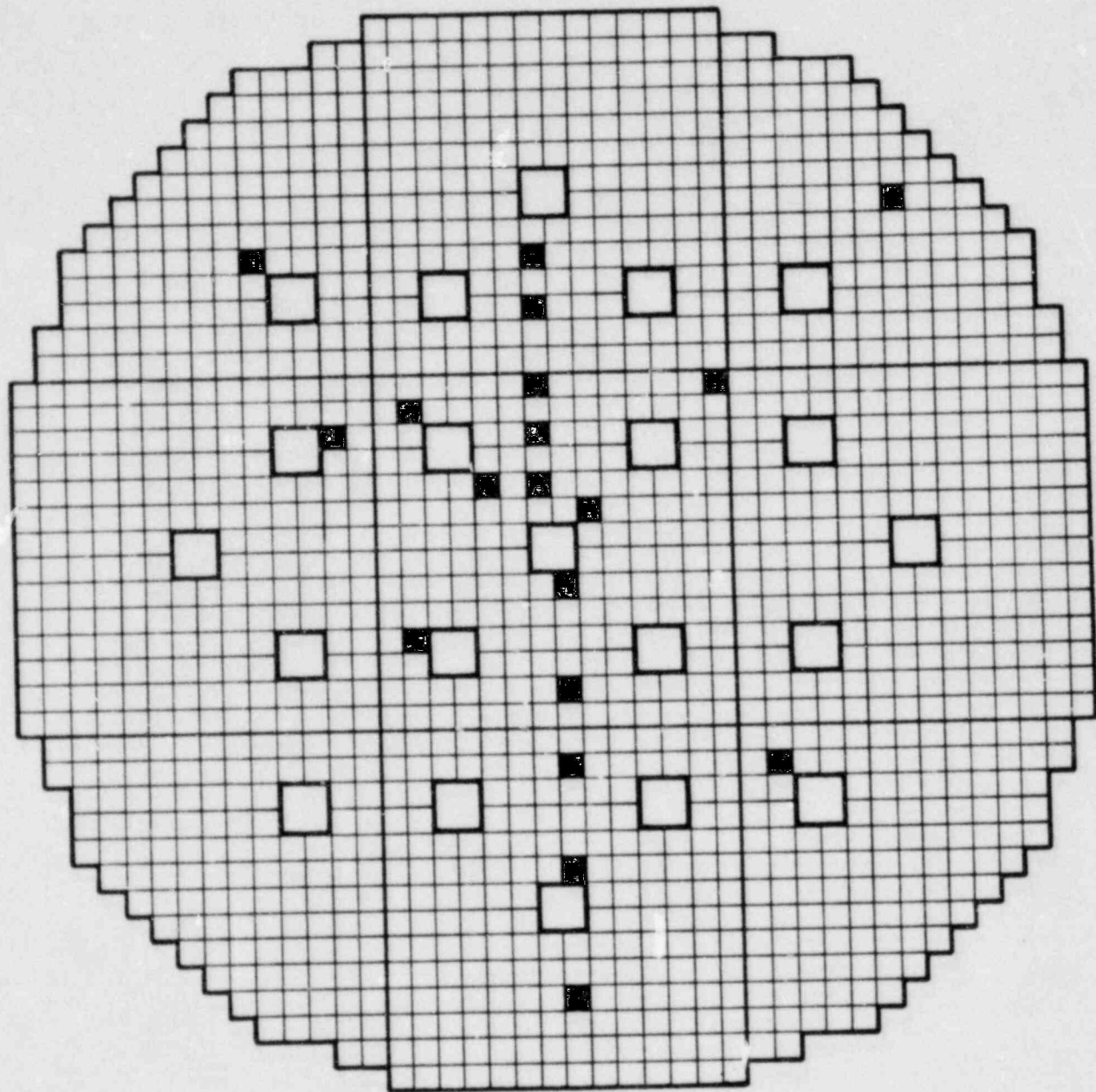


Figure 3-10
KRITZ U-WH2 CORE LAYOUT

TABLE 3.1

Isotopes on DIT Data Library

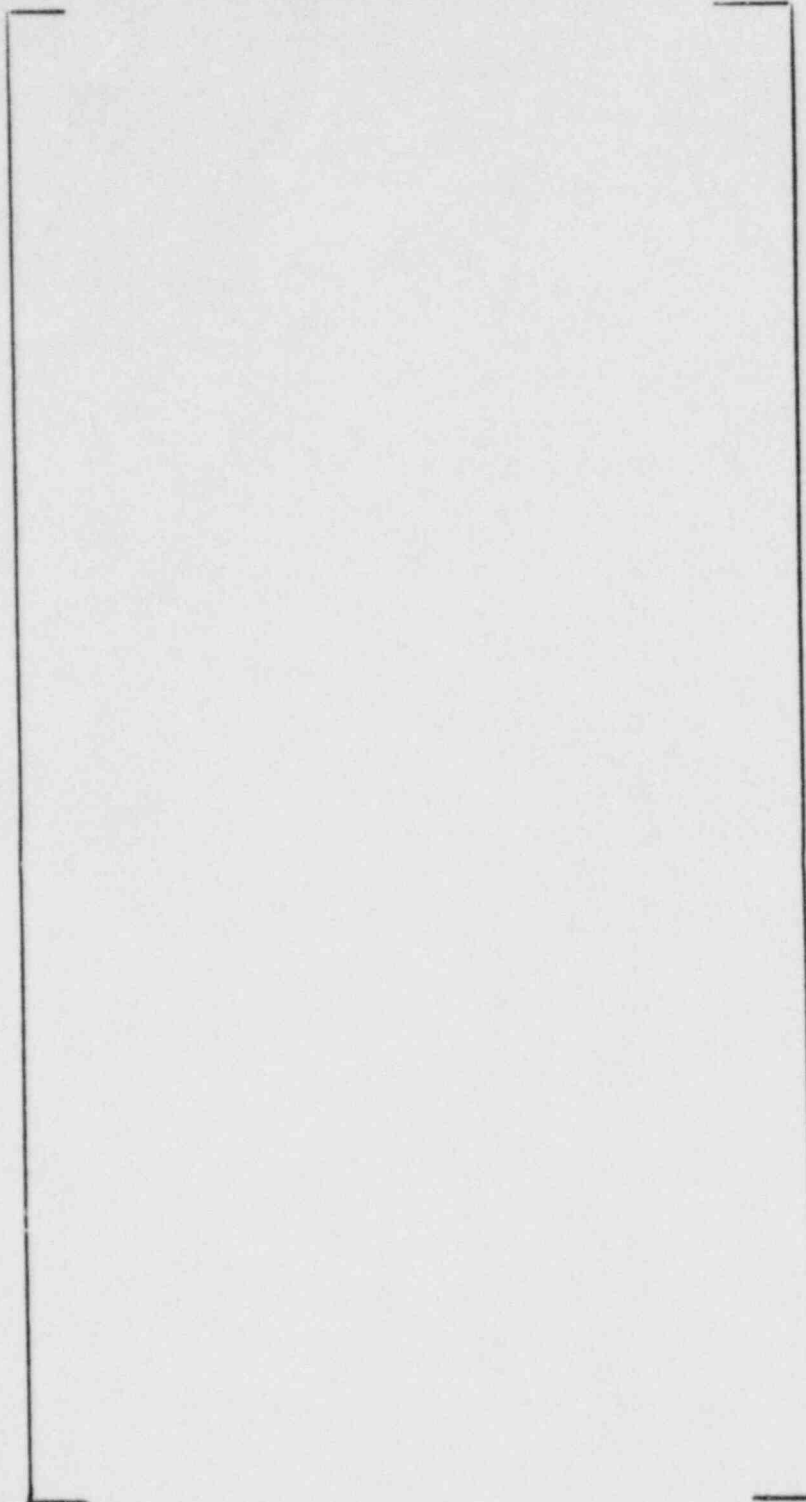


TABLE 3.2

ENERGY GROUP STRUCTURE FOR 85 GROUP LIBRARY

GROUP	E(upper),eV	GROUP	E(upper),eV
1	1.4919E+7	46	6.4760E+0
2	7.4082E+6	47	5.0435E+0
3	6.0653E+6	48	3.9279E+0
4	4.4933E+6	49	3.0590E+0
5	3.6788E+6	50	2.3824E+0
6	2.7253E+6	51	1.8554E+0
7	2.2313E+6	52	1.7262E+0
8	1.8268E+6	53	1.5950E+0
9	1.3534E+6	54	1.4575E+0
10	1.0026E+6	55	1.3079E+0
11	8.2085E+5	56	1.1664E+0
12	6.0810E+5	57	1.0987E+0
13	4.9787E+5	58	1.0722E+0
14	3.6883E+5	59	1.0624E+0
15	3.0197E+5	60	1.0525E+0
16	2.2371E+5	61	1.0428E+0
17	1.8316E+5	62	1.0137E+0
18	1.4996E+5	63	9.5069E-1
19	1.1109E+5	64	7.8211E-1
20	8.6517E+4	65	6.2493E-1
21	6.7380E+4	66	5.0326E-1
22	4.0868E+4	67	4.1704E-1
23	2.4788E+4	68	3.5768E-1
24	1.5034E+4	69	3.2064E-1
25	9.1188E+3	70	3.0113E-1
26	5.5308E+3	71	2.9075E-1
27	3.3546E+3	72	2.7053E-1
28	2.0347E+3	73	2.5104E-1
29	1.2341E+3	74	2.2770E-1
30	7.4852E+2	75	1.8444E-1
31	4.5400E+2	76	1.4573E-1
32	2.7536E+2	77	1.1157E-1
33	1.6702E+2	78	8.1970E-2
34	1.3007E+2	79	5.6925E-2
35	1.0130E+2	80	4.2757E-2
36	7.8893E+1	81	3.0613E-2
37	6.1442E+1	82	2.0493E-2
38	4.7851E+1	83	1.2397E-2
39	3.7267E+1	84	6.3250E-3
40	2.0923E+1	85	2.2770E-3
41	2.2603E+1		
42	1.7604E+1		
43	1.3710E+1		
44	1.0677E+1		
45	8.3153E+0		

TABLE 3.3

ENERGY GROUP STRUCTURE FOR 41 GROUP LIBRARY

GROUP	E(upper),eV	GROUP	E(upper),eV
1	[]	21	[]
2			
3			
4			
5			
6			
7			
8			
9			
10			
11			
12			
13			
14			
15			
16			
17			
18			
19			
20			
		22	
		23	
		24	
		25	
		26	
		27	
		28	
		29	
		30	
		31	
		32	
		33	
		34	
		35	
		36	
		37	
		38	
		39	
		40	
		41	

TABLE 3.4

Experiment	No. of Rods	$\frac{V_{\text{Mod}}}{V_{\text{Fuel}}}$	Soluble Boron (PPM)	Measured Buckling (M^{-2})	k_{eff} (Calculated)	ρ^{28}		ρ^{28}		ρ^{25}		Conversion Ratio		
						Meas.	Calc.	Meas.	Calc.	Meas.	Calc.	Meas.	Calc.	
Winfrith														
UO_2 (3.5U235)														
R1/100H(20°C)	1565	1.0	0.0	66.06					.0858 ^{+0.0009}	.0850			4.158 ^(±.03) 4.151	
R1/100H(80°C)	1565	1.0	0.0	62.64					.0895 ^{+0.0027}	.0869			4.293 ^(±.05) 4.268	
R2/100H(20°C)	665	3.16	0.0	100.00										
R3/100H(20°C)	2820	0.78	0.0	51.66					.1066 ^{+0.0018}	.1005			4.789 ^(±.05) 4.798	
TRX														
U_{METAL} (1.31XU235)														
TRX-1(20°C)	763	2.35	0.0	57.00					1.320 ^(±.021)	1.292	.0946 ^(±.0041)	.0966	.0987 ^(±.0010) .017	.797 ^(±.008) .773
TRX-2(20°C)	577	4.02	0.0	54.69					.837 ^(±.016) .810	.810	.0693 ^(±.0015)	.0695	.0614 ^(±.0008) .024	.647 ^{**} .628
EPRI-BHML														
UO_2 (2.35XU235)														
U-L175(22°C)	708	1.196	0.9	69.12										
U-L66(18°C)	383	2.408	0.5	84.14										
U-L162(22°C)	342	3.687	0.9	73.52										
U-L119(25°C)	1201	1.196	463.8	49.39										
U-L73(21°C)	1201	2.408	568.0	39.03										
U-L143(23°C)	885	3.687	285.8	39.13										
BAPL UO_2 (1.31XU235)														
BAPL-1(20°C)	2173	1.43	0.0	32.59					1.39 ^(±.01)	1.36	.078 ^(±.004)	.075	.084 ^(±.002) .086	
BAPL-2(20°C)	1755	1.78	0.0	35.47					1.12 ^(±.01)	1.14	.070 ^(±.004)	.065	.068 ^(±.001) .070	
BAPL-3(20°C)	1575	2.40	0.0	34.22					.906 ^(±.01)	.897	.057 ^(±.003)	.053	.052 ^(±.001) .054	

* Relative Conversion Ratio

** Conversion Ratio

TABLE 3.5
C-E CRITICALS

CORE
 Configuration

<u>Lattice</u>	<u>Fuel Rod Array</u>	<u>Fuel Cell Pitch Inch</u>	<u>Number of Fuel Rods</u>	<u>Temp. of Core</u>	<u>Soluble Boron Conc. PPM</u>	<u>Number of Control Rod Channels</u>
[]	30X30	[]	[]	68°F	[]	[]
	30X30			68°F		
	30X30			68°F		
	30X30			68°F		
	30X30			68°F		

TABLE 3.6

FUEL SPECIFICATION (KRITZ EXPERIMENTS)

Fuel material (pellets)		UO ₂
Fuel density (dishing included)	g/cm ³	[]
U235 in U	wt %	

Fuel length	mm	[]
Pellet length	mm	
Oxide diameter	mm	

Canning material		Zircaloy 4
Density	g/cm ³	[]
Outer diameter	mm	
Inner diameter	mm	

TABLE 3.7

Comparison of Reactivity Levels for Non-Uniform Core

Core	$\frac{\text{Vol Mod}}{\text{Vol Fuel}}$	No. of Large Water Holes	Measured Axial Buckling M-2	Soluble Boron Conc. PPM	k_{eff}
C-E Criticals					
KRITZ					

This chapter provides a summary of benchmark comparisons of ROCS using DIT cross sections with experiments. These comparisons are grouped into the two categories of normal conditions and upset conditions. Normal conditions includes power distributions, rod bank worths and reactivity coefficients while upset conditions covers single rod worths and assembly power distributions for anomalous rod configurations.

All ROCS calculations in this chapter employed the Higher Order Difference method, and the verification of power distributions is based on instrumented assembly data only. Assembly power distribution results for ROCS using the Nodal Expansion Method were discussed in Section 2.1. Imbedded calculations of fuel pin power peaking were presented in Section 2.5. Combined uncertainties for ROCS and MC calculations of local power peaking information (i.e, instrumented assembly results from Section 4.1.2 combined with pin/box results from Section 2.5.4) are discussed in Chapter 5.

Because of the wealth of experimental data available for model verification and calibration, the definition of biases and uncertainties for ROCS/DIT for normal operation relies on comparisons to measured data rather than to higher order calculations. Three-dimensional ROCS/DIT models have been used to analyze the available core follow and start-up test data. These data consist of measured incore instrument powers, soluble boron concentrations throughout core life and safety related parameters such as isothermal temperature coefficients, power coefficients, control rod bank worths and soluble boron worths.

The calculations shown here used three-dimensional quarter core ROCS models with zero-current boundary conditions along the major axes.

The external boundary conditions [

[

The cross section tables used in these ROCS models were all prepared from DIT lattice calculations as discussed in Section 2.1.3. Most, but not all, ROCS models used the same cross section tables, [

[] The three-dimensional model for each reactor and cycle was depleted in a core follow mode, which simulated the actual core operation for that cycle. End-of-cycle isotopics were then shuffled according to the loading pattern for the subsequent cycle. Thus isotopics used for any power distribution comparison or reactivity calculation always reflected true core history up to that point in time.

4.1.1 Reactivity

The verification of the ROCS/DIT reactivity predictive capabilities is performed by comparison against experimental data for both steady state parameters and reactivity coefficients. Three-dimensional ROCS/DIT computer models, incorporating the same cross section tables used in standard design calculations, are used to simulate the reactor start-up and operation. These ROCS models did not include the fuel rod spacer grids. The calculated reactivities simulate measured critical states and thus give a measure of the reactivity bias attributable to the models. Derivatives of the reactivity with respect to core parameters are discussed in Sections 4.1.3 through 4.1.6.

Start-up Data

Measured data obtained during reactor start-up are the most reliable, because they consist of well controlled conditions. Eleven cores have been analyzed, covering 4 cycles of fuel management. At the beginning of first cycles, the core compositions are entirely defined by the as-built characteristics of the fuel assemblies. At the beginning of later cycles, the core compositions are obtained from the end of the previous cycle, depleted to its correct end point, and shuffled into the new cycle. Decay of Iodine-135, Xenon-135, Promethium-149, Neptunium-234 and Plutonium-241 over the length of the refueling shutdown was simulated.

Table 4.1 shows the measured and predicted hot, zero power, xenon free, all rods out critical boron concentrations for each cycle. Over the eleven points of the data base, the critical soluble boron concentration is underestimated by an average of [] with tolerance limits of [] at a 95/95 probability/confidence level. In terms of reactivity, this corresponds to an underprediction by [] with two sided tolerance limits of []

Depletion Calculations

The depletion calculations are performed with a finite number of time steps, simulating the actual plant operation in terms of power level, inlet temperature, soluble boron concentration, and control rod insertion. These conditions were assumed to remain constant over the length of the depletion step. The depletion calculations typically model any change in operating condition which lasts more than [] MWD/T.

The operating data from the various reactor sites consist of measured critical conditions characterized by the core average exposure, the power level, the inlet temperature, the soluble boron concentration and the control rod insertion. These equilibrium conditions must prevail for at least two days to ensure that steady state operation has been reached. The frequency with which the data are collected varies from weekly to daily, thus generating a data base of measured conditions much larger than the number of calculated values. In order to benefit from this large data base, an interpolation strategy has been developed for the calculated data to produce a calculated reactivity at each one of the measured critical conditions. This process has been applied to ANO-2 cycle 1 (16X16 assembly type) and eight cycles of the 14X14 assembly type cores; i.e., Calvert Cliffs I cycles 2 and 3, Calvert Cliffs II cycles 1 and 2, and St. Lucie I cycles 1 through 4. The calculated reactivity values inferred for the entire data base are plotted in Figure 4-1. These results define the reactivity bias for future cycles. A least squares fitting through the points indicates that the reactivity bias has no statistically significant burnup dependence.

A large data base of 1281 data points has been used to establish the bias of [] with tolerance limits of [] at a 95/95 probability/confidence level. The small magnitude of the bias confirms the good predictive capabilities of the ROCS/DIT system. This bias and uncertainty are in very good agreement with the hot zero power results given earlier, demonstrating that Doppler and thermal-hydraulic reactivity effects, as well as fission product worth, are correctly treated throughout life by ROCS/DIT.

4.1.2 Assembly Power Distributions

The uncertainty to be attributed to calculated fuel assembly power distributions can be obtained by comparing detailed three-dimensional calculations of the assembly powers with those inferred from incore measurements with the CECOR^(4.1) system using fixed in-core rhodium detectors. The resulting differences are a reflection of both measurement and calculative errors. In order to determine the uncertainty to be attributed to the calculation, the measurement uncertainty has been subtracted out from these difference distributions as described below. The basic measurement uncertainty was taken from an evaluation of the uncertainty associated with the CECOR system, Part I of Reference 4.1. Thus, this section estimates variances for both the difference between calculation and measurement (σ_D^2), and for the difference between calculated and true assembly power (σ_C^2).

Introduction

Estimates have been made of:

(1) σ_{FR}^D - the standard deviation between measurement and calculation in radial power sharing - []

(2) σ_{FQ}^D - the overall peak power standard deviation - [] and,

(3) σ_{FXY}^D - the planar peak power standard deviation - []

Similarly, estimates have been made of σ_{FR}^C , σ_{FXY}^C , and σ_{FQ}^C , for the standard deviations of the differences between calculated and true assembly power. Sample standard deviations, S , have been used as estimates of the population standard deviations, σ .

These same comparison methods were recently used to assess the basic measurement uncertainty for assembly powers and are discussed in Section I.3.3 of Reference 4.1. The same normalization as in Reference 4.1 is chosen, and hence biases are identically zero. In the present report, the distribution of calculation - measurement differences was analyzed with DIT-based ROCS and CECOR models. The measurement uncertainty component, taken from Reference 4.1, was then subtracted in order to obtain an estimate of the ROCS/DIT assembly power calculative uncertainty.

Comparisons of measured and calculated assembly powers were made for various C-E cores over several cycles. The data base included Arkansas Nuclear One Unit 2 (ANO-2) cycle 1, Calvert Cliffs Unit 1 (BGE I) cycles 1 and 2, Calvert Cliffs Unit 2 (BGE II) cycles 1 and 2, and St. Lucie Unit 1 (FPL) cycles 1 through 3. ANO-2 is a 177 assembly core with a 16x16 fuel pin lattice, while the other cores have 217 assemblies with a 14x14 lattice. Overall, comparisons were made for these 8 cycles over 112 time points with on the order of 40 multi-level instrument strings each, resulting in about 20,000 calculation - measurement differences in the data base. Table 4.15 summarizes the results for this analysis.

Description of ROCS and CECOR Models

The ROCS calculations performed to generate the information for this section used three-dimensional quarter core models with zero current boundary conditions along the major axes. The external boundary conditions were [] Homogenized cross sections were obtained from DIT assembly calculations as described in Chapter 3.0.

Each fuel assembly was represented by [] nodes in the x-y plane. Axially, both the 136.7 inch, 217 assembly cores and the 150 inch, ANO-2 core were represented by [] nodes. Each in-core detector level

was represented by [] axial meshes except the outer-most level at the top and bottom of the ANO-2 core. These two levels used [] axial meshes in order to have similar mesh spacings at the core ends for the 136.7 inch and 150 inch cores.

The three-dimensional ROCS/DIT model for each reactor and cycle was depleted in a core follow mode which simulated actual core operation from beginning to end-of-cycle. These depletions incorporated details of power level, control rod insertion, inlet water temperature, and soluble boron operating histories, using several time-steps per 1000 MWD/T of core burnup.

The measured data consisted of assembly power distributions inferred by the CECOR code^(4.1) from "snapshots" of the fixed in-core rhodium detector signals taken periodically during each reactor cycle. The conversion of detector signals to instrument powers by CECOR is described in detail in Reference 4.1, as are the CECOR depletion models. The signal-to-box power conversion coefficients used in CECOR were obtained from two-dimensional fine-mesh calculations containing cross sections obtained from the same DIT assembly depletions used for the ROCS models.

Detailed Results

Sample standard deviations of ROCS - CECOR instrument powers at each detector level at each time point for the 8 reactor cycles are shown in Tables 4.2 through 4.9. These approximately 450 values form the F_{xy} data base. Standard deviations for F_R and F_Q are also shown in the tables for each time point. These sample standard deviations were calculated according to the methods of section I.3.3.2 of Reference 4.1, and are based on equations 3.8 to 3.20 given there.

Since the calculation - measurement comparisons used relative power

fractions, the standard deviations are in absolute, not relative, units. The differences are small and vary little level-to-level. All values are less than [] power fraction units and most values are less than [] units.

The least favorable values of $S_{\text{FGY}}^{\text{D}}$, S_{FR}^{D} and S_{FQ}^{D} at any timepoint or level for each cycle were chosen for the remaining analysis. These "worst case" values are highlighted in Tables 4.2 through 4.9, and are summarized along with the associated number of degrees of freedom in Table 4.10. The largest sample standard deviations of the calculation - measurement differences taken from Table 4.10 were:

$$\begin{aligned} S_{\text{FGY}}^{\text{D}} (\text{max}) &= [\quad] \text{power fraction units} \\ S_{\text{EQ}}^{\text{D}} (\text{max}) &= [\quad] \text{power fraction units} \\ S_{\text{FR}}^{\text{D}} (\text{max}) &= [\quad] \text{power fraction units} \end{aligned}$$

Estimate of Calculative Uncertainty

Since the deviations of calculation and measurement from the true power are independent stochastic variables the following relation is assumed to hold for the associated sample variances:

$$S_{\text{D}}^2 = S_{\text{M}}^2 + S_{\text{C}}^2 \quad (4.1-1)$$

where S_{D}^2 is the sample variance for the difference between ROCS/DIT calculated and measured assembly powers from Table 4.10. The variance associated with the difference between calculated and true assembly power, S_{C}^2 , is obtained from (4.1-1) by introducing the value of S_{M}^2 taken from the evaluation of the measurement uncertainty associated with CECOR. [

[]

The results obtained are shown in Table 4.11 for F_{xy} , Table 4.12 for F_Q and Table 4.13 for F_R . The least favorable S_C values for each peaking factor are highlighted in the tables and summarized below:

$$\begin{array}{l} S_{FXY}^C (\text{max}) = \left[\quad \right] \text{power fraction units} \\ S_{FQ}^C (\text{max}) = \left[\quad \right] \text{power fraction units} \\ S_{FR}^C (\text{max}) = \left[\quad \right] \text{power fraction units} \end{array}$$

The maximum values of S_D and S_C for F_{xy} , F_Q , and F_R are summarized again in Table 4.14. They are also converted from absolute units to a percentage basis by dividing by the minimum peak assembly power occurring during the cycle. One-sided tolerance limits for the population standard deviations have been constructed from the sample standard deviations assuming that the distributions are normal and are also shown in Table 4.14. The 95/95 probability/confidence factors were determined from the tables by Owen^(4.2). The number of degrees of freedom were determined as follows:

$$f_D = \text{number of contributing differences} - 1, \text{ as seen in Tables 4.2 to 4.9}$$

$$f_M = \left[\quad \right] \text{Reference 4.1}$$

and f_C from the following approximation:

$$\frac{S_D^4}{F_D} = \frac{S_C^4}{F_C} + \frac{S_M^4}{F_M} \quad (4.1-2)$$

The final one-sided tolerance limits, given on a 95/95 probability/confidence level, are summarized in Table 4.15. The calculative tolerance limits, kS_C , in the ROCS/DIT calculation of

assembly power peaks are:

$$\left[\begin{array}{l} \text{for } F_Q \\ \text{for } F_{xy} \\ \text{for } F_R \end{array} \right]$$

This excellent agreement between ROCS/DIT and measured three-dimensional assembly power distributions demonstrates the reliability of these codes and supports their use as valid nuclear reactor design tools.

These uncertainties in ROCS assembly power peaking are combined with the MC uncertainty in peak-to-assembly-average power (pin/box factor) in Chapter 5.

4.1.3 Inverse Boron Worth

The Inverse Boron Worth (IBW) is expressed as the number of PPM of soluble boron needed to change the core reactivity by 1%. The IBW, although not strictly a reactivity coefficient, is measured during start-up testing. It is used by the plant operator to assist him in plant maneuvering and control. The IBW is also used as input to safety analyses involving safety injection and in the analysis of the boron dilution accident.

Measured boron worths were obtained as a by-product of the control rod bank measurements performed at start-up and as such reflect the errors inherent in the measured critical boron concentrations and measured rod bank worths. The ROCS/DIT IBW's were similarly obtained during the calculations of control rod bank worths given in Section 4.1.5. The results of comparisons over four reactors and several cycles of operation are shown in Table 4.16.

The calculations overpredicted the IBW by an average of [] PPM/% reactivity. On a relative basis, this translates to a bias of [] of the measured IBW with a sample standard deviation of [] corresponding to tolerance limits of $\pm kS = []$ on a 95/95 probability/confidence level. These results represent an improvement on the accuracy historically associated with the prediction of inverse boron worths.

4.1.4 Isothermal Temperature Coefficient

The Isothermal Temperature Coefficient (ITC) is the change in core reactivity resulting from a 1°F change in moderator and fuel temperatures. The ITC is used here because it is directly measurable, unlike the moderator temperature coefficient which excludes the effects of concurrent fuel temperature changes.

Isothermal Temperature Coefficients have been measured for a number of reactors and cycles, both at power and at zero power, and for a wide range of soluble boron concentrations (83 to 1342 PPM). Three-dimensional ROCS calculations were performed at the same conditions as the measurements using concentration files taken from core follow depletions.

The plants included in the data base were AND-2 cycle 1, Calvert Cliffs Unit I cycles 1 through 4, Calvert Cliffs Unit II cycles 1 through 3 and St. Lucie I cycles 1 through 3. This data base contains 37 comparisons which are shown in Table 4.17. Included in the tables are the calculated and measured ITC's, their differences and the respective power level and soluble boron concentration.

Measured and calculated ITC's were found to be linear functions of the measured soluble boron concentration (PPM). The ITC calculated - measured differences were also a linear function of PPM and so a least squares linear fit was used to determine a PPM-dependent bias.

[] Thus the final results of this analysis consisted of a PPM-dependent bias curve and the associated tolerance band about that curve.

Figure 4-2 shows the calculated - measured differences as a function of PPM of soluble boron, the least squares linear fit, and the tolerance band about that fit. This linear fit is used to estimate PPM-dependent biases to apply to future ITC predictions with ROCS/DIT. When the bias curve is used the tolerance limits are $\pm 0.18 \times 10^{-4} \Delta\rho / ^\circ\text{F}$ on a 95/95 probability/confidence level.

These small tolerance limits, which include measurement error in addition to the calculative error, demonstrate the high accuracy of ROCS and DIT calculations of reactivity coefficients at operating temperatures. Low temperature end-of-cycle measurements are not readily available, but the excellent agreement with measurements seen here, as well as in Section 4.1.1 on reactivity and Sections 4.1.5 and 4.2.2 concerning control rod worths, establishes confidence in the use of ROCS for safety related calculations such as the cooldown following a steam line break accident.

4.1.5 Control Rod Bank Worths

Sequential insertions of regulating and shutdown control rod banks from start-up tests were simulated with three-dimensional ROCS calculations. The plants included in the data base were Calvert Cliffs Unit I cycles 1 through 4, Calvert Cliffs Unit II cycles 1 through 3, St. Lucie 1 cycles 1 through 3, and ANO-2 cycle 1. All ROCS/DIT calculations were performed at the conditions of the respective measurements. Reload cycle models used isotopics from core follow depletions. Asymmetric control rod configurations were not included in this analysis (see Section 4.2).

Homogenized macroscopic rod cross sections for the coarse-mesh calculations were obtained by []

The comparisons of ROCS calculated control rod bank worths to the measured values are shown in Table 4.18. Analysis of the control rod worth data for first cycles indicated that calculation - measurement differences were small with respect to the start-up test acceptance criteria. In reload cycles, biases and uncertainties were somewhat larger, but still within the acceptance criteria. Specifically, first cycle rod bank worths were underpredicted by [just less than 2%] on the average, while reload cycle control rod worths were overpredicted by []

The 67 comparisons from 11 different fuel cycles were tested for normality and poolability of sample standard deviations. Bartlett tests showed that both first cycle 14X14 assembly core results and reload cycle (all 14X14 assembly) results each were poolable. ANO-2 Cycle 1 (16X16 assembly design) did not pool with the other first cycle cores because its variance was significantly smaller. Thus the

conservative approach was taken and the ANO-2 data was excluded from the subsequent analysis. The small first cycle underprediction was observed in ANO-2 as in the other first cycles. All 14X14 assembly core results, regardless of cycle, also pool, but because of the different means for first and reload cycles, the uncertainties were calculated for first and reload cycles separately.

Table 4.19 shows the two sample means and standard deviations for the calculated - measured rod bank worth differences, \bar{X} and S_D . The sample standard deviations of the differences are [] A variance (S_M^2) for the rod worth measurements was estimated by comparing duplicate plants (See Tables 4.20 and 4.21). A variance (S_C^2) for the calculation of the rod bank worths was then inferred using:

$$S_D^2 = S_M^2 + S_C^2 \quad (4.1-1)$$

The corresponding standard sample deviations, S_C , are also shown in Table 4.19.

Table 4.20 compares the first cycle measured rod bank worths for the duplicate plants Calvert Cliffs Units I and II and for St. Lucie I and Millstone II. It was assumed that the measured bank worths for the duplicate plants should be identical at beginning-of-life and the variance (S_Δ^2) of their differences was calculated. The overall measurement variance was then estimated from:

$$S_M^2 = (1/2) S_\Delta^2 \quad (4.1-3)$$

The resulting sample standard deviations S_Δ and S_M are shown in Table 4.21. The estimated measurement standard deviation of [] was based on first cycle beginning of life measurements and probably represents a lower bound for reload cycle measurements. This value of S_M was used in equation (4.1-1) for all cycles to estimate the values of S_C shown in Table 4.19.

Tolerance limit factors on a 95/95 probability/confidence level were taken from Reference 4.3. Biases and uncertainties estimated for rod bank worths in this analysis are shown in Table 4.22. The tolerance intervals, $\pm kS_D$, in the differences of ROCS/DIT to measured rod bank worths were [

The one-sided tolerance limit $+ kS_D$ is consistent with the acceptance criteria associated with start-up test predictions. The estimated calculative tolerance intervals, $\pm kS_C$, for the difference between ROCS/DIT and truth were [

] Thus the accuracy of ROCS/DIT is comparable to currently approved C-E methods and is acceptable for the calculation of control rod worths.

4.1.6 Power Coefficient

The power coefficient is the change in core reactivity due to a 1% change in power level. In addition to proper functionalization of the temperature dependence of the microscopic cross sections, accurate calculation of power coefficients depends on the model used for the effective fuel temperature. All current ROCS models employ fuel temperature correlations that are both local (nodal) power density and fuel exposure dependent. Direct fits to FATES^(4.5) fuel temperature data are used for each fuel type.

Power coefficients were analyzed for a data base similar to that of the isothermal temperature coefficient calculations. Plants and cycles included were Calvert Cliffs Unit I cycles 2 through 4, Calvert Cliffs Unit II cycles 1 through 3 and St. Lucie I cycles 1 through 3. Calculations were performed with the same three-dimensional ROCS/DIT models using isotopics from core follow type depletions. Each calculation matched the conditions of the respective measurement as closely as possible.

Table 4.23 shows 15 calculated and measured power coefficients and the differences between them. The average bias was small and slightly positive and therefore conservative. That is, the calculated power coefficients were about [] less negative than the measured values.

The uncertainty in ROCS/DIT power coefficients is characterized by tolerance limits of [] $\Delta\rho/\%power$ on a 95/95 probability/confidence level. These tolerance limits include both measurement and calculative error. Since the measurement error component is a significant contribution to these tolerance limits, it is concluded that ROCS/DIT is acceptable for calculating power coefficients.

UPSET CONDITIONS

This second half of the design use verification of ROCS/DIT also employs benchmark comparisons against measured data taken from reactor start-up tests at or near beginning of life. The category of upset conditions includes control rod worths and power distributions for anomalous rod configurations. Specifically, dropped, ejected and net (N-1) rod worths and dropped and ejected rod power distributions are covered. The power distribution comparisons are based on instrumented assembly data only and do not include local power peaking effects which are discussed in Chapter 5.

All ROCS calculations employed the HOD neutronics formulation. The ROCS/DIT models were the same as those used in the comparisons for normal operation and are described in detail in the introduction to Section 4.1. Most calculations were in three-dimensions, though a few two-dimensional midplane calculations were performed where appropriate.

4.2.1 Dropped, Ejected and Net Rod Worths

Reactivity worths for the sequential insertion of control rod groups were analyzed in Section 4.1.5. In this section, reactivity worths for some non-sequential asymmetric rod configurations are calculated and compared to measured values. The results for these anomalous rod configurations are then related to those for normal control rod operation. Some of the ROCS calculations in this section were also used for the power distribution comparisons shown in Section 4.2.2.

Dropped Rod Worths

Dropped rod calculations simulate the failure of a single control rod drive mechanism such that a single control rod assembly drops into the reactor core. Two-dimensional ROCS/DIT calculations were used in the analysis of hot zero power (HZP) reactivity worth measurements and three-dimensional calculations were used for those experiments at power where in-core instrument readings were also recorded.

Measured data was available for 7 rod drops all performed near beginning of life. Four reactors were sampled, including both 14X14 and 16X16 fuel assembly designs. One drop involved a part length control rod subgroup of 4 rods. Otherwise, the measurements were for single or dual yoked control rods.

The calculated and measured dropped rod reactivity worths are compared in Table 4.24. The absolute calculated-measured differences are small, [] The standard deviation of the differences is []

Ejected Rod Worths

Ejected rod calculations simulate the failure of a single control rod drive mechanism such that one control rod assembly is suddenly withdrawn (ejected) from an otherwise symmetric pattern of insertion. Two-dimensional ROCS/DIT calculations were used in the analysis of HZP reactivity worth measurements. Three-dimensional

calculations were used for those experiments performed at power where in-core instrument readings were also recorded or where the pseudo-ejected rod test was performed from partial rather than full insertion.

Measured data was available for 8 pseudo-ejected rod tests near beginning of life for four reactors. Both 14X14 and 16X16 assembly cores are included in the data base. One measurement was performed at two slightly different times in the beginning of St. Lucie I cycle 1, once at HZP and once at 50% of full power.

The calculated and measured ejected rod reactivity worths are shown in Table 4.25. The absolute calculated-measured reactivity differences are small []

Net (N-1) Rod Worths

Net rod worth calculations simulate the insertion of all control rods into the reactor core except one, the most reactive, which remains "stuck" out. All net rod worth measurements were performed at HZP beginning of life conditions and hence two-dimensional ROCS/DIT calculations were performed.

Four measured values were available, including the 16X16 assembly Arkansas core. In all cases except ANO-2, the control rod remaining stuck out was a dual yoked shutdown rod.

The calculated and measured net rod worths are compared in Table 4.26. The mean difference of [] represents a small [] underprediction of the measured N-1 rod worths which is in the conservative direction. Note that all four measurements are similarly underpredicted, with a standard deviation about the mean of []

Conclusions

The dropped, ejected and net rod worth comparisons all showed similar good results which are consistent with the previous analysis of control rod bank worths. This is demonstrated in Table 4.27 where the means and standard deviations for the upset rod configurations are compared with reactivity results for normal sequential insertions of control rod banks from Section 4.1.5. The normal rod bank reactivity results are taken from the first cycle only calculations seen in Table 4.18 because all upset rod calculations here were for first cycles. The mean and standard deviation for the normal sequential insertions are shown both in terms of relative differences (taken directly from Table 4.18) and the corresponding absolute reactivity differences. The rod drop and rod ejection results are shown in Table 4.28 in absolute units because relative units can be misleading when comparing small reactivity worths. The net (N-1) rod worth mean difference and standard deviation are shown in Table 4.28 in relative terms. This mixed approach is consistent with the selection of acceptance criteria for C-E start-up measurements of control rod worths.

Table 4.27 shows that the results obtained here for upset conditions compare favorably with the calculations for normal control rod operation. The mean differences are similar, showing basically a small underprediction of the measured rod worths. The standard deviations for the upset rod configurations are either less than or equal to the symmetric rod bank results. That is, there is no observed deterioration in the ROCS/DIT rod worths for asymmetric rod configurations. Thus the maximum control rod worth calculational uncertainty value of [] taken from Table 4.22 of Section 4.1.5 would be a conservative choice for upset rod configurations.

4.2.2 Dropped & Ejected Rod Power Distributions

ROCS/DIT calculations for dropped or ejected control rods are not very different from rodged cases included in the data bases of the sections in 4.1 Normal Operation. Nevertheless, these upset rod conditions do provide a method to verify the ROCS code for asymmetric (i.e, radially skewed) power distributions. In this section, instrumented assembly radial power distributions for dropped and ejected control rods are calculated with ROCS and compared to measurements.

The experiments were performed during the power ascension phase of start-up testing, typically at the 50% power plateau. Some AND-2 measurements were taken slightly later, near 1000 and again near 2000 MWD/T. In-core detector signals were recorded under equilibrium conditions prior to the experiment and then shortly after completion of the rod drop or pseudo-ejection. The experiments took place in less than one hour, so that xenon redistribution effects were small.

Three-dimensional ROCS calculations were performed for the rod ejections since these were all initiated from partial insertion. The AND-2 rod drops were also done in three dimensions because all 5 levels of in-core detector signals were recorded. Three rod drops involved two-dimensional calculations since only one level of in-core signals was available. All ROCS calculations simulated [

[] this results in conservative comparisons to measurement.

Results

The data base for this analysis is summarized in Table 4.28 and includes cores of both 14x14 and 16x16 assembly designs. There were 8 dropped rod experiments resulting in 28 planar comparisons and 7 pseudo-ejected rod experiments yielding 15 planar comparisons.

Before and after calculated instrument power distributions were compared to measurements as follows. Ratios of after-to-before powers were constructed from the normalized instrumented assembly radial power distributions. The resulting calculated and measured power distortion ratios were then compared. Figures 4-3 and 4-4 show typical radial comparison maps for a rod drop and a pseudo-ejection, respectively. Note that ROCS tends to overpredict the strong flux distortions in the neighborhood of the rod drop or ejection.

Next, subsets of the instrumented locations were selected (marked by circles in the sample maps) such that

- (1) power increased as a result of the event (i.e., measured power distortion ratios >1.0); and
- (2) the measured instrument power was greater than average after the experiment.

The ROCS-measured differences in these locations were then tabulated. Thus, for positive differences, ROCS conservatively overpredicts assembly power increases; and, conversely for negative differences, ROCS underpredicted the assembly power decreases.

Figure 4-5 shows the frequency distribution of the differences in calculated-measured power distortion ratios for the dropped rod cases. Figure 4-6 shows the same for the ejected rod cases. The shapes of these frequency distributions are quite similar. Both are skewed towards positive differences because of the selection criteria above and the tendency of ROCS to overpredict the flux distortion near the anomalous rod locations. Even for the combined dropped plus ejected rod data base, illustrated in Figure 4-7, only a few locations exhibit underpredictions of the power increases. []

[] Thus the ROCS calculations of dropped and ejected rod events are basically conservative.

Nonparametric statistics have been used to quantify the left-hand (non-conservative) sides of the frequency distributions in Figures 4-5 through 4-7. The method described on pages 116-120 of Reference 4.6 was used to estimate a one-sided tolerance limit on a 95/95 probability/confidence basis for each error distribution. These estimates are based on the following approximate relationship between the sample size, N, and the Rth data point

$$N \approx 9.75 \chi_{2R}^{0.95} + (R-1) \quad (4.2-1)$$

where $\chi_{2R}^{0.95}$ represents the 0.95 quantile of a chi-square random variable with 2R degrees of freedom. The error distributions are first ordered monotonically from the most negative difference through zero to the most positive difference. Values of R are then deduced from Table 4.29 which was calculated using Eq. (4.2-1) above. The Rth data point counting from the most negative difference represents the estimated lower tolerance limit.



Conclusion

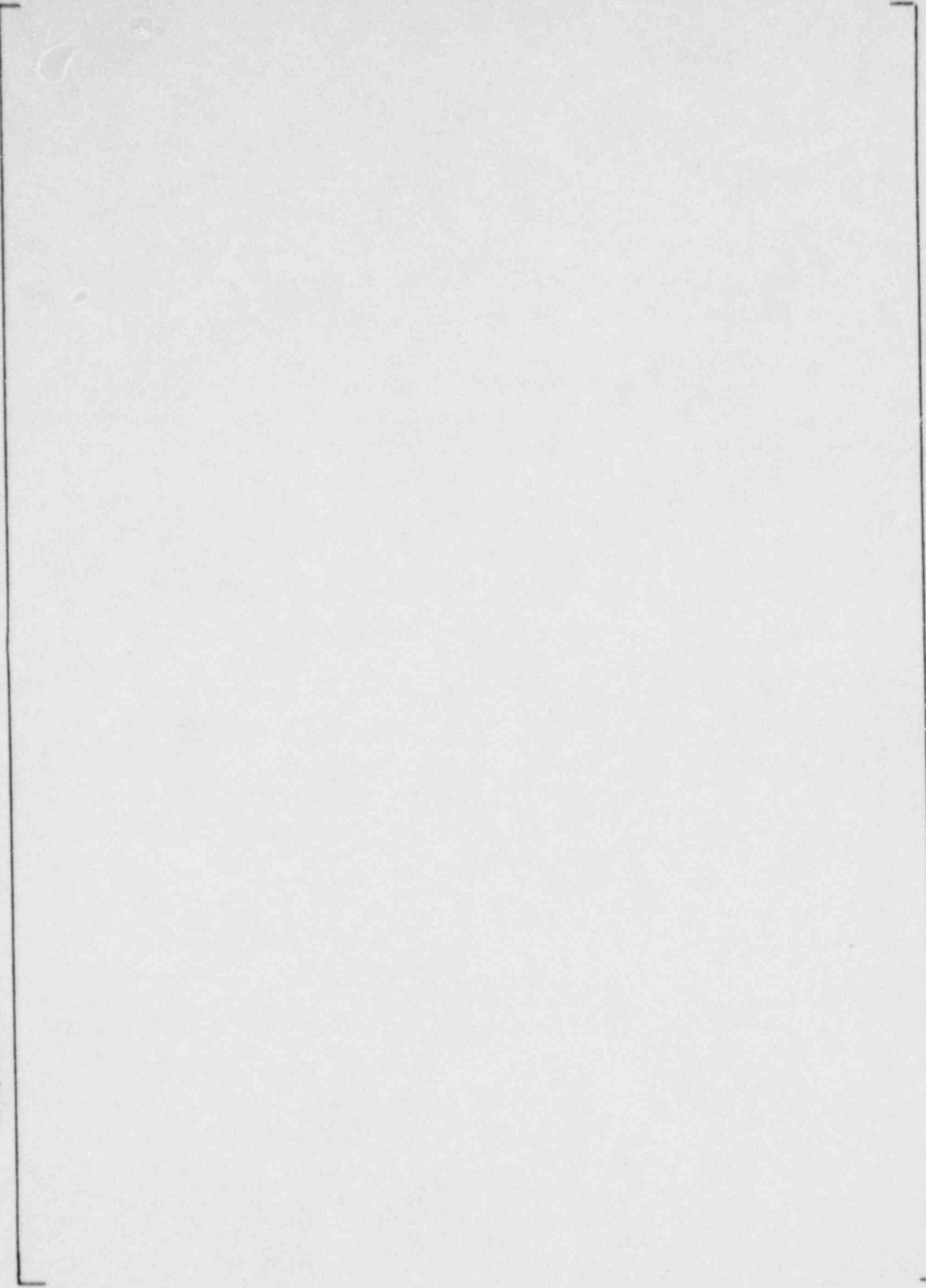
Considering the worst case only (the ejected rod comparison sample), we obtain a one-sided lower tolerance limit of [] confirming the initial observation. Thus ROCS/DIT predicts high power assemblies for asymmetric rodged configurations with sufficient accuracy to be used in the design and safety analyses of PWR cores.

4.3 REFERENCES

- 4.1 A. Jonsson, W. B. Terney, M. W. Crump, "Evaluation of Uncertainty in the Nuclear Power Peaking Measured by the Self-Powered, Fixed In-Core Detector System", CENPD-153-P, Rev. 1-P-A, May 1980.
- 4.2 D. B. Owen, "Factors for One-Sided Tolerance Limits and for Variables Sampling Plans", Tables 4.2.14 and 4.2.15, Sandia Corporation Monograph, SCR-607, 1963.
- 4.3 Ibid., Table 2.4.
- 4.4 A. Hald, Statistical Theory with Engineering Applications, p.291, J. Wiley & Sons, Inc., 1955.
- 4.5 P. H. Gavin, P. C. Rohr, "Development and Verification of a Fuel Temperature Correlation for Power Feedback and Reactivity Coefficient Application," Trans. Am. Nucl. Soc. 30, p.765, 1978.
- 4.6 W. J. Conover, Practical Nonparametric Statistics, pp. 116-120 and Table 2, John Wiley & Sons, Inc., 1971.

FIGURE 4-1

ROCS/DIT REACTIVITY FROM CORE FOLLOW CALCULATIONS



CORE AVERAGE EXPOSURE (GWD/T)

PERCENT REACTIVITY

FIGURE 4-2

CALCULATION - MEASUREMENT ITC DIFFERENCE vs SOLUBLE BORON
3D ROCS (DIT)

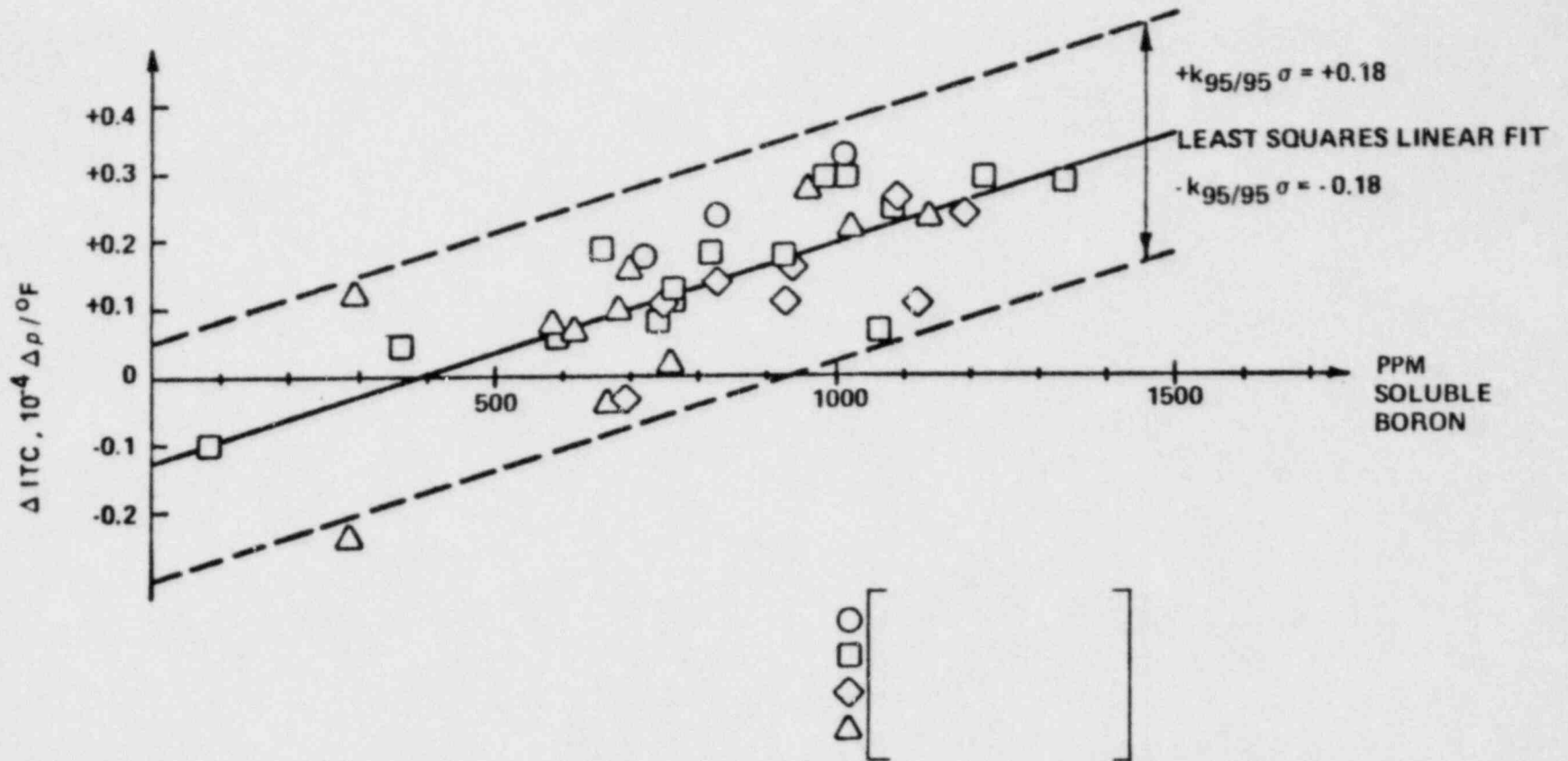


Figure 4-3
COMPARISON OF MEASURED AND CALCULATED
DROPPED ROD POWER DISTORTION RATIOS

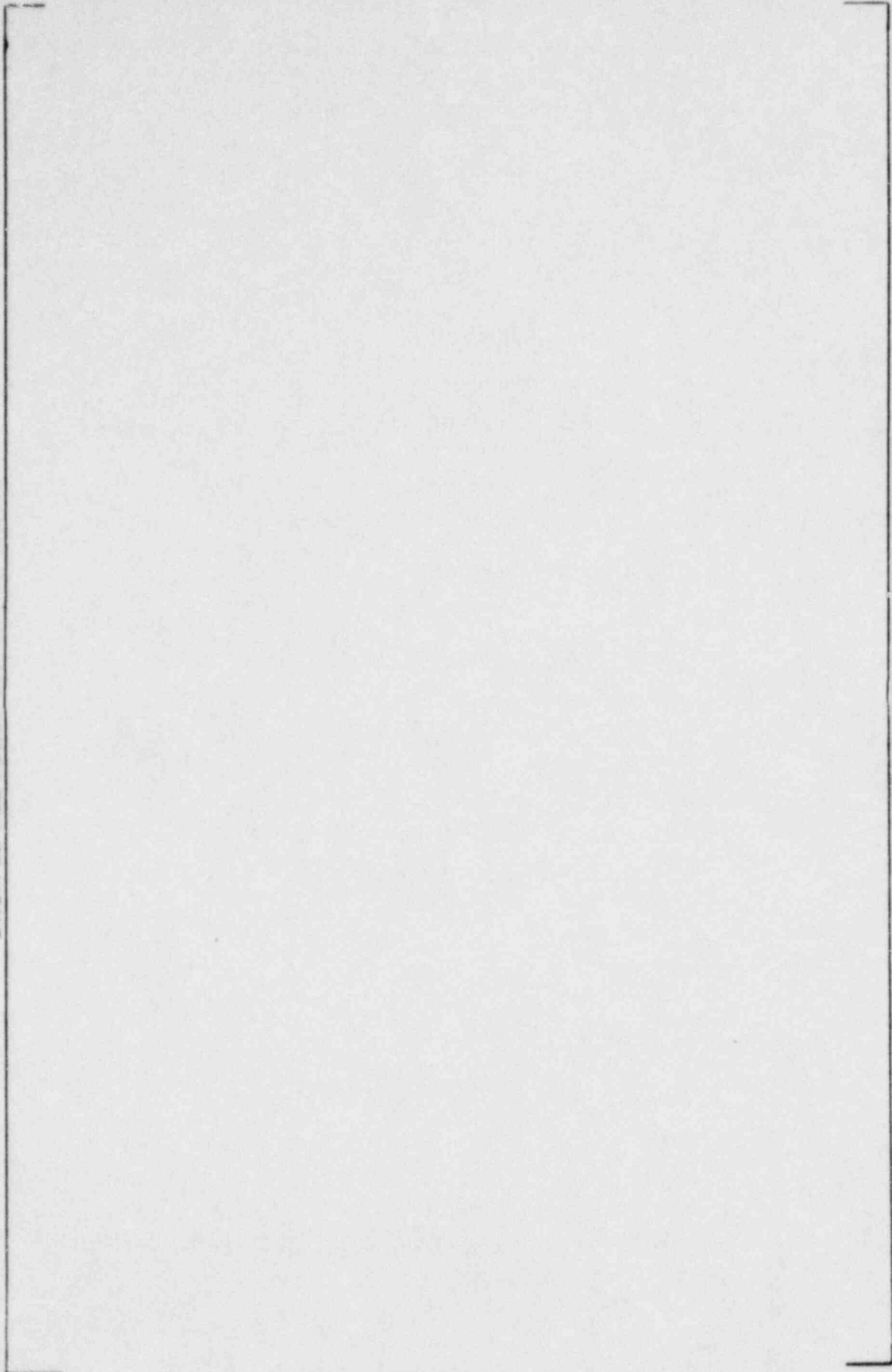
A_i AFTER/BEFORE RATIO OF INCORE DETECTOR POWERS (MEAS)
 B_i AFTER/BEFORE RATIO OF ROCS POWERS (CALC.)

Figure 4-4
COMPARISON OF MEASURED AND CALCULATED
EJECTED ROD POWER DISTORTION RATIOS

A_i = AFTER/BEFORE RATIO OF INCORE DETECTOR POWERS (MEAS.)
 B_i = AFTER/BEFORE RATIO OF ROCS POWERS (CALC.)

Figure 4-5

FREQUENCY DISTRIBUTION OF DIFFERENCES
DROPPED ROD POWER DISTORTION RATIOS



ROCS-MEASURED DIFFERENCE (BINS OF 0.0025)

FREQUENCY

Figure 4-6
FREQUENCY DISTRIBUTION OF DIFFERENCES
EJECTED ROD POWER DISTORTION RATIOS

FREQUENCY

4.31

ROCS-MEASURED DIFFERENCE (BINS OF 0.0025)

Figure 4-7

FREQUENCY DISTRIBUTION OF DIFFERENCES IN POWER DISTORTION RATIOS
FOR DROPPED AND EJECTED RODS

FREQUENCY
4.32

ROCS-MEASURED DIFFERENCE (BINS OF 0.0025)

TABLE 4.1

Beginning-of-Cycle, Hot Zero Power,
Xenon Free, Unrodded
Critical Boron Concentration

<u>Plant</u>	<u>Cycle</u>	<u>Critical Boron Concentration (PPM)</u>	
		<u>Measured</u>	<u>Calculated(ROCS/DIT)</u>
Calvert Cliffs I	1	[]
	2		
	3		
	4		
Calvert Cliffs II	1		
	2		
	3		
St. Lucie I	1		
	2		
	3		
ANO-2	1		

Average Difference (Meas-calc) = []
95/95 Tolerance Limits = []

TABLE 4.2

ANO-2 CYCLE 1 ROCs/DIT - CECOR

SAMPLE STANDARD DEVIATIONS OF CALCULATION - MEASUREMENT DIFFERENCES

Burnup (MWD/T)	Level 1		Level 2		Level 3		Level 4		Level 5		S_{FR}	f	
	S_D	f	S_D	f	S_D	f	S_D	f	S_D	f			
272	41	41	41	41	41	41	41	41	41	41		209	36
356	41	41	41	41	41	41	41	41	41	41		209	36
686	41	41	41	41	41	41	41	41	41	41		209	36
915	41	41	41	41	41	41	41	41	41	41		209	36
1150	43	40	40	40	41	41	41	40	42	42		211	36
1470	42	40	40	40	41	41	40	40	40	40		207	35
1775	40	40	40	40	41	41	38	40	40	40		203	36
1980	40	40	40	40	41	41	38	39	39	39		202	35
2380	41	41	41	41	41	41	39	40	40	40		206	35
2730	41	41	41	41	42	42	40	40	41	41		209	37
3210	41	41	41	41	42	42	40	40	41	41		209	37
3675	43	41	41	41	42	42	41	41	42	42		213	39
3915	42	41	41	41	42	42	41	41	42	42		212	38

Least favorable values are boxed

TABLE 4.3

CALVERT CLIFFS I CYCLE 1 ROCS/DIT - CECOR

SAMPLE STANDARD DEVIATIONS OF CALCULATION - MEASUREMENT DIFFERENCES

Burnup (MWD/T)	Level 1		Level 2		Level 3		Level 4					
	S_D	f	S_D	f	S_D	f	S_D	f	S_{FQ}	f	S_{FR}	f
850		44		44		43		44		178		43
3000		43		44		43		44		177		42
4000		43		44		43		44		177		42
5000		43		44		43		44		177		42
6000		43		44		43		44		177		42
7000		43		44		43		44		177		42
8000		43		44		43		44		177		42
9000		43		44		43		44		177		42
10000		43		44		43		43		176		41
11000		43		44		43		43		176		41
12000		43		44		43		43		176		41
13000		43		44		43		43		176		41
14000		42		44		43		42		174		39
15000		42		44		43		42		174		39

Least favorable values are boxed

TABLE 4.4

CALVERT CLIFFS I CYCLE 2 ROCS/DIT - CECOR

SAMPLE STANDARD DEVIATIONS OF CALCULATION - MEASUREMENT DIFFERENCES

Burnup	Level 1		Level 2		Level 3		Level 4					
(MWD/T)	S_D	f	S_D	f	S_D	f	S_D	f	S_{FQ}	f	S_{FR}	f
234		37		35		37		37		149		35
332		37		35		37		37		149		35
989		37		35		37		37		149		35
1436		37		35		37		37		149		35
1747		37		35		37		37		149		35
2087		37		35		37		37		149		35
2717		37		35		37		36		148		34
3338		37		34		37		35		146		32
3969		37		34		37		35		146		32
4184		37		33		37		35		145		31
5057		37		33		37		35		145		31
6006		37		33		37		34		144		30
6446		37		33		37		34		144		30
6924		37		33		37		34		144		30
7334		37		32		36		34		142		28
7555		37		32		36		34		142		28

Least favorable values are boxed

TABLE 4.5

CALVERT CLIFFS II CYCLE 1 ROCS/DIT - CECOR

SAMPLE STANDARD DEVIATIONS OF CALCULATION - MEASUREMENT DIFFERENCES

Burnup (MWD/T)	Level 1	Level 2	Level 3	Level 4	S_{FQ}	S_{FR}	f
1440	S_D []	S_D []	S_D []	S_D []	[]	[]	42
3330	f 44	f 43	f 43	f 44	[]	[]	41
5630	f 43	f 41	f 41	f 42	[]	[]	36
6230	f 43	f 41	f 41	f 42	[]	[]	36
6880	f 43	f 41	f 41	f 42	[]	[]	36
7435	f 43	f 41	f 41	f 42	[]	[]	36
8750	f 43	f 41	f 41	f 42	[]	[]	36
9980	f 43	f 41	f 40	f 42	[]	[]	35
0675	f 43	f 41	f 40	f 41	[]	[]	35
1980	f 43	f 41	f 40	f 40	[]	[]	33
3810	f 43	f 39	f 40	f 39	[]	[]	31
5185	f 43	f 39	f 39	f 38	[]	[]	31
5525	f 43	f 39	f 39	f 38	[]	[]	31

Least favorable values are boxed

TABLE 4.6

CALVERT CLIFFS II CYCLE 2 ROCS/DIT - CECOR

SAMPLE STANDARD DEVIATIONS OF CALCULATION - MEASUREMENT DIFFERENCES

Burnup	Level 1		Level 2		Level 3		Level 4					
(MWD/T)	S_D	f	S_D	f	S_D	f	S_D	f	S_{FQ}	f	S_{FR}	f
200		41		40		40		40		164		38
280		41		40		40		39		163		37
389		41		40		41		40		165		39
1438		40		40		40		39		162		36
1698		40		40		39		39		161		35
2518		40		40		39		39		161		35
3519		40		40		39		39		161		35
3943		40		40		39		39		161		35
5085		41		39		40		39		162		36
5966		40		38		40		39		160		34
6977		40		36		39		39		157		32
8096		39		35		38		38		153		29
8990		38		35		38		38		152		28
9631		37		35		38		36		149		27

Least favorable values are boxed

TABLE 4.7

ST. LUCIE I CYCLE 1 ROCS/DIT - CECOR

SAMPLE STANDARD DEVIATIONS OF CALCULATION - MEASUREMENT DIFFERENCES

Burnup	Level 1		Level 2		Level 3		Level 4					
(MWD/T)	S_D	f	S_D	f	S_D	f	S_D	f	S_{FQ}	f	S_{FR}	f
838		43		44		43		42		175		40
2139		43		44		43		42		175		40
2982		43		44		43		42		175		40
3420		43		44		43		42		175		40
4903		43		44		43		42		175		40
5513		43		44		43		42		175		40
6029		43		44		43		42		175		40
7093		43		44		43		42		175		40
8976		43		44		44		42		176		41
11359		41		43		44		42		173		38
12414		41		43		44		42		173		38

Least favorable values are boxed

TABLE 4.8

ST. LUCIE 1 CYCLE 2 ROCS/DIT - CECOR

SAMPLE STANDARD DEVIATIONS OF CALCULATION - MEASUREMENT DIFFERENCES

Burnup	Level 1		Level 2		Level 3		Level 4					
(MWD/T)	S_D	f	S_D	f	S_D	f	S_D	f	S_{FQ}	f	S_{FR}	f
189		41		43		42		42		171		39
317		41		43		43		42		172		40
560		41		43		43		42		172		40
1054		41		43		43		42		172		40
1361		41		43		43		42		172		40
1726		41		43		43		42		172		40
2234		41		43		43		42		172		40
2724		41		43		42		41		170		38
3132		41		43		42		41		170		38
3649		41		43		42		41		170		38
4200		41		43		42		41		170		38
4643		41		43		42		41		170		38
5087		41		43		42		41		170		38
5424		41		43		42		41		170		38
5948		41		43		42		41		170		38
6368		41		43		42		41		170		38
7030		41		43		43		40		170		38
7382		41		43		43		40		170		38
7885		41		43		43		40		170		38
8370		41		43		43		40		170		38

Least favorable values are boxed

TABLE 4.9
 ST. LUCIE I CYCLE 3 ROCS/DIT - CECOR
 SAMPLE STANDARD DEVIATIONS OF CALCULATION - MEASUREMENT DIFFERENCES

Burnup	Level 1	Level 2	Level 3	Level 4				
(MWD/T)	S_D	S_D	S_D	S_D	S_{FQ}	S_{FR}	f	f
486	42	43	43	44	175		40	
1004	42	43	43	43	174		39	
1434	42	42	43	43	174		39	
1864	42	43	43	42	173		38	
2385	42	43	43	43	174		39	
2927	42	43	43	40	171		36	
3400	42	43	42	38	168		34	
3923	42	43	43	38	169		35	
4529	42	43	41	38	167		34	
5603	42	42	41	38	166		34	
6687	42	42	41	38	166		34	

Least favorable values are boxed

TABLE 4.10

SUMMARY OF SAMPLE STANDARD DEVIATIONS OF ROCS/DIT-CECOR
 INSTRUMENT POWER Differences
 LEAST FAVORABLE* VALUES FOR EACH CYCLE

Core	Cycle	No. of Time Points	$S_{\text{FX}} Y$	f	S_{FQ}	f	S_{FR}	f
ANO-2	1	(13)	[]	(42)	[]	(209)	[]	(37)
Calvert Cliffs I	1	(14)	[]	(43)	[]	(177)	[]	(43)
	2	(16)	[]	(37)	[]	(149)	[]	(35)
Calvert Cliffs II	1	(13)	[]	(44)	[]	(177)	[]	(42)
	2	(14)	[]	(41)	[]	(163)	[]	(38)
St. Lucie I	1	(11)	[]	(42)	[]	(173)	[]	(40)
	2	(20)	[]	(43)	[]	(170)	[]	(38)
	3	(11)	[]	(42)	[]	(169)	[]	(34)

*) ie, the largest sample standard deviation for any timepoint in the depletion and any instrument level in the core.

The least favorable values over all cycles are boxed.

TABLE 4.11

ROCS/DIT F_{xy} CALCULATIONAL SUMMARY

Core	Cycle	S_D	f_D	S_M	f_M	S_C	f_C
ANO-2	1	[]	(42)	[]	(185)	[]	
Calvert Cliffs I	1		(43)		(174)		
	2		(37)		(2431)		(22)
Calvert Cliffs II	1		(44)		(45)		
	2		(41)		(2225)		
St. Lucie I	1		(42)		(171)		
	2		(43)		(3520)		
	3		(42)		(185)		

TABLE 4.12
ROCS/DIT F_0 CALCULATIONAL SUMMARY

Core	Cycle	S_D	f_D	S_M	f_M	S_C	f_C
ANO-2	1	[]	(209)	[]	(185)	[]	(129)
Calvert Cliffs I	1		(177)		(178)		(116)
	2		(149)		(2431)		
Calvert Cliffs II	1	[]	(177)	[]	(177)	[]	
	2		(163)		(2225)		
St. Lucie I	1				(173)		
	2		(170)		(3520)		
	3		(169)		(185)		

TABLE 4.13
 ROCS/DIT F_R CALCULATIONAL SUMMARY

Core	Cycle	S_D	f_D	S_M	f_M	S_C	f_C
ANO-2	1]	(37)]	(681)]	(14)
Calvert Cliffs I	1		(43)		(43)		
	2		(35)		(543)		
Calvert Cliffs II	1		(42)		(42)		
	2		(38)		(503)		
St. Lucie I	1		(40)		(516)		
	2		(38)		(811)		
	3		(34)		(681)		

TABLE 4.14
SUMMARY OF ROCS/DIT DIFFERENCE & CALCULATIVE UNCERTAINTIES

Assembly Power Peaks

	F_{xy}	F_Q	F_R
Least Favorable Case (All Calvert Cliffs I)	Calvert Cliffs I Cycle 2	Calvert Cliffs I Cycle 1	Calvert Cliffs I Cycle 2
<u>ROCS-Measurement Differences:</u>			
S_D (absolute)	[]
f_D	37	177	35
$k_{95/95}$	2.04	1.80	2.06
S_D (%)	[]
kS_D (%)	[]
<u>ROCS Calculational Uncertainty:</u>			
S_C (absolute)	[]
f_C	22	116	14
$k_{95/95}$	2.20	1.85	2.41
S_C (%)	[]
kS_C (%)	[]
Conversion to (%) assumes	[]	minimum peak	(Reference 4.1)

TABLE 4.15
 SUMMARY OF BOX POWER PEAKING UNCERTAINTIES⁺

	F_{XY}	F_Q	F_R
ROCS/DIT - Measurement	┌───┐		┌───┐
Calculative Uncertainty	└───┘		└───┘

⁺ Tolerance limit on a 95/95 probability/confidence level

TABLE 4.16

COMPARISON OF ROCS/DIT INVERSE BORON WORTH WITH MEASURED VALUES

CORE	MEASURED (PPM/% ρ)	CALCULATED (PPM/% ρ)	RATIO (Calc/Meas)
Calvert Cliffs II cy 1			
Calvert Cliffs II cy 2			
Calvert Cliffs II cy 3			
Calvert Cliffs II cy 3			
St. Lucie * cy 1			
St. Lucie * cy 3			
ANO-2 * cy 1			

mean ratio \pm standard deviation = []

mean value of calculated - measured differences = []

*Various rod configurations

TABLE 4.17

ITC SUMMARY FOR ROCS/DIT

CORE	CYCLE	%Power	PPM	MEASURED	CALCULATED ($\times 10^{-4} \Delta p / ^\circ F$)	DIFFERENCE	
Calvert Cliffs II	1	HZP	1090	[]]	
		50	827				
		96	745				
	2	HZP	1121				
		50	940				
		100	690				
	3	HZP	1191				
		50	923				
	St. Lucie I	1	HZP				962
50			696				
1A			51	681			
			83	619			
			98	585			
2		95	296				
		HZP	1024				
		100	670				
		97	288				
3		HZP	1137				
		100	757				
		Calvert Cliffs I	1	HZP	1087	[]
20	923						
50	820						
80	764						
100	740						
100	365						
2	95		83				
	HZP		1013				
	50		765				
	100		593				
3	HZP		1220				
	50		989				
	100		660				
4	HZP		1342				
	50		1066				
ANO-2	1	HZP	1012	[]]	
		20	825				
		50	720				

TABLE 4.18

**COMPARISON OF CONTROL ROD BANK WORTHS
3D ROCS (DIT) vs MEASUREMENT**

UNITS OF % DIFFERENCE FROM MEASURED WORTH

PLANT/CYCLE SEQUENTIAL ROD BANK	ANQ2	C.C.I	C.C.II	St.L.I	C.C.I	C.C.II	St.L.I	C.C.I	C.C.II	St.L.I	C.C.I
	CY 1	CY 1	CY 1	CY 1	CY 2	CY 2	CY 2	CY 3	CY 3	CY 3	CY 4

4.50

TABLE 4.19
ROD BANK WORTH SUMMARY FOR ROCS/DIT
MEANS & STANDARD DEVIATIONS

Units of % of bank worth

Sample Description	\bar{x}	S_D	S_M	S_C
First Cycles	[]
Reload Cycles	[]

TABLE 4.20

COMPARISON OF DUPLICATE PLANTS
FIRST CYCLE MEASURED ROD WORTH DIFFERENCES

BANK	<u>Calvert Cliffs</u>		<u>Difference*</u> (% of bank worth)
	<u>Unit I</u> (% reactivity)	<u>Unit II</u>	
5	[]	
4			
3			
2			
1			
C			

BANK	<u>St. Lucie</u>	<u>Millstone</u>	<u>Difference</u> (% of bank worth)
	<u>Unit I</u>	<u>Unit II</u>	
7	[]	
6			
5			
4			
2			
1			
B			

* Difference (%) = 2 (Plant 1 - Plant 2) / (Plant 1 + Plant 2) * 100%

TABLE 4.21

COMPARISON OF DUPLICATE PLANTS

Means & Sample Standard Deviations for Measured Rod Worths

Sample Description	$\bar{X} \pm S_{\Delta}$
Calvert Cliffs I vs. II	[]
Millstone II vs. St. Lucie I	
Combined	
	S_M^*
Combined	[]

$$* S_M^2 = \frac{1}{2} S_{\Delta}^2$$

TABLE 4.22

BEST ESTIMATED ROD WORTH
BIASES AND UNCERTAINTIES
FOR ROCS/DIT

Units of % of bank worth

Individual banks	Bias Observed \bar{x}	Uncertainties*	
		kS_D	kS_C
First Cycles	[]	[]	
Reload Cycles	[]	[]	

*) 95/95 probability/confidence level.

TABLE 4.23

COMPARISON OF POWER COEFFICIENTS
 3D ROCS(DIT) vs MEASUREMENT
 UNITS OF $10^{-4} \Delta\rho/\%P$

<u>PLANT/CYCLE</u>	<u>POWER (%)</u>	<u>CALCULATED</u>	<u>MEASURED</u>	<u>DIFFERENCE</u>
Calvert Cliffs I	2	50		
		100		
	3	50		
		100		
	4	50		
Calvert Cliffs II	1	50		
		96		
	2	50		
		100		
	3	50		
St, Lucie I	1	50		
		83		
		98		
	2	100		
	3	100		

4.55

TABLE 4.24
DROPPED ROD REACTIVITY WORTHS

CORE	ROD	CALCULATED (%Δρ)	MEASURED (%Δρ)	DIFFERENCE (C-M)
ANO-2	6-1	[]
	6-47			
	* P-24			
	* P-1(subgroup)			
Calvert Cliffs I	B-8			
St. Lucie I	B-7			
Millstone II	B-6			

* Part Length CEAs

Mean Difference []
Standard Deviation []

TABLE 4.25
EJECTED ROD REACTIVITY WORTHS

CORE	ROD	CALCULATED (% $\Delta\rho$)	MEASURED (% $\Delta\rho$)	DIFFERENCE (C-M)
ANO-2	6-1	[]
	4-11			
Calvert Cliffs I	5-1			
St. Lucie I	7-1 (HZP)			
	7-1 (50%P)			
Millstone II	6-15			
	7-1			
	6-16			

Mean Difference []
Standard Deviation []

TABLE 4.26
NET (N-1) ROD WORTH

CORE (Stuck Rod)	CALCULATED (%Δρ)	MEASURED (%Δρ)	DIFFERENCE (C-M)	
			Absolute(%Δρ)	Relative(%)
ANO-2 (A-52)	[]
St. Lucie I (A-49)				
Millstone II (A-49)				
Calvert Cliffs I (B-9)				

(Absolute) Mean Difference
Standard Deviation

(Relative) Mean Difference
Standard Deviation

--	--

TABLE 4.27

SUMMARY OF ANOMALOUS ROD REACTIVITY WORTHS

	MEAN CALC-MEAS DIFFERENCE	(Units)	STANDARD DEVIATION
Single Rod Drops	[]	(Abs.)	[]
Single Rod Ejections	[]	(Abs.)	[]
Net (N-1) Worth	[]	(Rel.)	[]
First Cycle Rod <u>Banks</u> (Ref. Table 4.18)	[]	(Abs.)	[]
	[]	(Rel.)	[]

TABLE 4.28
 RADIAL POWER DISTRIBUTION COMPARISONS
 IN UPSET ROD CONFIGURATIONS

	<u>CORE</u>	<u>ROD</u>	<u>Axial Planes of Instrument Signals</u>	
<u>DROPPED ROD</u> (8 measurements)	ANO-2	6-1	5	
		6-46	5	
		5-60	5	
		4-11	5	
		P-24	5	
		Calvert Cliffs I	5-58	1
	Millstone II	B-8	1	
		B-6	1	(28 planar) (comparisons)
<u>EJECTED ROD</u> (7 measurements)	ANO-2	6-1	3	
		6-46	3	
	Calvert Cliffs I	5-1	1	
		5-37	1	
		5-58	1	
	Millstone II	7-1	3	
		7-59	3	(15 planar) (comparisons)

TABLE 4.29
 RELATIONSHIP OF SAMPLE SIZE AND DATA POINT
 REPRESENTING ONE-SIDED LOWER TOLERANCE LIMIT

<u>R</u>	<u>Degrees of Freedom</u>	<u>$\chi_{2R}^{0.95}$</u>	<u>N</u>
1	2	5.991	58
2	4	9.488	93
3	6	12.59	124
4	8	15.51	153
5	10	18.31	181
6	12	21.03	216
15	30	43.77	434
16	32	46.17	458
17	34	48.57	482
22	44	60.46	632
23	46	62.80	657
24	48	65.15	682
25	50	67.50	707

where $N \sim 9.75 \chi_{2R}^{0.95} + \frac{1}{2} (R - 1)$

5.0 COMBINATION OF ASSEMBLY PEAKING AND LOCAL PEAKING UNCERTAINTIES

5.1 Statistical Model

One-sided tolerance limits for the random error in pin peaking as calculated by ROCS and MC is to be established for each of the three peaking factors F_q , F_r and F_{xy} . Table 4.14 from Section 4.1.2 contains estimates of the mean error and variance for assembly average power (box power) peaking (F_{qBOX} , F_{rBOX} and F_{xyBOX}). Table 2.2 from Section 2.5.4 contains an estimate of the mean deviation and variance for MC versus PDQ comparisons of the true pin/box factors, F_p . The core pin peaking factors are related to F_{BOX} and F_p by:

$$F_q = \text{Max} (F_{qBOX} \cdot F_p) \quad (5.1-1)$$

$$F_r = \text{Max} (F_{rBOX} \cdot F_p) \quad (5.1-2)$$

$$F_{xy} = \text{Max} (F_{xyBOX} \cdot F_p) \quad (5.1-3)$$

The uncertainties of the box peaking and pin/box factors will be combined in order to establish the overall uncertainty. To do this, one must first derive estimates of the mean error (μ_p) and variance (σ_p^2) for the random error (relative to true values) for the pin/box factor calculated by ROCS and MC.

Uncertainty In Pin/Box Factor For ROCS and MC

Section 2.5.4 established the following estimates of the mean difference and standard deviation for pin/box factors calculated by MC compared to PDQ. Let (μ_{MP}, σ_{MP}) be the mean and standard deviation for this distribution of differences. The estimates obtained were:

$$\mu_{MP} \cong \bar{D}_{MP} = [\quad] \quad (5.1.4)$$

$$\sigma_{MP} \approx S_{MP} = [\quad] (\text{Absolute}) \text{ or } [\quad] (\text{Relative}) \quad (5.2-5)$$

$$f_{MP} = 51 \quad (5.1-6)$$

where the mean difference and sample variance are taken from the least favorable case and f_{MP} is the associated number of degrees of freedom.

Reference 5.1 Part II documented the estimated uncertainty for PDQ models constructed by Combustion Engineering, Inc. using DIT cross sections. This uncertainty is characterized by:

$$\mu_{PDQ} \approx \bar{D}_{PDQ} = [\quad] \quad (5.1-7)$$

$$\sigma_{PDQ} \approx S_{PDQ} = [\quad] \quad (5.1-8)$$

$$f_{PDQ} = [\quad] \quad (5.1-9)$$

[]

The absolute standard deviation in Eq. (5.1-8) was obtained by multiplying the relative value by the minimum DIT pin/box factor from Reference 5.1.

The following model is used to obtain estimates for (μ_p, σ_p) , the mean and standard deviation for pin/box factors calculated by ROCS and MC.

Let ϵ_{MP} , ϵ_{PDQ} and ϵ_p be the random variables for which means and variances have been defined above. Then,

$$E(\epsilon_{MP}) = \mu_{MP} \quad (5.1-10)$$

$$D^2(\epsilon_{MP}) = \sigma_{MP}^2 \quad (5.1-11)$$

$$E(\epsilon_{PDQ}) = \mu_{PDQ} \quad (5.1-12)$$

$$D^2(\epsilon_{PDQ}) = \sigma_{PDQ}^2 \quad (5.1-13)$$

$$E(\epsilon_p) = \mu_p \quad (5.1-14)$$

$$D^2(\epsilon_p) = \sigma_p^2 \quad (5.1-15)$$

where, in the terminology of Ref. 5.2, $E(\epsilon)$ is the mean value and $D^2(\epsilon)$ is the second moment (variance) of a random variable ϵ .

$$\text{Since } \epsilon_p = \epsilon_{MP} + \epsilon_{PDQ} \quad (5.1-16)$$

it follows from taking first moments of this equation that:

$$E(\epsilon_p) = E(\epsilon_{MP}) + E(\epsilon_{PDQ}) = \mu_{MP} + \mu_{PDQ}$$

and the mean value of the MC error can be estimated by:

$$\mu_p \cong \bar{\epsilon}_p = \bar{\epsilon}_{MP} + \bar{\epsilon}_{PDQ} \quad (5.1-18)$$

Similarly, taking second moments of Eq. (5.1-16) gives:

$$D^2(\epsilon_p) = D_{MP}^2 + D_{PDQ}^2 = \sigma_{MP}^2 + \sigma_{PDQ}^2$$

[] The variance of the MC error can therefore be estimated by:

$$\sigma_p^2 \cong S_p^2 = S_{MP}^2 + S_{PDQ}^2 \quad (5.1-20)$$

Inserting the numerical values from above the following estimates result for the mean and standard deviation for the MC pin/box factor error:

$$\left[\right] \quad (5.1-21)$$

$$\left[\right] \quad (5.1-22)$$

$$\sigma_p \leq S_p = [\quad] \quad (5.1-23)$$

$$f_p = [\quad] \quad (5.1-24)$$

The relative sample standard deviation was obtained by dividing the absolute value from Eq. (5.1-22) by the minimum PDQ calculated pin/box factor from the same least favorable case. The equivalent number of degrees of freedom associated with the sample variance S_p has been estimated from the following approximation [

$$\frac{S_{MP}^4}{f_{MP}} = \frac{S_p^4}{f_p} + \frac{S_{PDQ}^4}{f_{PDQ}} \quad (5.1-25)$$

Combination of Box Power and Pin/Box Uncertainties

The box power uncertainty is characterized by $(\mu_{BOX}, \sigma_{BOX})$, the population mean and standard deviation of the random error. Estimates,

$$\mu_{BOX} \approx \bar{D}_{BOX} \quad (5.1-26)$$

$$\sigma_{BOX}^2 \leq S_{BOX}^2 \quad (5.1-27)$$

were obtained in Chapter 4, Table 4.14. Since only relative power distributions are considered, μ_{BOX} is identically zero. The pin/box factor uncertainty (μ_p, σ_p) , was estimated above. The overall combined uncertainty for core pin peaking will be characterized by (μ, σ) and the method for estimating this is described below.

Eqs. (5.1-1) to (5.1-27) show the single analytical relationship between the box power and the pin/box factors. It follows from these relationships that the random errors are related by:

$$[\quad] \quad (5.1-28)$$

Hence the sample variances can be assumed to be chi-square distributed and it follows that:

$$\frac{S^4}{f} = \frac{S_{\text{BOX}}^4}{f_{\text{BOX}}} + \frac{S_p^4}{f_p} \quad (5.1-35)$$

A 95%/95% probability/confidence multiplier is obtained from Reference 5.1 using the overall number of degrees of freedom, f , as determined from (5.1.35). The lower one-sided tolerance limits for the deviation between ROCS with MC and the true power distribution is then determined by:

$$\bar{D} = k_{95/95} S \quad (5.2-36)$$

5.2

Numerical Results

Numerical values are obtained by following the method described in 5.1 and using the results for \bar{D}_{BOX} , S_{BOX} , f_{BOX} and \bar{D}_p , S_p , f_p as determined in Sections 4.1.2 and 5.1 respectively. The combined uncertainties associated with F_q , F_r and F_{xy} are shown below and in Table 5.1. For clarity, Table 5.1 also includes the corresponding data for F_{BOX} and F_p .

	$\bar{D}(\%)$	$S(\%)$	f	$k_{95/95}$	$\bar{D}-kS(\%)$
F_q	[]
F_r					
F_{xy}					

The one-sided tolerance limits $\bar{D}-k_{95/95} S$ use the convention that the deviations correspond to ROCS and MC minus truth. Thus the overall calculative uncertainty is such that there is a 95% probability that at least 95% of the true F_q , F_r and F_{xy} values will be less than the values obtained with ROCS and MC plus [] respectively.

It is concluded that the ROCS code, including the fine-mesh module MC, is an accurate design tool for the calculation of two- and three-dimensional, coarse- and fine-mesh flux and power distributions. It is also concluded that ROCS and MC are sufficiently accurate for the generation of coefficient libraries for the in-core instrumentation, replacing the use of two-dimensional PDQ in the procedures described in Part II of Reference 5.

References

- 5.1 A. Jonsson, W. B. Terney, M. W. Crump, "Evaluation of Uncertainty in the Nuclear Power Peaking Measured by the Self-Powered, Fixed In-Core Detector System", Part II, Section 3.3 and Appendix 3.1, CENPD-153-P, Rev. 1-P-A, May 1980.
- 5.2 H. Cramer, Mathematical Methods of Statistics, Princeton University Press, Princeton, 1954.
- 5.3 D. B. Owen, "Factors for One-Sided Tolerance Limits and for Variables Sampling Plans," tables 4.2.14 and 4.2.15, Sandia Corporation Monograph, SCR-607, 1963.

TABLE 5.1
TOLERANCE LIMITS FOR CORE
LOCAL POWER PEAKING FOR
ROCS AND MC USING DIT CROSS SECTIONS

	$\bar{D}(\%)$	S(%)	f	k _{95/95}	\bar{D} -kS(%)
$F_{q, BOX}$	[]
$F_{r, BOX}$					
$F_{xy, BOX}$					
F_p	[]
F_q					
F_r					
F_{xy}					

Chapters 2 and 3 describe the methodology used in the ROCS and DIT computer codes as well as in the imbedded fine-mesh MC calculations. Chapter 3 and Reference 5.1 provide verification for the DIT code by comparison to critical experiments. Chapter 4 presents extensive comparisons of ROCS with DIT cross sections to measurements for both normal operation and upset conditions. Uncertainties for peak-to-assembly average pin power and assembly average power were combined in Chapter 5.

The results of the analyses contained within this report show that the use of ROCS and DIT for both normal and upset operating conditions is associated with the biases and uncertainties shown in Table 6.1. All tolerance limits are given on a 95/95 probability/confidence level. Numerical values of tolerance limits are in all cases smaller than the conservatism applied by C-E to the input for safety analyses.

Conclusions

This report establishes the ROCS and DIT computer codes and the MC module as adequate tools for nuclear core design and safety-related core neutronics calculations with well quantified uncertainties. Their capabilities and levels of accuracy are concluded to be sufficient for the neutronics design including all safety related parameters dependent on two- and three-dimensional coarse- and fine-mesh flux and power distributions, control and absorber worths, depletion and power dependent reactivity level, reactivity coefficients and reactivity differentials. It is also concluded that the ROCS code, including the fine-mesh module MC, is of sufficient accuracy for the generation of coefficient libraries for the in-core instrumentation, replacing the use of two-dimensional PDQ in the procedures described in the topical report on the CECOR code system.

TABLE 6.1
SUMMARY OF ROCS, DIT AND MC
BIASES & CALCULATIVE TOLERANCE LIMITS

<u>Reactivity Related</u>	<u>Section</u>
Core Reactivity	4.1.1
Inverse Boron Worth	4.1.3
Power Coefficient	4.1.6
ITC and PPM-dependent bias	4.1.4
<u>Control Rod Worths</u>	
First cycle rod banks	4.1.5
Later cycle rod banks	4.1.5
Dropped, ejected, (N-1) rods	4.2.1
<u>Power Distributions</u>	
Assembly Power F_Q (ROCS with HOD)	4.1.2
F_{XY}	
F_R	
With dropped or ejected rods	4.2.2
Local Pin Power (DIT)	Reference 5.1
Core Pin Peaks F_q (ROCS and MC)	5.2
F_{xy}	
F_r	

COMBUSTION ENGINEERING, INC.